Karlsruher Institut für Technologie

FSM

Measurements of velocity fields in a centrifugal fan by means of Particle Image Velocimetry

Master thesis No.: 1883

by

B.Sc. Christian Feldle

At the faculty of engineering,
Institute of Fluid Machinery

October 2017 – March 2018

Supervisor:
Dr.-Ing. Balazs Pritz
M.Sc. Johannes Walter

Declaration of Authorship

I hereby certify that this thesis has been composed by me and is based on my own work, unless stated otherwise. No other person's work has been used without due acknowledgement in this thesis. All references and verbatim extracts have been quoted, and all sources of information, including graphs and data sets, have been specifically acknowledged.

Date: Signature:

Abstract

This thesis contains measurements of flow velocity fields inside the blade channel of a centrifugal fan by using *Particle Image Velocimetry* (PIV), an optical method for flow visualization. The results are analyzed and compared to previous experiments. It concludes that they show a good compliance and quality.

Beforehand, the fan's characteristic curve and efficiency are determined and validated with preceding investigations. The results show a distinctive conformity with previous experiments and a good match with existing simulation data done by the Institute of Fluid Machinery. The measurements are done at different speeds to proof the scalability. The powertrain and the mounting for the camera and laser used for the experiments were modified to improve the quality of the data and to simplify the procedure of the PIV experiment.

PIV measurements are measured at the points of maximum efficiency, partial load and full load, whose position on the characteristic curve were determined previously. The rotational speed is not varied in the PIV experiment, but in comparison to previous works, where only one fixed plane in the blade channel was measured, multiple planes are measured. This allows to visualize the flow in more depth and a profound knowledge about the flow conditions can be gathered.

Resumen

Esta Tesis presenta medidas de los campos de velocidad de flujo de partículas dentro del canal de aspas de un ventilador centrifugo usando Velocímetría de Partículas por Imágenes (PIV, por sus siglas en ingles), un método óptico para la visualización del flujo. Se concluyen que las mismas presentan buena adecuación y calidad. Previamente, la curva característica y eficiencia del ventilador fueron determinadas y validadas por investigaciones precedentes. Los datos obtenidos muestran una destacable concordancia con experimentos previos y una buena coincidencia con datos simulados existentes, hechos por el Instituto de Maquinaria de Fluidos, respectivamente. Las mediciones fueron llevadas a cabo a diferentes velocidades para probar su escalabilidad. El sistema de accionamiento y montaje de la cámara y laser usados para los experimentos fueron modificados para mejorar la calidad de los resultados y simplificar el procedimiento del experimento PIV. Las mediciones PIV fueron hechas en los puntos de máxima eficiencia, carga parcial y carga total, los cuales fueron determinados con anterioridad. La velocidad rotacional no fue variada durante los experimentos PIV, pero a diferencia de trabajos anteriores donde se realizaron mediciones un solo plano fijo en el canal del aspa, en el presente se realizaron mediciones en múltiples planos. Esto permitió visualizar el flujo en 3D con el uso de interpolación y pudieron recolectarse conocimientos profundos acerca de las condiciones de flujo.

ACKNOWLEDGMENTS

This work would not have been possible without the support of my thesis supervisors Dr. Balazs Pritz and Johannes Walter. Their door was always open for me. Furthermore, I would like to thank Prof. Dr. Gabi for his help and the chance to conduct this thesis at the Institute of Fluid Machinery.
I'd like to say a big thank you to the guys from the workshop for the assistance whenever I needed help.

Finally, I must express my very profound gratitude to my mother and to my girlfriend Esperanza for providing me with unfailing support and continuous encouragement throughout my years of study and through the process of researching and writing this thesis. Lastly, I'm thankful for all my friends that helped me during my studies. This accomplishment would not have been possible without them.

Dedicated to the memory of my father, Günter Feldle, who always believed in my ability to be successful in the academic world. You are gone, but your belief in me has made this journey possible.

Thank you!

Feldle, Christian

Table of contents

Symbols

a	$[\frac{m^2}{s^2}]$	specific work
A	$[m^2]$	area
b	$[mm]$	width
B	$[mm]$	width of volute housing
c	$[\frac{m}{s}]$	absolute velocity
c_{ref}	$[\frac{m}{s}]$	reference velocity
C	$[-]$	flow coefficient
d	$[mm]$	diameter
d_h	$[mm]$	hydraulic mean diameter
D	$[mm]$	outlet diameter
f	$[-]$	frequency
F	[N]	force
g	$[\frac{m}{s^2}]$	gravitational acceleration
h	$[mm]$	height
m	$[kg]$	mass
M	$[Nm]$	torque
n	$[\frac{1}{s}]$	rotational speed
n	$[-]$	number of measurements
p	$[Pa]$	pressure
P	$[W]$	power
r	$[mm]$	radius
R	$[\frac{J}{molK}]$	universal gas constant
s	[m]	surface
t	$[s]$	time
u	$[\frac{m}{s}]$	peripheral velocity
U	$[V]$	voltage
$\dot{V}$	$[\frac{m^3}{s}]$	volume flow rate
w	$[\frac{m}{s}]$	relative velocity

α	[°]	absolute flow angle
β	[°]	relative flow angle
γ	[°]	relative angle of target level
δ	[−]	diameter number
ϵ	[−]	expansibility factor
η	[−]	efficiency
ϑ	[°]	blade angel at leading edge
κ	[−]	isentropic exponent
λ	[−]	coefficient of performance
μ	$[Pa \cdot s]$	dynamic viscosity
μ	[−]	expected value
ν	$[\frac{m^2}{s}]$	kinematic viscosity
ρ	$[\frac{m^3}{kg}]$	density
σ	[−]	speed number
σ	[−]	standard deviation
φ	[−]	flow coefficient
φ_L	[−]	relative humidity
ψ	[−]	pressure coefficient
ω	$[\frac{1}{s}]$	angular velocity

Index

abs	absolute
amb	ambient
tot	total
stat	static
leak	leakage
m	model
OP	operation point

Abbreviations

PIV	Particle Image Velocimetry
KIT	Karlsruhe Institute of Technology
DEHS	Di-Ethyl-Hexyl-Sebacate
LSV	Laser Speckle Velocimetry
PTV	Particle Tracking Velocimetry
RSD	Relative Standard Deviation

List of figures

List of tables

1 Introduction

1.1 Motivation

Fans are built-in in a lot of daily use devices such as cars, laptops or table fans. Depending on the intended use, impeller diameters of a few centimeters up to twenty meters and more occur. Accordingly, the bandwidth of the drive power ranges from just a few watts into the megawatt range. The total electricity consumption of fans powered by motors with an electrical input between 125 W and 500 kW is 344 TWh per year and will increase to 560 TWh by 2020 if current EU market trends persist. The potential for cost-effective design improvements is around 34 TWh annually; this corresponds to CO_2 emissions of 16 million tons [16] [17]. Other main development goals for fans are operational safety and wear resistance. In addition, in the context of ever-increasing environmental awareness, noise abatement measures are playing an increasingly important role.

Many parameters determine how efficient a system with an integrated fan is working. When developing a new fan, it makes sense to design it for the given application and operating point. However, it is costly to build a new prototype for each application and therefore it makes often no sense. With the steady growth of the processing power of computers, simulations become more and more profitable. However, the internal flow that develops in a centrifugal fan impeller is exceedingly complex, involving system rotation, separation, and turbulence effects. Simulations are based on assumptions and simplifications and to deliver good results it must be validated with experimental data.

A good understanding of the flow phenomena in turbomachines are necessary to increase the efficiency. For this reason, velocity flow fields in the blade channel of a radial fan are investigated with *Particle Image Velocimetry*, which offers information on the instantaneous flow structures [28] [29].

1.2 Aim of this thesis

The aim of this thesis is to conduct and compare PIV measurement results to previous experimental and simulation data, respectively. Beforehand, efficiency and the centrifugal fan's characteristic curve are determined and compared to the results from *D. Sauerer* and with numerical simulation data from *T. Rhode*. The velocity flow fields of the blade channel of the impeller are investigated at three characteristic different operating points. These points include partial load, point of maximum efficiency and full load which are determined previously. In contrast to previous works on this test bench, this work contains multiple planes that are analyzed in order to learn more about the flow conditions.

The thesis is segmented into 7 chapters. Chapter 2 provides the fundamentals in fluid mechanics and turbomachinery. Also, the basics of particle image velocimetry are explained. The experimental set-up for the different measurements is extensive described in chapter 3. That includes the measurement instrumentation and calculation methods that are needed for the experiments. In chapter 4 and 5 are the results and their evaluations presented. The tests are compared to previous experimental data done at this test bench and to simulation data. Finally, in chapter 6 and 7 a summary of the most important conclusions are stated and suggestions for future works are given.

1.3 State-of-the-Art

There are already countless works in which the flow has been investigated in turbomachinery and in particular centrifugal fans, both experimentally and numerically. On the other hand, so far only a few studies have been carried out using *Particle Image Velocimetry* in turbomachinery.

M. Schroll examined flow conditions in the blade channel of a side channel compressor. In his work, the vortex flow generated by the rotating impeller was investigated with PIV. For this reason, the test bench was modified, so that it was optical accessible for PIV. The tests provided further insights by showing velocity fields of the blade channel. Beforehand, only the dynamic pressures were measured. Finally, both variables are combined and deeper insight into the flow conditions obtained [31].

In *Dornstetter's* work, the flow into a cross-flow fan was investigated by experimental and numerical methods to develop a numerical model for the study of important geometry parameters. Thus, on the one hand, the flow was calculated using Star-CD, a CFD program, and compared to experimental data obtained by means of Particle Image Velocimetry. With the help of the PIV measurement, the velocity distribution in the housing of the cross-flow fan was determined, but not in the impeller itself [30].

G. Wuibaut et al. investigated velocity fields of a radial flow pump impeller. The test rig was also modified and made suitable for the PIV measurements. Up to now, the database for the CFD validation for this geometry refer mainly to dynamic pressure, hot wire anemometers or laser doppler velocimetry results. The work shows that the PIV results are suitable and even better for understanding the flow phenomena associated with this turbomachine [32].

In summary it can be said, that currently research is being done on turbomachines with the help of PIV and the method shows promising features and advantages.

2 Basic principles

For a better understanding of this thesis this chapter will provide the necessary basics. The fundamentals of fluid dynamics and Particle Image Velocimetry are explained. More detailed information can be found in the literature and will be alluded at the intended passages.

2.1 Fluid mechanics

To describe the behavior of a flowing fluid, the basic equations for mass, momentum and energy are used, which will be explained below in simplified form with reference to a current filament. The flow is assumed to be frictionless, adiabatic and incompressible [18].

2.1.1 Fundamental equations

Stream filament theory deals with the flow along a stream filament, which is a model idea and must be thought of as a streamlined, thin streamtube with variable cross-sectional area. The change of all state quantities across the stream filament are small compared to those in the longitudinal direction. This stream filament has a mass flow $\dot{m}$.

$$\dot{m} = \rho \bar{c} A = const. \tag{2.1}$$

$\dot{m}$ stands for the mass flow, ρ the density, A for the surface and $\bar{c}$ for the mean velocity. For incompressible fluids (e.g. liquids), ρ is constant, and with volume flow rate $\dot{V}$ equation 2.1 becomes:

$$\dot{V} = \bar{c} A = const. \tag{2.2}$$

[18] [26].

Forces are calculated using the momentum equation. This results to:

$$\sum \overrightarrow{F_a} = \frac{dI}{dt} = \frac{d}{dt} \int_V \rho \bar{c} dV. \tag{2.3}$$

This results in the Euler differential equation:

$$\frac{dc}{dt} = \frac{\partial c}{\partial t} + c\frac{\partial c}{\partial s} = -\frac{1}{\rho}\frac{\partial p}{\partial s} - g\frac{\partial z}{\partial s}. \tag{2.4}$$

By integration along a stream filament results for a frictionless, incompressible and stationary flow:

$$\frac{1}{2}(c_2^2 - c_1^2) + g(z_2 - z_1) + \frac{p_2 - p_1}{\rho} = 0. \tag{2.5}$$

If the stream filament is curved, additional forces in radial direction occur. Neglecting gravitational forces, the momentum equation becomes the radial pressure equation:

$$\frac{c^2}{R} = -\frac{1}{\rho}\frac{\partial p}{\partial r}. \tag{2.6}$$

2.1.2 Fundamental theory

The central component of a turbomachine is the impeller. In it, energy is exchanged with the help of the fluid via deflection by the impeller blading. Depending on the location of the observer, different velocity fields result.

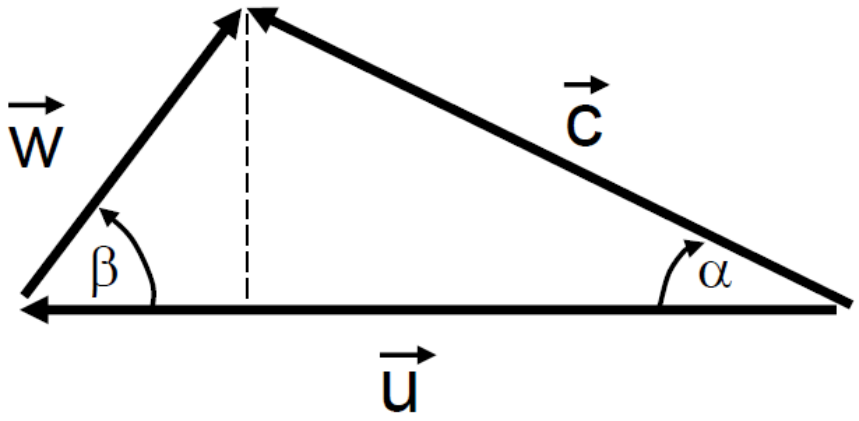

Figure 2-1: Relationship between absolute and relative velocity

If the flow in the impeller is viewed from a fixed component (absolute system), e.g. from the housing, you can see the absolute velocity $\vec{c}$. If the observer is moved with the impeller (relative system), he views the relative velocity $\vec{w}$. These two velocity fields are linked by the circumferential velocity $\vec{u} = \vec{\omega}\, x\, R$, resulting in the following vector equation:

$$\vec{c} = \vec{u} + \vec{w}. \tag{2.7}$$

In addition, in figure 2-1, the angle between the absolute and peripheral velocity, the absolute angle α, and the angle between the relative and peripheral velocity, the relative angle β, can be seen. Assuming a blade-congruent throughflow in the impeller and a swirl-free inflow, this vector equation can be applied to the fluid in the impeller. In addition, in this case the product of impeller width b and the radius R is assumed to be constant, so that due to the constant cross-sectional area at a constant volume flow, the meridional component of the absolute velocity remains constant. Thus, for each point in the impeller velocity triangles can be constructed. With them the flow can be described in a simplified manner. Figure 2-2 shows the velocity triangle using a radial impeller of a turbomachine.

Euler's equation for turbomachines

For the design of a turbomachine, it is necessary to conclude from the velocity triangles to the transmitted power. The Euler equation for turbomachines is used for this purpose. It can be derived by applying the angular momentum conservation theorem on the control room of a blade channel. Which is:

$$\sum \overrightarrow{M_a} = \frac{d\vec{L}}{dt} = \frac{d}{dt}\int_V \rho(\vec{R}\ x\ \vec{c})dV. \tag{2.8}$$

Since the compressive forces and gravity do not affect the sum of the outer moments, corresponds the external moment to the blade moment M_s. For a stationary flow we obtain:

$$M_s = \int_A \rho(\vec{R}\ x\ \overrightarrow{c_u})(\vec{c}\ \vec{n})dA. \tag{2.9}$$

Furthermore, by applying the velocities of a working machine in the integral we get:

$$M_s = \dot{m}(R_2 c_{u.2} - R_1 c_{u.1}). \tag{2.10}$$

With the help of the blade moment the transmitted power P_s results:

$$P_s = \vec{M} \cdot \vec{\omega}\,. \tag{2.11}$$

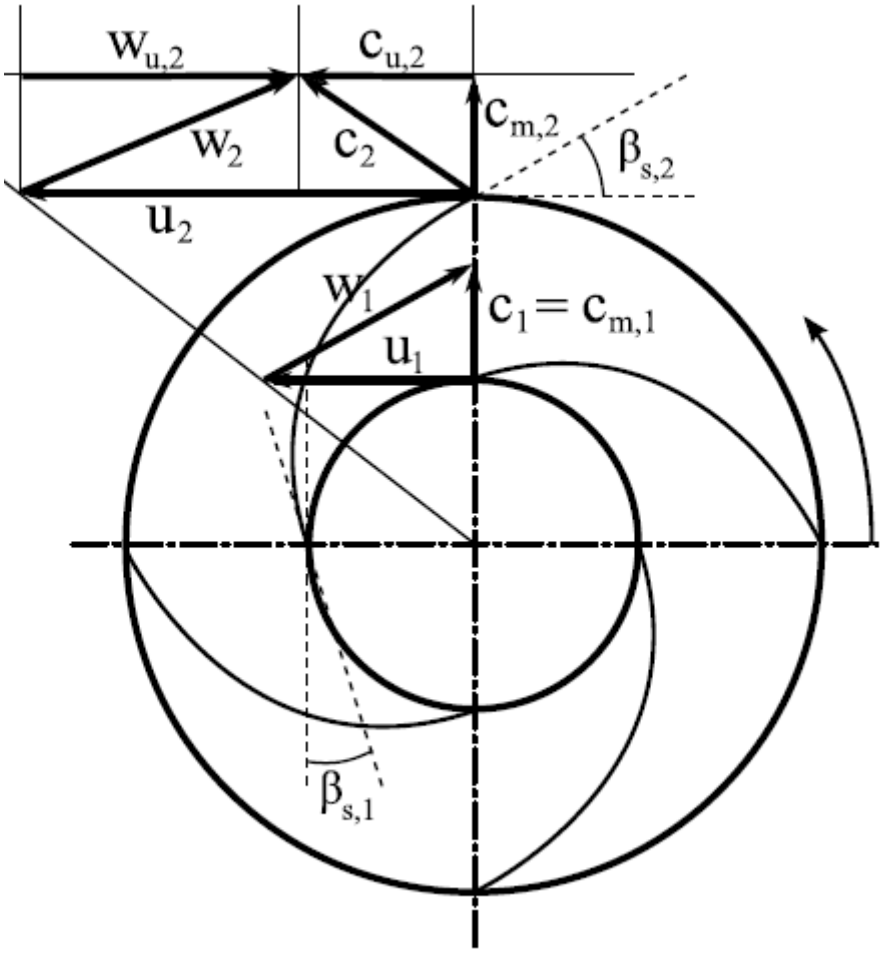

Figure 2-2: Velocity triangle for a radial turbomachine

By inserting of (2.10) in (2.11) and with $\vec{u} = \vec{\omega}\, x\, R$ ensues:

$$P_s = \dot{m}\left(u_2 c_{u,2} - u_1 c_{u,1}\right). \tag{2.12}$$

Dividing the equation by the mass flow $\dot{m}$ will lead to Euler's main equation for turbomachines:

$$a_s = \dot{m}(u_2 c_{u,2} - u_1 c_{u,1}) \tag{2.13}$$

[26].

2.1.3 Characteristic curve

Turbomachines are part of a technical system. The turbomachine is part of the system where work is done. In the rest of the system no work is done, there are only losses. Thus,

the requirements for a turbomachine depend on the system in which the turbomachine is installed. In a closed circuit, as used in the test bench under investigation, the only work that has to be done by the turbomachine is to overcome all losses in the entire system.

The characteristic curve of a turbomachine sets the pressure rise p of the machine in relation to the volume flow $\dot{V}$. Analogous to the increase in pressure, specific work y or head H as a representation of the flow work done by a turbomachine on the fluid are also common.

A flow machine can only be operated if it meets the pressure increase requirement of the system at a certain flow rate. This is the case at the intersection of the two characteristic curves. This point is commonly called operating point (OP).

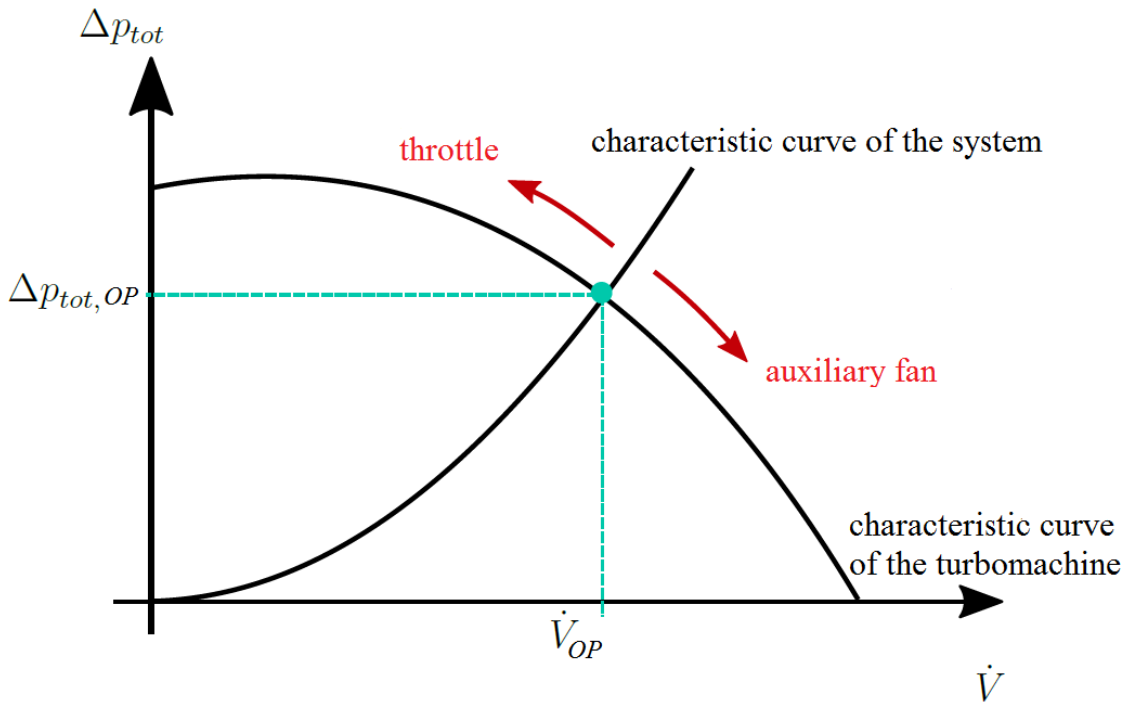

Figure 2-3: Characteristic curve

In the experimental determination of the characteristic curve of a turbomachine, different operating points are approached in order to subsequently record them. This is done by changing the system characteristics. On the one hand by throttling and on the other by the use of an auxiliary fan. When closing the throttle, as shown in figure 2-3: characteristic curve, the operating point shifts towards smaller flow rates. To achieve operating points with higher volume flows, an auxiliary fan is switched on additionally.

2.1.4 Similarity law and dimensionless coefficients

In designing and predicting the operation performance of turbomachinery with the help of data from similar machines, it is necessary to convert the operating data to other dimensions, speeds, values or other fluids. This conversion is done using similarity laws or dimensionless coefficients. Total compliance with all similarity laws is difficult to fulfill. However, the approximate fulfillment of the similarity laws allows a broad transferability of the flow conditions between similar machines. In many cases, it is advantageous to represent the operating performance of similar machines by means of characteristic maps from dimensionless coefficients, independent of size and speed.
Experimental investigations on turbomachinery can often only be carried out with smaller models than in reality. To draw the right conclusions from such experiments on their large-scale designs, the similarity laws must be known [13].

Similarity laws

In this chapter no subscript stands for the prototype and subscript m for the model.
For two machines to be similar, the following conditions must be met:

Geometrical similarity

Geometric similarity is fulfilled when all dimensions of the flow-relevant parts of two machines are scaled to the same ratio (e.g. diameter D and width b).

$$D = x \cdot D_m \, , b = x \cdot b_m. \tag{2.14}$$

Kinematic similarity

Another requirement is that the velocity triangles must be similar, meaning that the correspondent velocities of prototype and model are in a fixed ratio to each other.

$$\frac{c_2}{c_{2m}} = \frac{w_2}{w_{2m}} = \frac{u_2}{u_{2m}} \; etc. \tag{2.15}$$

With the peripheral speed $u = \pi n D$ the following relation applies:

$$\frac{u_2}{u_{2m}} = \frac{nD}{n_m D_m}. \tag{2.16}$$

Dynamic similarity

To obtain dynamic similarity forces must be similar. The magnitudes of forces at equivalent points in two dynamically similar systems must be in a fixed ratio [27].

$$\frac{(f_1)}{(f_1)_m} = \frac{(f_2)}{(f_2)_m} \; or \; \frac{Re}{Re_m} \tag{2.17}$$

with Re being the Reynolds number.

If all the requirements mentioned above are fulfilled the following affinity laws can be applied [13] [15]:

DESCRIPTION	DEFINITION	
VOLUME FLOW	$\frac{\dot{V}}{\dot{V}_m} = \frac{D^3 n}{D_m^3 \cdot n_m}$	(2.18)
PRESSURE INCREASE	$\frac{\Delta p}{\Delta p_m} = \frac{\rho \cdot D^2 \cdot n^2}{\rho_m \cdot D_m^2 \cdot n_m^2}$	(2.19)
SPECIFIC ENERGY	$\frac{y}{y_m} = \frac{D^2 \cdot n^2}{D_m^2 \cdot n_m^2}$	(2.20)
POWER	$\frac{P}{P_m} = \frac{\rho \cdot D^5 \cdot n^3}{\rho_m \cdot D_m^5 \cdot n_m^3}$	(2.21)

Table 2-1: Affinity laws

Dimensionless coefficients

The use of dimensionless coefficients for designing and description of operating performance is a common and practical tool in turbomachinery. They base on the similarity laws and link the most important operating data with their geometry and rotation speed.
In the following table 2-2 are the most important dimensionless coefficients listed for this thesis:

DESCRIPTION	DEFINITION	
FLOW COEFFICIENT	$\varphi = \frac{4\dot{V}}{\pi^2 D^3 n}$	(2.22)
PRESSURE COEFFICIENT	$\psi = \frac{2\Delta p_{tot}}{\pi^2 D^2 n^2 \rho}$	(2.23)
SPEED NUMBER	$\sigma = \frac{n}{(2\pi^2)^{-\frac{1}{4}} (\frac{\Delta p_{tot}}{\rho})^{\frac{3}{4}} \dot{V}^{-\frac{1}{2}}}$	(2.24)
DIAMETER NUMBER	$\sigma = \frac{D}{(\frac{8}{\pi^2})^{\frac{1}{4}} (\frac{\Delta p_{tot}}{\rho})^{-\frac{1}{4}} \dot{V}^{\frac{1}{2}}}$	(2.25)

Table 2-2: Dimensionless coefficients

2.2 Statistical significance

In modern experiments, huge amounts of data often accumulate. In order to get a sense or significance for such quantities, it is useful to define different variables [21].
The expected value of a sample μ is defined as:

$$\mu = \frac{1}{n} \sum_{i=1}^{n} x_i. \qquad (2.26)$$

Also important are measures that can be used to describe the span or variability of a sample. A variable suitable for this purpose is the number that describes the squares of the average distances between the mean and the individual sample data. This is the so-called variance or scatter of a sample.
The positive square root of the variance is called the standard deviation of the sample [19].

$$\sigma = \sqrt{\sigma^2} = \sqrt{\frac{1}{n-1}\sum_{i=1}^{n}(x_i - \mu)^2}. \qquad (2.27)$$

The relative standard deviation (RSD) is a measure of dispersion of a probability distribution. It is defined as the ratio between the standard deviation σ and the mean μ, thus expressed dimensionless. It is helpful to secure a repeatability and reproducibility of an experiment. A low RSD value is an indicator that the data is tightly clustered around the mean, on the other hand if the percentage is high, the data is more spread out. The more precise the data, the smaller the RSD [20].

$$RSD = \frac{\sigma}{|\mu|}. \qquad (2.28)$$

2.3 Particle Image Velocimetry

Particle Image Velocimetry (PIV) is a modern optical measurement technique, which can capture velocity information of whole flow fields. Its development started in the eighties of the last century and is continuously developing.

PIV allows a non-invasive measurement of the velocity field vectors of gaseous or liquidous fluids. In this technique the time is known, and the displacement of the particles is measured.

To calculate the velocity field tracer particles have to be added to the flow. Within a brief time interval these particles have to be illuminated in a plane (light sheet) of the flow. The light scattering of the tracer particles is done using a high-resolution camera and can be visualized. There are two different ways to measure the displacement of the particles: Either by using a single frame or a sequence of frames. With the help of correlation, the displacement of the particles in a plane can be calculated. The velocity vector can be calculated with the known frequency of the laser. The field of view (FOV) is separated in smaller areas – the interrogation areas (IA). For each IA the displacement vector for the image of the tracer particles of the first and second illumination is determined by means of statistical methods (e.g. cross-correlation).

In this experiment, due to the planar illumination of the flow, the velocity vector is determined in the standard two-component PIV (2D2C-PIV) [10].

In figure 2-4 the experimental set-up is shown with the laser, flow with tracer particles and the imaging optics.

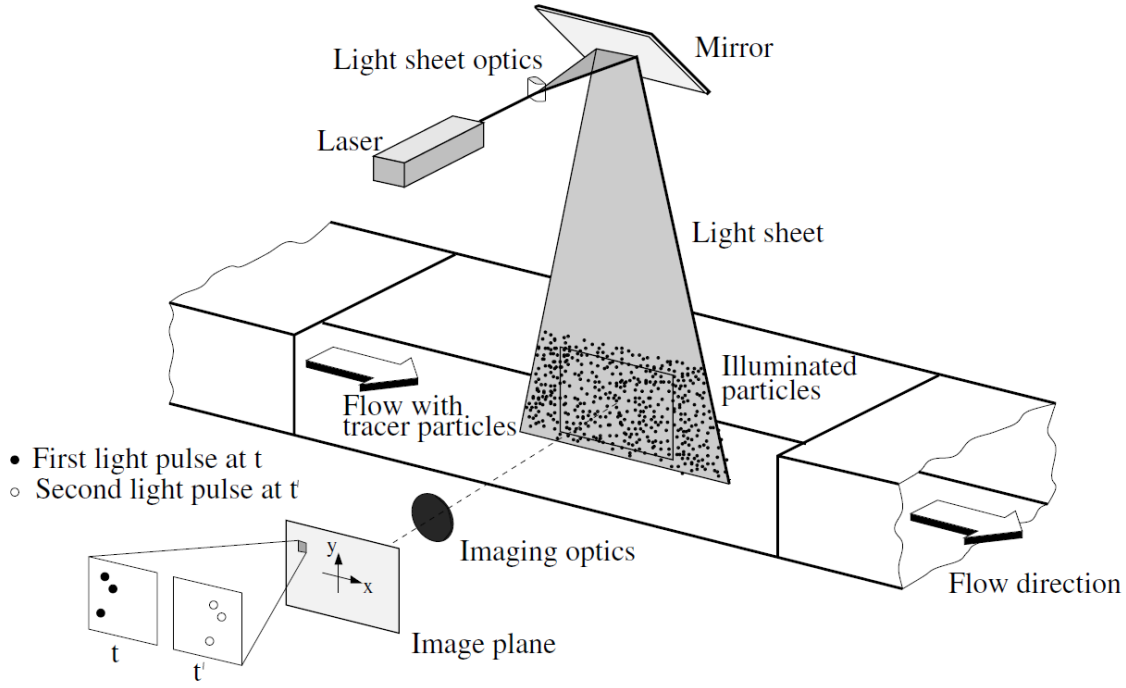

Figure 2-4: Experimental set-up for PIV in a wind tunnel [10]

2.3.1 Image acquisition

In contrast to other measurement techniques (e.g. hot-wire anemometry), PIV does not intrude the flow while investigating. To achieve a high degree of accuracy of images, which represent the flow, three main things need to be considered carefully: illumination of the flow, seeding particles and the medium for recording the images.

Flow illumination

The main factor for the choice of light source depends on the velocity range and size of the area that is going to be investigated. To produce usable results the seeding particles should not move a large distance during an illumination pulse so that the particles images are sharp. In addition, enough light must be scattered by the particles in order to detect them. In modern PIV, typically a pulsed laser system or a continuous wave laser is used because both meet the needed requirements.

2.3.2 Seeding particles

Since the velocity information are measured indirectly from the seeding particles, the accuracy of the results is limited by the ability of the particles to follow the flow precisely. Important parameters which influence this behavior are particle size, shape, density and concentration.

Inevitably, densities between seeding particles and the fluid particles in the surrounding medium are diverse and this will lead to a delay response to any acceleration in the fluid. Therefore, it is essential to know how well the motion of the seeding particles matches the fluid motion.

Some important equations to describe this problem are:

$$St = \frac{\tau_p}{\tau_f}. \tag{2.28}$$

The capability to follow the fluid motion is characterized by a dimensionless index, the Stokes number St, which compares the reaction time of the fluid τ_p with the one of the particle τ_f.

$$\tau_f = \frac{l_c}{u}. \tag{2.29}$$

The reaction time of the fluid τ_f is the characteristic length lc divided by the velocity u.

$$\tau_p = \frac{d_p^2 \rho_p}{18\mu_p}. \tag{2.30}$$

The reaction time of the particle τ_p is based on Stokes's law which is applicable to flows with small Reynolds numbers.

$$v_p - U = \frac{d_p^2(\rho_p - \rho_f)dv_p}{18\mu_f \, dt}. \tag{2.31}$$

The velocity U of the fluid is not identical with the velocity v_p of the particle. The difference can be calculated as seen in the equation above. Note that with a higher density also

$v_p - U$ is higher. D_p is the cross section of the tracer, ρ_p the density of the particle, ρ_f the density of the fluid and μ_f is the dynamic viscosity of the fluid [14].

Seeding particle concentration

In the interrogation regions of the image the density of the seeding particles is a crucial factor. On the one hand, at too high densities the particles start to overlap, and single particle images will be replaced by a speckle pattern due to interference of the light scattered. The displacement of the accumulation of particles can be calculated by statistical analysis of the speckles, also known as Laser Speckle Velocimetry (LSV). However, two-phase flow effects can occur when the particle concentration is too high, because of possible interference between the fluid and the particles.

On the other hand, if the seeding density is so low that the average particle displacement between images is less than the mean distance between particles, the motion of each particle is tracked using Particle Tracking Velocimetry (PTV). But this could result in missing velocity information in some areas because at low particle concentrations some image areas may not contain particles.

In summary, for optimal spatial resolution of a region of flow using PIV, the concentration of particles should be low enough to separately identify each particle but high enough to provide numerous data points in each interrogation area without interference [14]

2.3.3 Light scattering

In order to be detected by the camera, the particles must scatter enough light. The intensity of light scattered depends highly on the particle size and angle of observation.

If the particles have a greater diameter than the wavelength of the incident light, which is common for PIV, Mie's scattering theory can be applied.

As the particle diameter increases, so does the number of local maxima of the scattered Light between 0° (pure backward scattering) and 180° (pure forward scattering) corresponding to:

$$q = \frac{\pi d_p}{\lambda} \tag{2.32}$$

where q is a normalized diameter and λ the wavelength of the incident light. In addition, the direct comparison shows that the intensity ratio between forward and backward scattering also increases with increasing particle diameter. Although figure 2-5 and Figure 2-6 show that forward scattering is well suited, the limited depth of field of the optical components used typically results in side-scattering (90°) PIV images. With the usage of larger particles, brighter images can be produced, but at the expense of the particle response to the fluid motion. Also, the particles concentration can be raised, resulting in an increase of the background noise. The challenge here is to reach a satisfying compromise between the size parameters.

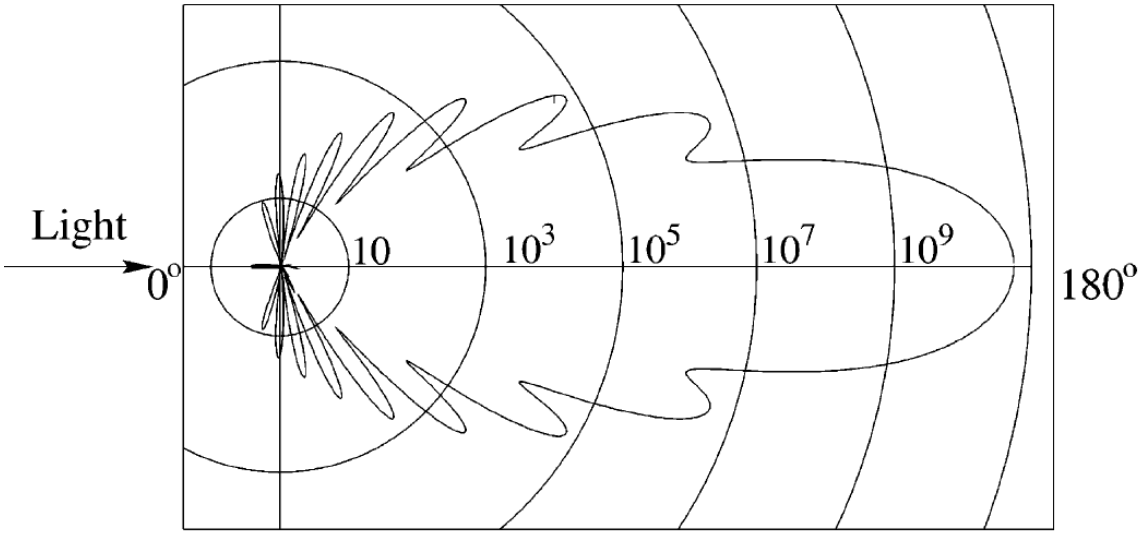

Figure 2-5: Light scattering by a 1 μm glass particle in water [Raphael].

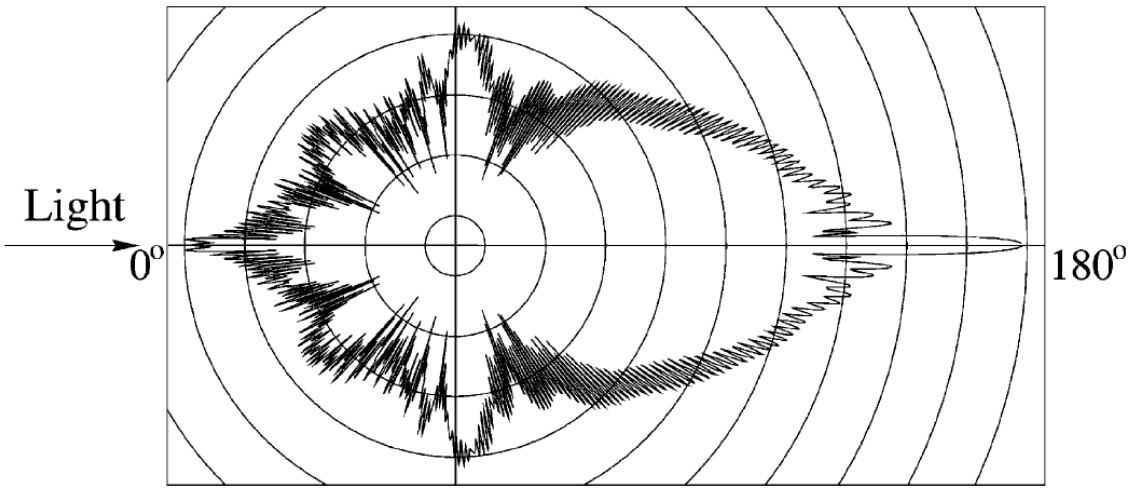

Figure 2-6: Light scattering by a 10 μm glass particle in water [Raphael].

2.3.4 Cross-correlation

Cross-correlation represents the mathematical basis of the PIV evaluation. To this end, it is necessary to divide the image into sections, so-called interrogation windows, which are located on the image plane. Due to the finite thickness of the light section, these areas in the measurement plane have a certain extent in the z-direction and represent very small volumes. Within a control volume is a certain number N of particles that are randomly distributed and their state at a certain time t is described as follows:

$$\Gamma = \begin{pmatrix} \vec{X}_1 \\ \vec{X}_2 \\ \vdots \\ \vec{X}_N \end{pmatrix}; with\ \vec{X}_i = \begin{pmatrix} X_i \\ Y_i \\ Z_i \end{pmatrix}. \tag{2.33}$$

$\vec{X}_i$ describes the position of a particle i at a certain time t. In the following, capital letters are used for the description regarding the light section and lowercase letters for the description relating to the image plane. Furthermore, for the sake of simplification, it is assumed that the position of the particles and that of the image are linked by a constant magnification factor M such that the following applies:

$$X_i = \frac{x_i}{M} \tag{2.34}$$

$$Y_i = \frac{y_i}{M}. \tag{2.35}$$

The interrogation volume in the light section plane is mapped to an interrogation area in the image plane. There, the intensities I (1st image) and I' (2nd image) are determined in the form of gray levels.

Now particle groups of the first image are correlated with those of the second image. This happens because within the interrogation area in image 1, a particle group (separation area), which is usually half the size of the interrogation area, is selected and in image 2 within the interrogation area it is shifted so that the sums on the product of the intensities $I * I'$ become maximal.

$$R_{II}(x,y) = \sum_{i=-K}^{K} \sum_{i=-L}^{L} I(i,j)I'(i+x, j+x). \tag{2.36}$$

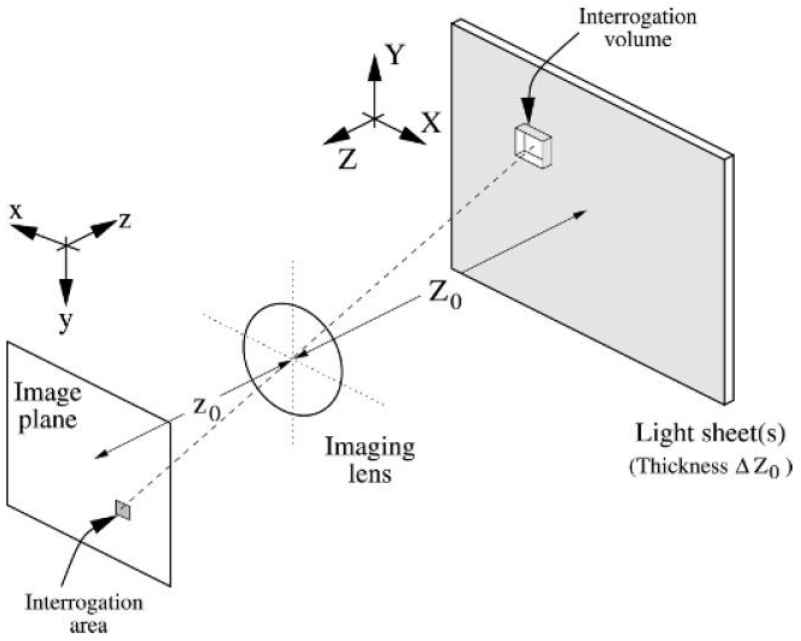

Figure 2-7: Schematic representation of geometric imaging [10]

Figure 2-8 on the right shows the shift of the separation area (image 1) within the interrogation area (image 2) and the resulting cross-correlation plane. Due to the different possibilities of moving the 4 × 4 separation area within the 8 × 8 interrogation Area, a 5 × 5 cross-correlation area is created. Since up to several thousand displacement vectors have to be determined in a PIV recording, a more efficient approach is needed to calculate the cross-correlation function. This more efficient approach is based essentially on the Fast Fourier Transformation (FFT) and the correlation theorem [10].

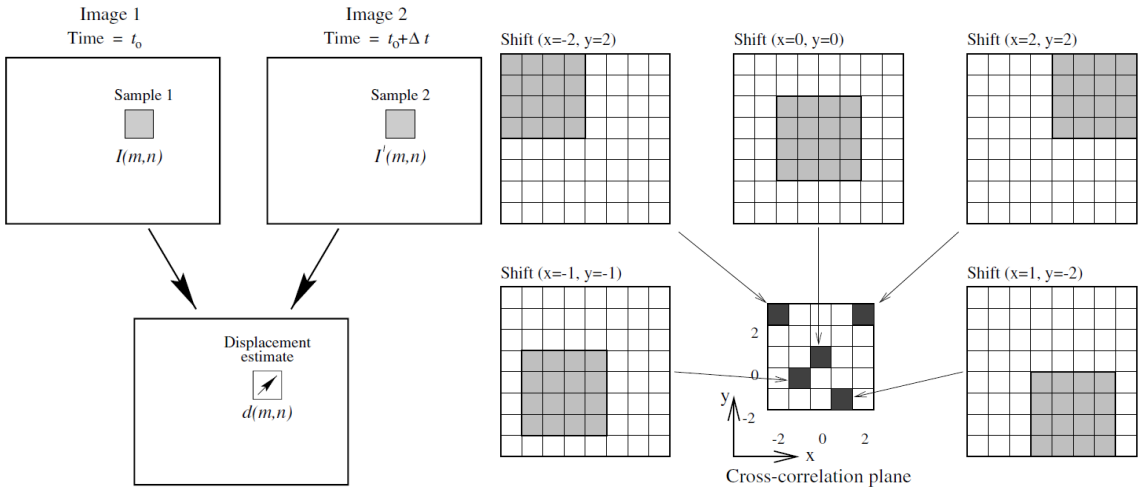

Figure 2-8: Concept of cross-correlation for double frame / single exposure [10]

3 Experimental set-up

As part of this thesis a centrifugal fan is investigated. In this chapter the general set-up of the test bench and its components will be discussed. Also, a brief explanation of how the efficiency and characteristic curve are determined. Lastly, the set-up of the PIV experiment is displayed.

3.1 Test bench

This chapter serves to get to know the test bench in its functionality. It explains the mechanical components that are important for the function and their arrangement in the overall system.

The overall system on which the experiments are carried out represents a closed cycle. This favors the PIV measurement because it uses seeding with DEHS tracer particles. The particles can remain in the closed loop and can be used continuously. To ensure a steady flow before entering the inlet section, a volume with a very large cross-section, the so-called settling chamber, is used. Figure 3-1: Test bench shows the schematic structure of the test bench. The test object, the impeller, is located in the volute housing. It is powered by an electric engine, which is marked in the figure with "engine". The electric engine is connected to the impeller via drive shafts and a measuring shaft. The engine, drive shafts and measuring shaft are referred to as drivetrain. The blue arrows indicate schematically the flow direction of the air. The rotated impeller draws air from the axial direction and conveys it radially upwards into the outlet shaft. There, the fluid is passed further into the volume flow measuring section. This measuring section includes the measuring orifice, which is discussed in more detail in 3.1.2. Afterwards, the fluid passes through the adjustable throttle. It serves to shift the operating point in the direction of smaller volume flows. After the throttle, the air enters the settling chamber, in which the auxiliary blower is located. It can be regulated in its speed and has as well as the throttle the task to move the operating point of the turbomachine. However, the auxiliary blower shifts the operating point towards larger volume flows. Furthermore, in the settling chamber sieves are attached, which serve to resolve larger disturbances [9] [11].

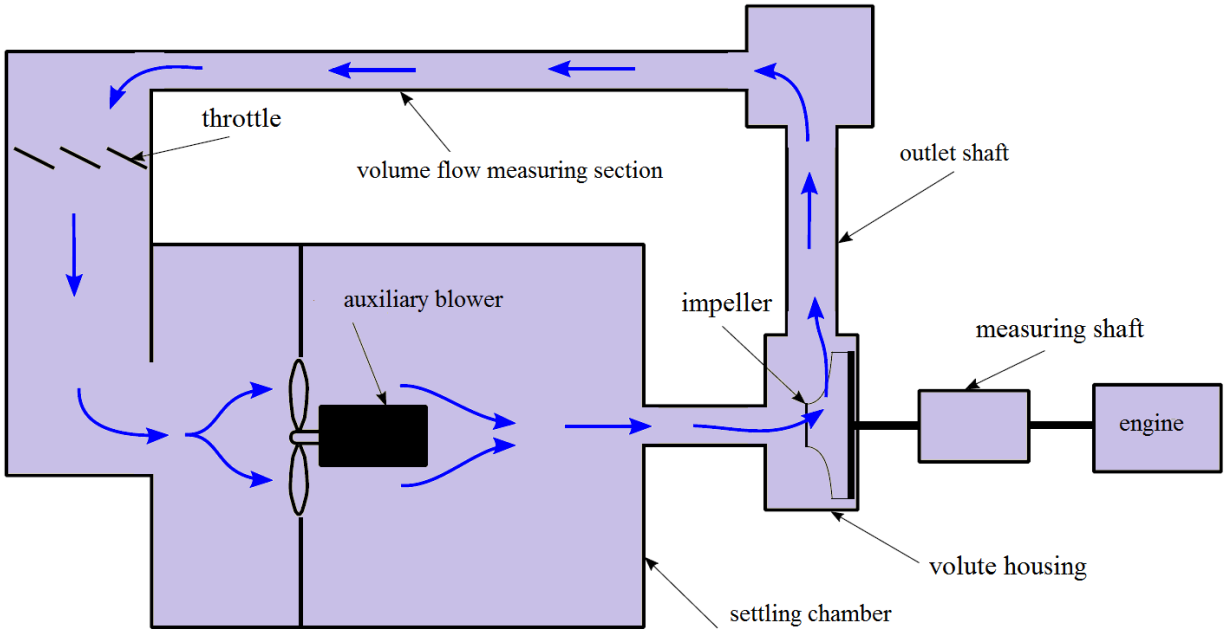

Figure 3-1: Test bench

Table 3-1 below lists some important geometrical data about the test bench and the impeller. These values are used in some calculations and considered to be given.

DESCRIPTION	VALUE	UNIT
CROSS SECTION OUTLET SHAFT	0,0219	$[m^2]$
NUMBER OF VANES (IMPELLER)	9	$[-]$
CROSS SECTION IMPELLER INLET	0,016	$[m^2]$
DIAMETER OF IMPELLER AT INLET	0,138	$[m]$
CROSS SECTION IMPELLER OUTLET	0,023	$[m^2]$
DIAMETER OF IMPELLER AT OUTLET	0,325	$[m]$
WEIGHT OF IMPELLER	2,4	$[kg]$
INNER DIAMETER OF ORIFICE	64/76	$[mm]$

Table 3-1: Dimensions of test bench and impeller

Axial gap covering

The axial gap coverage s is a geometric size. As shown in Figure 3-2, it is the axial distance between the edge of the stationary inlet nozzle facing the impeller and the edge of the suction nozzle from the impeller. The volume flow that flows through this gap depends on the gap coverage. This volume flow represents a leak and thus has an influence on the efficiency. The gap coverage is not varied in the context of this work, but adjusted to a fixed level as tested by *B. Driedger* [9].

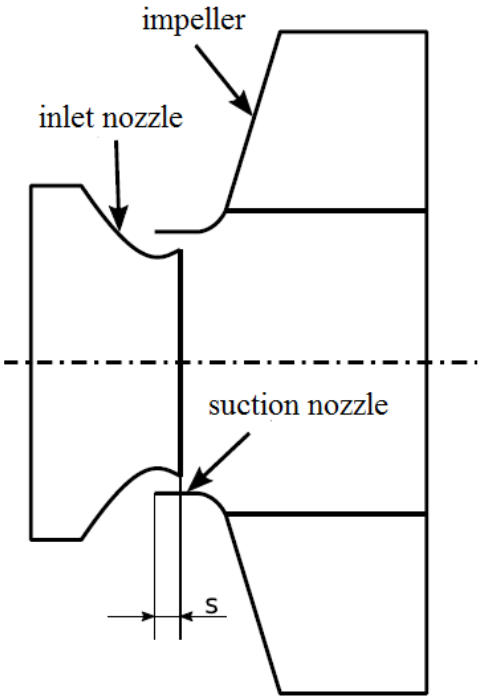

Figure 3-2: Axial gap

3.1.1 Calculation of the efficiency

In this sub-chapter the procedure of the determination of the fan's efficiency will be explained.

At first, the static pressure difference $\Delta p_{stat,1}$ is measured between the static pressure in the settling chamber and in the outlet shaft. In addition, the static pressure difference $\Delta p_{stat,2}$ is measured over the measuring orifice. With the help of $\Delta p_{stat,2}$, the volume flow can be calculated. This calculation will be discussed in the following chapter 3.1.2. The pressure changes are very small in relation to the absolute ambient pressure. For this reason, a constant density can be assumed for the following calculations. The total pressure is given by:

$$p_{tot} = p_{dyn} + p_{stat} = \frac{\rho}{2} c^2 + p_{stat} \tag{3.1}$$

with c being the flow velocity and ρ the density.

The density of air at ambient pressure and the flow velocity can be calculated with:

$$\rho_{amb} = \frac{p_{amb}}{R \cdot T_{amb}} \tag{3.2}$$

and

$$c = \frac{\dot{V}}{A}. \tag{3.3}$$

The efficiency η in general is the ratio between benefit and effort. Here it results in:

$$\eta = \frac{\Delta p \cdot \dot{V}}{P_{shaft}}. \tag{3.4}$$

In turn the shaft power is:

$$P_{shaft} = M_{imp} \cdot 2\pi n. \tag{3.5}$$

Considering and applying all the assumptions, equations and losses of the system the total efficiency is [11]:

$$\eta_{tot} = \frac{[\Delta p_{stat,1} + \frac{p_{amb}}{2 \cdot R \cdot T_{amb}} \cdot (\frac{\dot{V}}{A})^2] \cdot (\dot{V}_{orifice} + \dot{V}_{leak})}{(M_{engine} - M_{friction}) \cdot 2\pi n}. \tag{3.6}$$

3.1.2 Calculation of the volume flow

The volume flow determined indirectly by the static pressure difference across the measuring orifice. This measurement is carried out according to DIN EN ISO 5167. The mentioned standard contains both the design features of the measuring orifice and the calculation specification. The procedure takes place iteratively [12]. The volume flow is:

$$\dot{V} = \frac{\dot{m}}{\rho}. \tag{3.7}$$

and the mass flow $\dot{m}$:

$$\dot{m} = \frac{C}{\sqrt{1-\beta^4}} \epsilon \frac{\pi}{4} d_{orifice}^2 \sqrt{2\Delta p_{orifice} \rho}. \tag{3.8}$$

The expansion number ϵ can be calculated or be looked up in a table [DIN]. The diameter number β results in:

$$\beta = \frac{d_{inner,orifice}}{D_{outer,orifice}} \tag{3.9}$$

and needs to be within $0{,}75 \geq \beta \geq 0{,}1$. Finally, the calculation of the flow rate coefficient C is rather complicated and will not be discussed in detail. It is basically a function of the Reynolds number, which itself is a function of the flow rate, therefore the whole procedure, as mentioned above, is iteratively. It needs to be noted that in this thesis β will be slightly bigger than $0{,}75$ but it has no influence on the correctness of the calculation. Please refer to [12] for more details.

3.1.3 Losses

Every technical system has different kind of losses. The measured data often does not include them and therefore they have to be calculated separately. The sensors installed do not consider two of the main losses: frictional torque in the powertrain ($M_{friction}$) and leakage ($\dot{V}_{leak}$) within the closed circuit. Their great influence can be seen in the equation of the total efficiency (3.6).

3.1.4 Frictional torque

The friction of a rolling bearing is composed of several parts (see table 3-2). Due to the large number of influencing variables, such as the dynamics in speed and load, the friction torque is not a trivial value to calculate [19].
The radial force is mainly caused by the gravitational force by shaft and impeller. They will be determined experimentally.
On the other hand, the axial forces occur due to change of momentum in the impeller caused by the out-flowing fluid. This was done mathematically by *D. Sauerer* in his thesis by using the conservation of momentum equation. The result was that at $1200\,\frac{r}{min}$, which is the maximal testing speed, the friction torque caused by axial force is $0{,}00092\ Nm$. Relatively to the absolute torque that is 0,38 %.

To determine the radial force, a rotationally symmetrical weight was produced with the mass of the impeller and then mounted instead of the impeller on the main shaft. The torque then is measured at different speeds in order to see if there is a dependency. Figure 3-3 shows the results of the tests. The black plot is with the weight and the red one without. It

can be observed that the torque and speed are dependent. With increasing speed, the torque also increases. However, the influence of the weight force is not dependent of the speed and has little influence.

Both, radial and axial caused friction torques are added and used in the equation to calculate the efficiency.

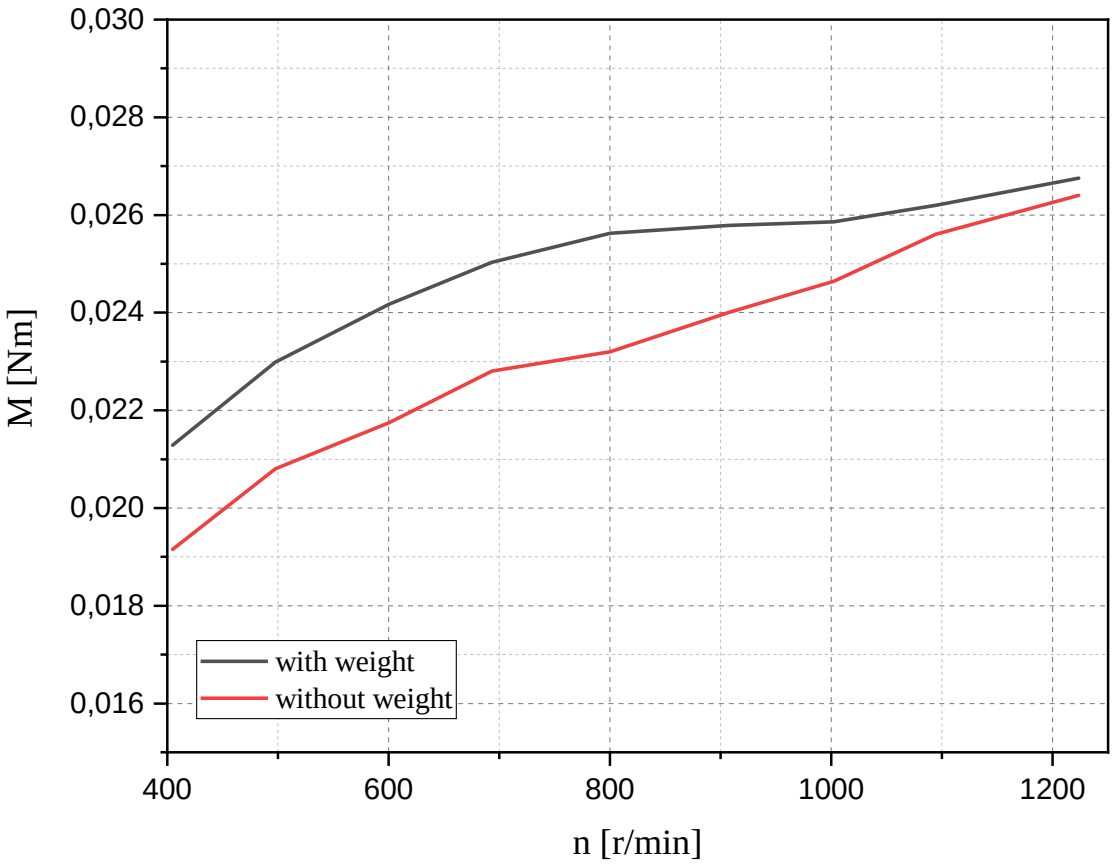

Figure 3-3: Friction torque comparison

FRICTION	INFLUENCE VARIABLE
ROLLING FRICTION	Size of the load
DYNAMIC FRICTION OF ROLLING ELEMENT OR CAGE	Size and direction of load, speed and lubrication
FLUID FRICTION	Design and speed
SEAL FRICTION	Design and pretension of the seal

Table 3-2: Friction parts [19]

3.1.5 Leakage

A full leakproofness is almost impossible in any technical system. Due to the difference between the pressure inside the test circuit and the ambient pressure outside, air is flowing

outside to equalize the pressure difference. This volume flow is not detected by the measuring orifice, thus falsifying the results. Therefore, in this chapter the leakage is determined to correct the volume flow measurement.

In this work the same leakage test was conducted as done by *D. Saurer* [11]. Essentially, the measuring test section is divided and one open end is sealed and the other is connected to a vacuum cleaner, which is regulated by a transformer. The static pressure difference across the orifice and between outlet shaft and ambiance are measured.

When the vacuum cleaner is switched on, a negative pressure is generated in the system. The higher ambient pressure pushes air from the outside through gaps and other leaks into the test bench. This airflow is passed through the orifice before passing the vacuum cleaner. The power of the vacuum cleaner is varied step by step. As a result, different pressure differences are generated. Thus, the pressure differences at the metering orifice are converted into the corresponding volume flows. A fixed leakage flow can be assigned to each pressure difference to the environment by use of a regression model [11].

Before performing the test, the entire test bench was checked again for leaks and critical spots were sealed as good as possible. As shown in figure 3-4 a slightly better leakproofness is achieved. At the operating point (600 r/min) the leakage is 1,3 % of the absolute volume flow, in comparison to 1,6 %.

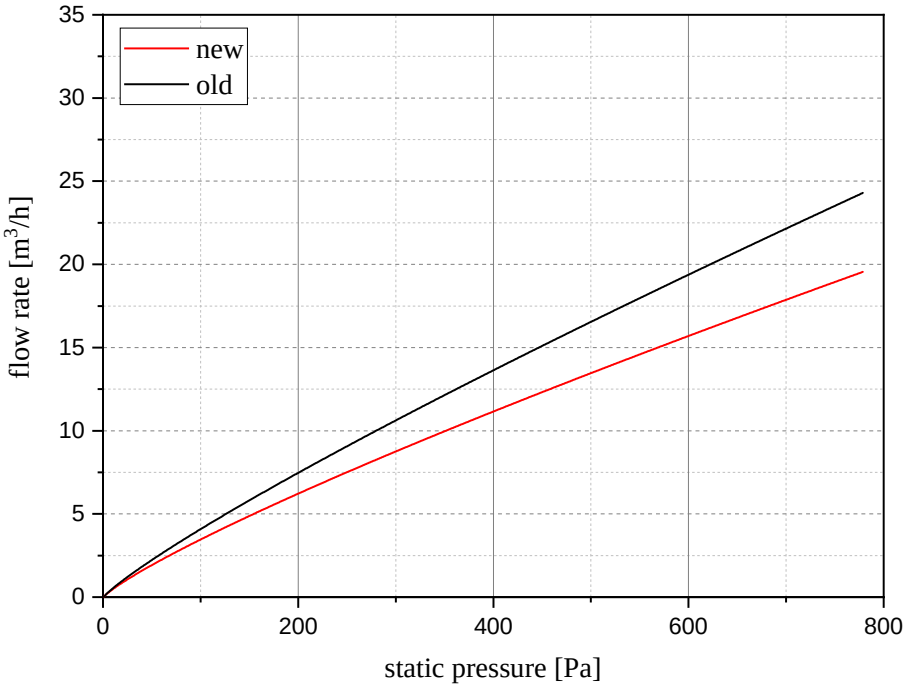

Figure 3-4: Leakage test

The problem with the concept of this test is that the leakage in the entire system is measured, but there is no way of knowing where it comes from. However, only leakage between the measuring orifice and suction nozzle is relevant to the test results. Nevertheless, the test shows that the overall leakage is small relative to the absolute flow rate.

Therefore, another leakage test was done which set-up is shown in figure 3-5. This time the test bench is sealed at the outlet shaft (2) and at the suction nozzle (1). Through a pressure bore the system is inflated with an air pump. After reaching 200 Pa the air pump is unplugged and the pressure bore sealed. The pressure is plotted over time to see how fast it decreases. The idea is that the time is an indicator for the leakproofness. The result is displayed in figure 3-6. After one hour the pressure has decreased to 195,25 Pa which corresponds to a 2,37 % pressure drop.

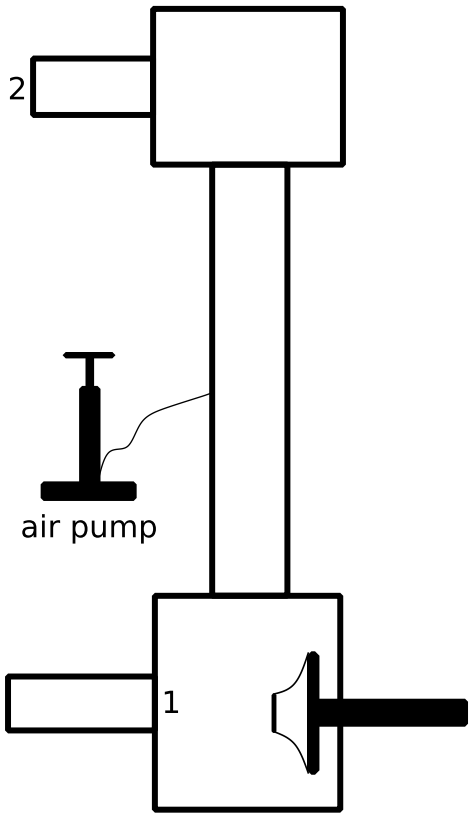

Figure 3-5: Schematic set-up

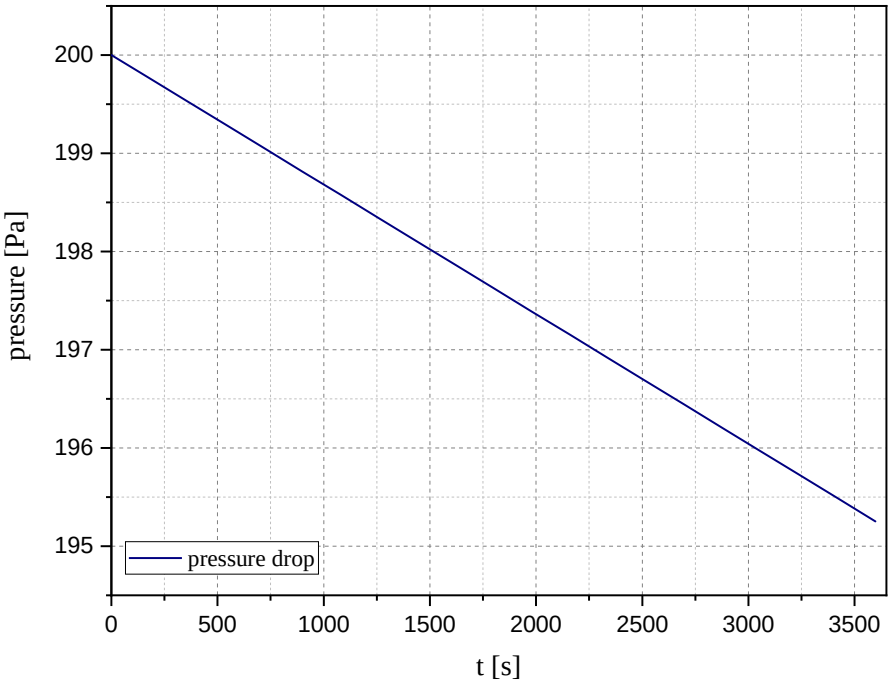

Figure 3-6: Pressure drop

Combining the two tests, the test bench can be assumed leakproof and the test results accurate.

3.1.6 Modifications to the powertrain

As part of the thesis of *D. Sauerer* the powertrain was improved significantly because the torque fluctuations and the friction torque where too high. Figure 3-7: Old powertrain shows the old powertrain.

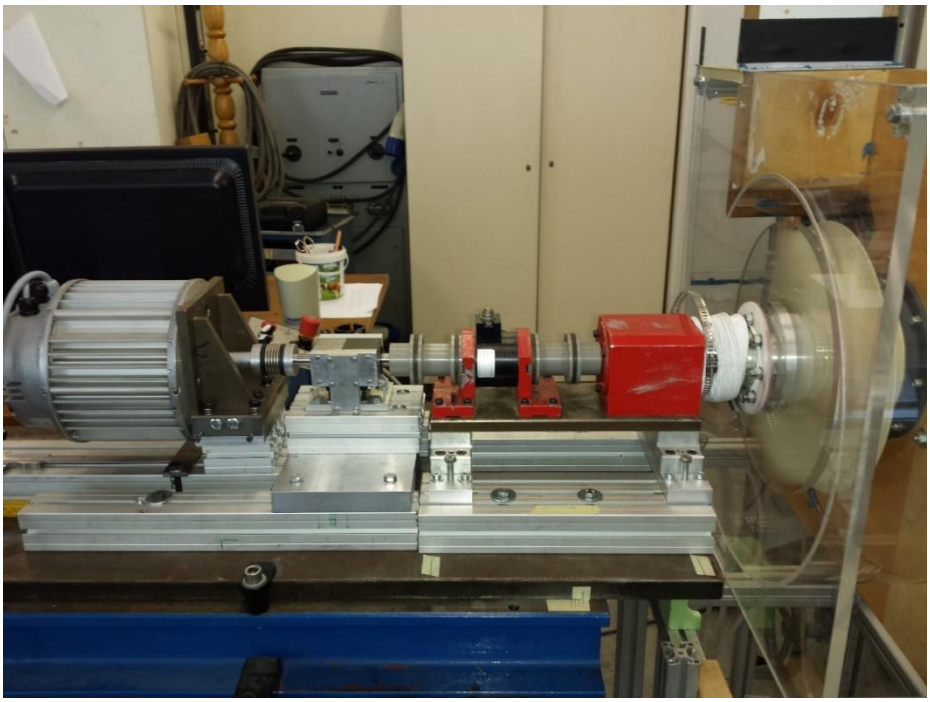

Figure 3-7: Old powertrain

To optimize torque fluctuation even more, the powertrain was shortened even more to its rudimentary components as figure 3-8 displays. The spring washer coupling between measuring shaft and main shaft was removed and a metal bellows coupling built in. The motor and measuring shaft are also connected with a metal bellows coupling, which is a flexible coupling for transmitting torque between two shafts while allowing for angular misalignment, parallel offset and even axial motion, of one shaft relative to the other.

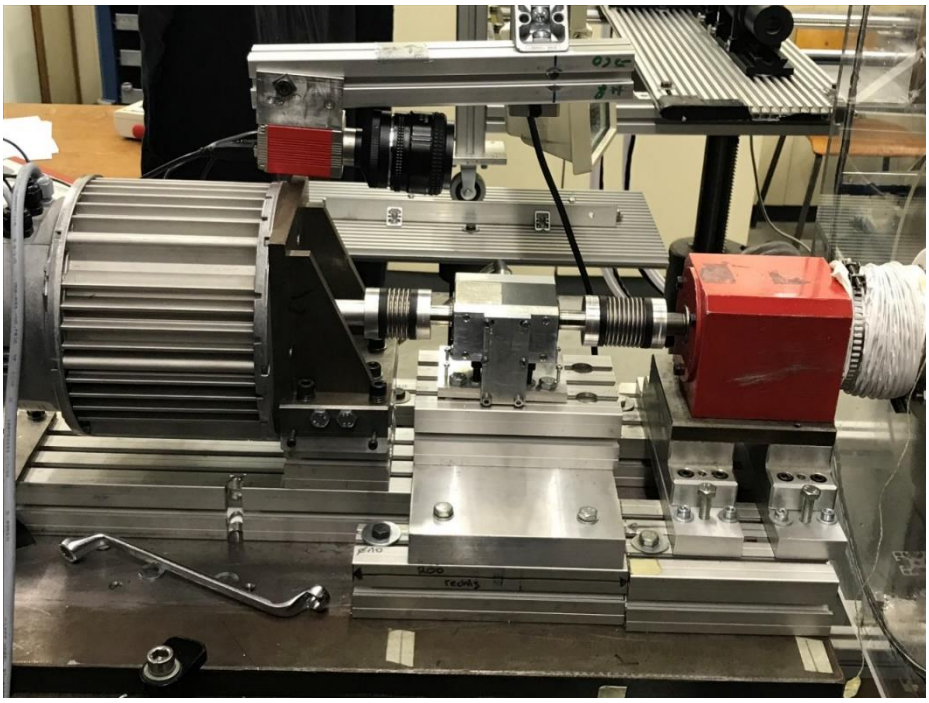

Figure 3-8: New powertrain

The alignment of the shafts to each other plays an important role. Just like the motor, the measuring and main shafts can also be precisely aligned using adjusting screws. The alignment was done as good as possible by means of trial and error. This process was very time consuming and the results were satisfying but the perfect alignment was not found. For future work it would be advisable to let an external company do the alignment professionally.

Figure 3-9 compares the friction torque and fluctuations of the old powertrain and the new one. A slightly optimization is observed as the friction torque decreased 15 % from an average 0,02 Nm to an average 0,017 Nm at 1200 r/min.

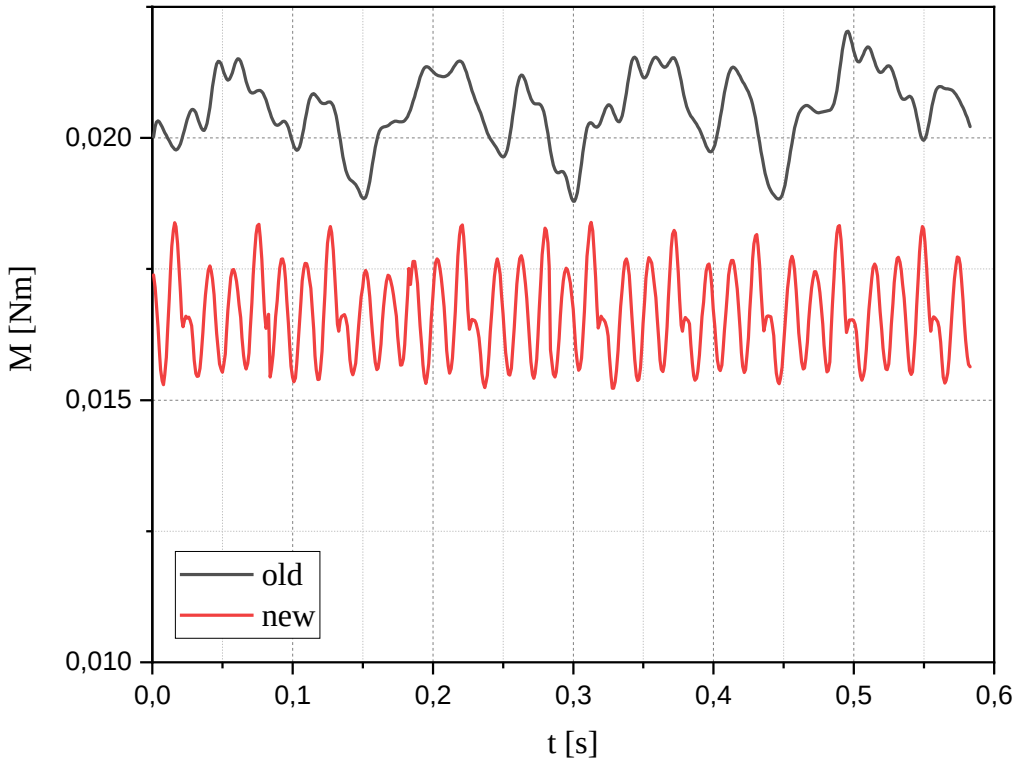

Figure 3-9: Friction torque comparison

Changing the lubricant

Lastly, the lubrication of the bearings was changed from grease to oil. The expectations or aim were that the friction torque reduces. However, no significant changes are observed as displayed in figure 3-10. At low speeds up until 1000 r/min the friction torque is lower, at higher speeds the friction is even higher than before. Also, with oil lubrication every few hours and before every experiment it had to be lubricated. Finally, the bearings were knocking after a few weeks which indicated a defect and new bearings were bought and lubricated with grease again.

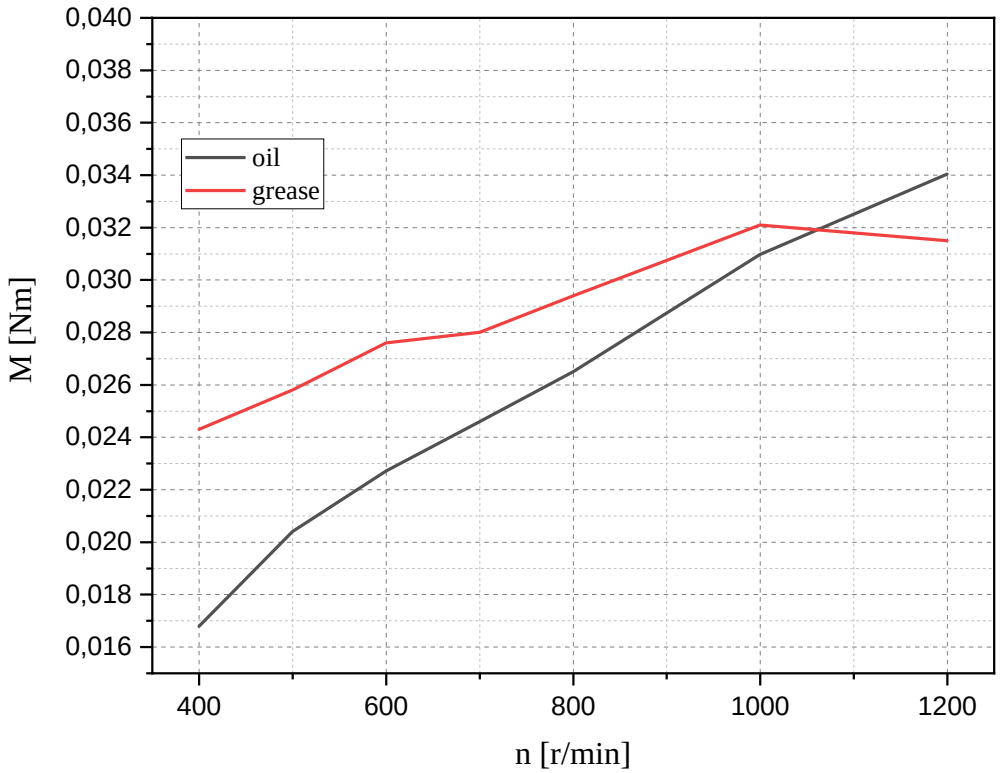

Figure 3-10: Lubricant comparison

3.2 Measurement instrumentation

The aim of this test bench is to determine the fan's characteristic curve, efficiency and analyze the velocity fields via particle image velocimetry. To do this different measurement instrumentation is needed. This chapter will give an overview of the most important components.

3.2.1 Set-up for efficiency and characteristic tests

For the examination of the fan's efficiency and characteristic curve pressure, temperature, torque and flow rate need to be measured. Figure 3-11 shows schematically the necessary sensor technologies. The data from the sensors will be transferred to the data acquisition module and afterwards to the computer. To calculate the flow rate, the static pressure difference before and after the orifice is measured. The static pressure difference between outlet shaft and settling chamber is used to calculate the pressure increase in the turbomachine. The temperature of the air is measured inside of the test bench to take into account the variation of the density. At last, the measuring shaft sends two quantities, torque between motor and drivetrain and rotational speed. All signals are analogue except for the rotational speed signal, it is a digital one. The data acquisition module converts the analogue signals to digital signals and sends them to the computer. On the computer the data are saved and evaluated with the help of suitable software.

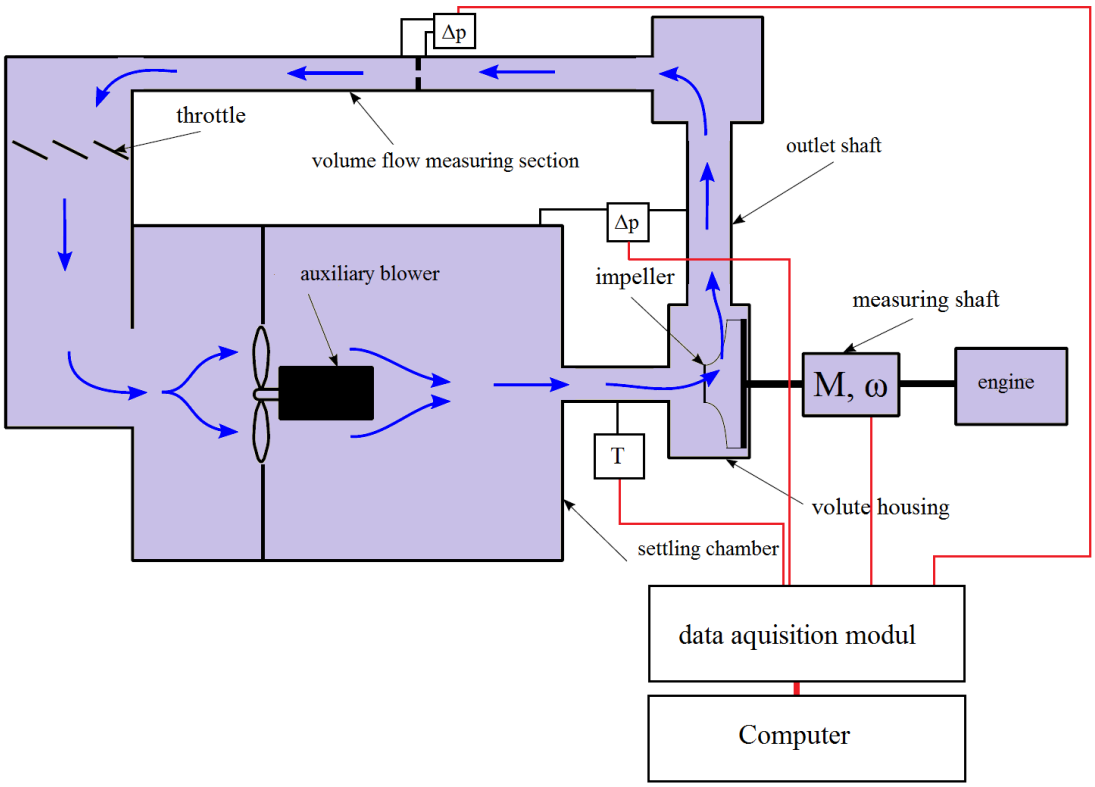

Figure 3-11: Measurement instrumentation

3.2.1.1 Measuring shaft

The task of the measuring shaft is to determine the torque between drivetrain and motor and send it as a digital signal to the data acquisition module. This measuring shaft was selected and calibrated in previous theses [9] [11]. In the following table 3-3 the most important data for it are shown:

DESCRIPTION	INFORMATION
MANUFACTURER	HBM
TYPE	T20WN
TORQUE RANGE	-5 Nm – 5 Nm
SPEED RANGE	3000 $1/min$
OUTPUT SIGNAL TORQUE	-10 V – 10 V
OUTPUT SIGNAL SPEED	5 V, 360 $impulses\ per\ revolution$
NOMINAL SPEED	10000 r/min

Table 3-3: Data sheet measuring shaft

3.2.1.2 Pressure sensors

As explained above for determining the fan's efficiency and characteristic curve two pressure sensors are needed. One for the pressure difference at the orifice and the other between

settling chamber and outlet shaft. The dimensioning of the pressure sensor technology was done by previous theses [9]. As part of this thesis the calibration of the zero-defect value was determined and pressures compared with the ones from Betz manometer's [A 1]. The slope of the function is given by the measurement range and the output voltage and is 100 $\frac{Pa}{V}$. In order to calculate the zero-defect value, the output voltage is plotted in an unloaded state for several seconds. This procedure was done serval times during the experiments. In figure Z an example of the voltage – time plot of the pressure probe is shown. From this plot the mean value is calculated and in the following measurement subtracted from the output voltage.

This adds up to the transformation equation for voltage:

$$\Delta p(U) = (U - 0{,}0003) \cdot 100 \frac{Pa}{V}. \tag{3.10}$$

To ensure and control the sensors during the experiment, the pressures were compared to the ones from Betz manometers. These are very reliable and are based on the principle of conventional pressure gauges.

The comparison shows that the difference between the measurement results is $\mp 1{,}5\%$ and is therefore within the measuring inaccuracy of the pressure gauges. In table 3-4 are essential information gathered.

DESCRIPTION	**INFORMATION**
MANUFACTURER	Kalinsky Sensor Elektronik GmbH
TYPE	DS2
RANGE OF MEASUREMENT	0 Pa – 1000 Pa
OUTLET SIGNAL	0 V – 10 V
NOMINAL TEMPERATURE RANGE	-20°C – 50°C
NOMINAL VOLTAGE	24 V DC/AC $\mp 10\%$

Table 3-4: Data sheet pressure sensor

3.2.1.3 Temperature sensor

To capture the change in density caused by the variation of the air's temperature, a temperature sensor is installed. The sensor's resistance changes as the temperature changes and a transmitter sends an analogue signal to the data acquisition module. Table 3-5 shows important technical properties of the sensor.

DESCRIPTION	INFORMATION
PRODUCTION SERIES	PT100
TYPE	Plug-in resistance thermometer
TEMPERATURE RANGE	-50 $°C$ – 180 $°C$

Table 3-5: Data sheet temperature sensor

3.2.1.4 Data acquisition module

The data acquisition module gathers the incoming analogue signals and converts them into digital signals. Afterwards it sends them to the computer where the data are evaluated. In the following table 3-6 are technical data listed for the used module.

DESCRIPTION	INFORMATION
MANUFACTURER	National Instruments
TYPE	USB-6210
NUMBER OF ANALOGUE INPUTS	16 (single ended), 8 (differential)
MAXIMAL SAMPLING RATE	$\mp 10\ V$; $\mp 5\ V$; $\mp 1\ V$; $\mp 0{,}2\ V$
INPUT VOLTAGE	250 $\frac{kS}{s}$
RESOLUTION	16 bit
INTERFACE	USB

Table 3-6: Data sheet NI module

3.2.1.5 LabView (software)

LabView is a software product from National Instruments. The software converts the digital signals into the measured quantities, saves and writes them into an excel file and visualizes the data live on the monitor. It is possible to write small programs, called virtual instruments (VI), and change, add or manipulate the incoming data e.g. using filters. Figure 3-12: Control panel shows the control panel with all important live information.

Figure 3-12: Control panel

3.2.2 Set-up for PIV

In this thesis the velocity fields in the blade channels are investigated. The method to do this is the particle image velocimetry, which basics are discussed in chapter 2.3. In this chapter the set-up and components are described.

Figure 3-13 illustrates schematically the set-up and its relevant components.

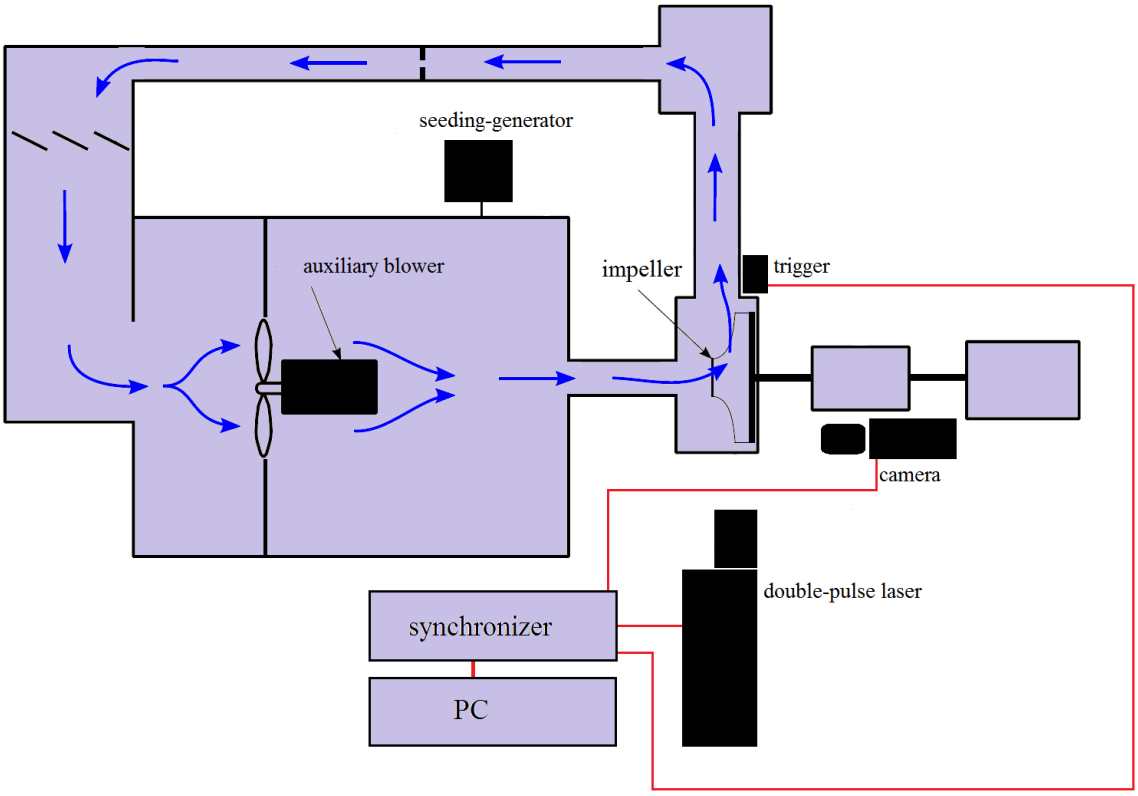

Figure 3-13: PIV set-up

3.2.2.1 Seeding-generator

The tracer particles used are drops of the liquid di-ethyl-hexyl-sebacate (DEHS). They are atomized using an atomizer from the manufacturer *PivTEC*. Controllers can be used to determine the number of nozzles used. In addition, the atomizer has a device for regulating the overpressure. The seeding generator creates the tracer particles and blows them into the circuit of the test bench, where they mix with the air. The removal of seeding particles must not be too close or too far away from the measuring point, because the size of the particles can still change during their transport through the air to the measuring point. Also, a bunching of the particles is possible at too long distances.

The generator used in this work creates liquid droplets and is connected to the settling chamber. The atomization within the generator is realized by compressed air.

The following table 3-7 shows important specifications.

DESCRIPTION	INFORMATION
MANUFACTURER	PIVTEC GmbH
OPERATING TEMPERATURE	5°C – 45°C
MAXIMUM STARTING OVERPRESSURE	2,5 bar
YEAR OF MANUFACTURE	2011
SIZE OF PARTICLE	0,9 μm – 2,3 μm []

Table 3-7: Data sheet seeding-generator

3.2.2.2 Laser system

The laser system consists of a neodymium-YAG double pulse laser *Twin BSL* of the manufacturer *Quantel laser*. It consists of two cavities whose laser beams are deflected by a mirror system onto a laser axis. The individual pulses are triggered by the synchronizer of the manufacturer *ILA Intelligent Laser Applications GmbH*. The laser exposes the particles generated by the seeding generator in the blade channel so that they can be detected by the camera. Controlled by the synchronizer, two impulses are emitted by the laser in quick succession at a certain position of the impeller.
Connected to the double pulse laser are the light sheet optics, which convert the laser beam to a plane. To avoid illumination of non-relevant components in the fan housing, the considered blade channels were painted black.

Table 3-8 shows some specifications of the laser system:

DESCRIPTION	INFORMATION
MANUFACTURER	Quantel
TYPE	Twin BSL 50
WAVE LENGTH	532 nm
POWER SUPPLY	ICE 450
FREQUENCY	15 Hz
ENERGY PER PULSE	50 mJ
OPERATING TEMPERATURE	10°C – 30°C

Table 3-8: Data sheet laser

3.2.2.3 Synchronizer

The synchronizer communicates with the laser and the camera and synchronizes them. If he receives a trigger signal through an external trigger, he triggers synchronously the camera and the laser pulse. In the setup of this work, the synchronizer does not control the camera directly. Instead, the signal will be passed to a PC with software installed to control

the camera. This in turn triggers the camera when the trigger signal is received. The Synchronizer itself is operated via a PC with control software. Some data are listed below.

DESCRIPTION	INFORMATION
MANUFACTURER	ILA GmbH
TYPE	Synchronizer 2011
NUMBER OF TRIGGER ENTRIES	6
NUMBER OF EXITS	12
SOFTWARE	Synchronizer Control 2012

Table 3-9: Data sheet synchronizer

For future reference a screenshot can be seen in figure 3-14 that shows the settings used in this work.

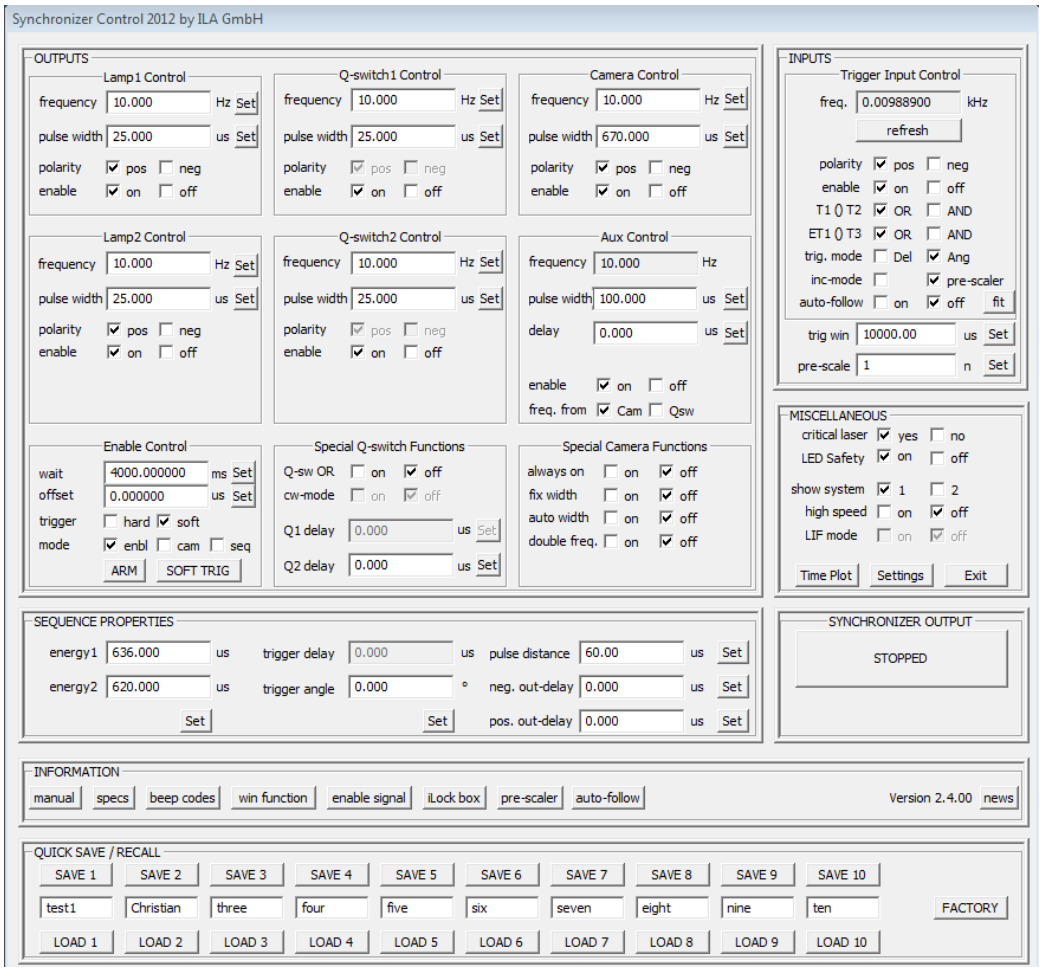

Figure 3-14: Synchronizer data

3.2.2.4 CCD-camera

The system for image acquisition consists essentially of the camera *pco.pixelfly USB* of the manufacturer *PCO*. There are 24-mm, 35-mm and 50-mm lenses available, however, in this thesis the 24-mm lens is used. Between lens and camera is a wavelength filter. It selects the range of the wavelength of the laser light. All other wavelengths are not picked up by the filtering. The triggering of the camera takes place, as in the case of the laser system, by a signal from the synchronizer.
Table 3-10 summarizes the main data of the camera.

DESCRIPTION	INFORMATION
MANUFACTURER	PCO
TYPE	SensiCam LongExposure
RESOLUTION	1376x1040 pixel
EXPOSURE TIME	1 ms – 1000s
DELAY TIME	0 s – 1000s
SOFTWARE	Camware

Table 3-10: Data sheet camera

3.2.2.5 Trigger

The trigger outputs a signal to the synchronizer depending on the position of the impeller. If the impeller passes through a fixed position, the trigger activates. It is attached to the volute casing by a bracket designed for this experiment (figure 3-15). Screwing in the screw releases the holder and unscrewing fixes the holder. A light source of the trigger radiates radially from outside to inside through the spiral housing, which consists of acrylic glass. On the outer surface of the hub of the impeller, a small reflective strip is glued. If the strip is under the trigger, the emitted light is reflected to the trigger. A light sensor in the trigger registers the reflected light, causing a signal to be emitted.

DESCRIPTION	INFORMATION
MANUFACTURER	CONTRINEX AG
TYPE	LTK 1120 303
MAXIMUM SWITCHING FREQUENCY	1000 Hz
MAXIMUM SWITCHING DISTANCE	300 nm
WAVE LENGTH OF LIGHT SOURCE	660 nm

Table 3-11: Data sheet trigger

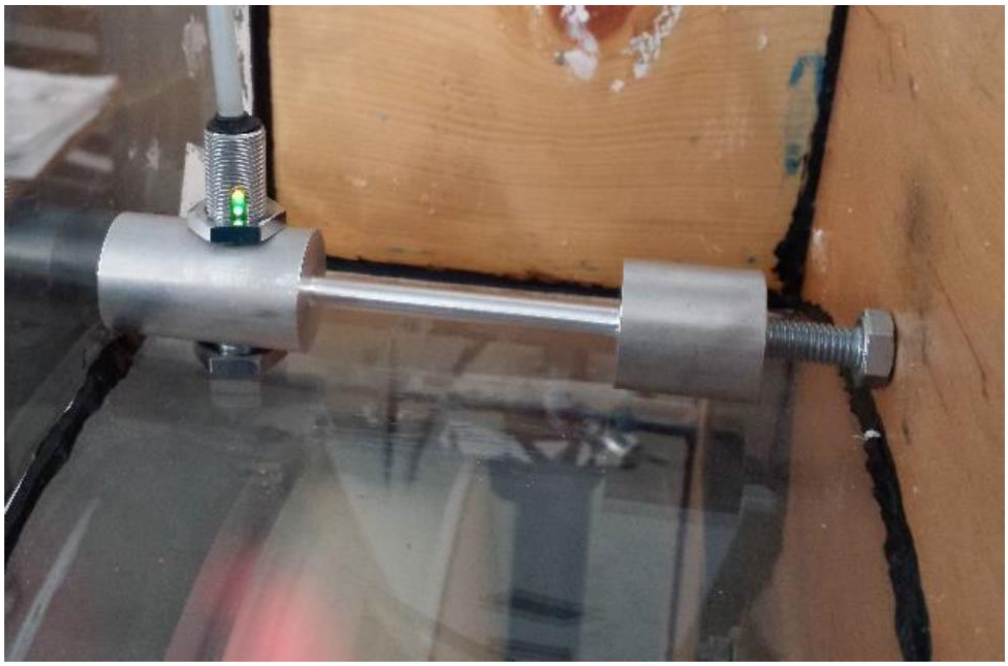

Figure 3-15: Trigger mounting

4 Characteristic curve and efficiency

In the following chapter the efficiency and the fan's characteristic curve are determined and compared to other experiments. Afterwards, the velocity field in the blade channel of the impeller is investigated by means of Particle Image Velocimetry.

As discussed in chapter 3.1, in order to determine the characteristic curve the operation points can be shifted with the help of the throttle and the auxiliary fan. The throttle can be closed gradually until there is no volume flow. The power of the auxiliary fan can also be increased gradually, while the throttle is open, to reduce the losses. The speed of the impeller is constant within a small tolerance. However, in order to check the scalability, the tests are performed at different speeds. Two measuring orifices with different inner diameters (63 mm and 77 mm) are used. A bigger diameter causes less flow resistance, thus higher flow rates can be achieved.
The measurement section duct's outer diameter was changed from $d = 80\ mm$ to $d = 100$ mm [A 6] in order to be able to measure higher flow rates while having a valid β [3.1.2].
The experimental results of the fan's characteristic curve and efficiency are compared to the experimental data of *D. Sauerer* [11] and the simulation data of *T. Rhode* [23].

4.1 Measuring results at 600 r/min

The first measurement was done at 600 r/min and with a 63-mm orifice. Figure 4-1 shows also the results from the simulation and the results from *D. Sauerer*, who used a 62-mm orifice and the old measuring section with an outer diameter of $d_{duct} = 80\ mm$.

At first glance the experiment shows a good compliance with the simulation and even a better compliance with the results from *D. Sauerer*. The full range of the characteristic curve could be measured up to a flow rate of $0{,}0914\ \frac{m^3}{s}$. In the first quarter of the plot both experimental data show a higher pressure increase compared to the simulation. Towards higher flow rates ($V \geq 0{,}065\ \frac{m^3}{s}$) the simulation predicts a slightly higher pressure increase than the experimental suggests.

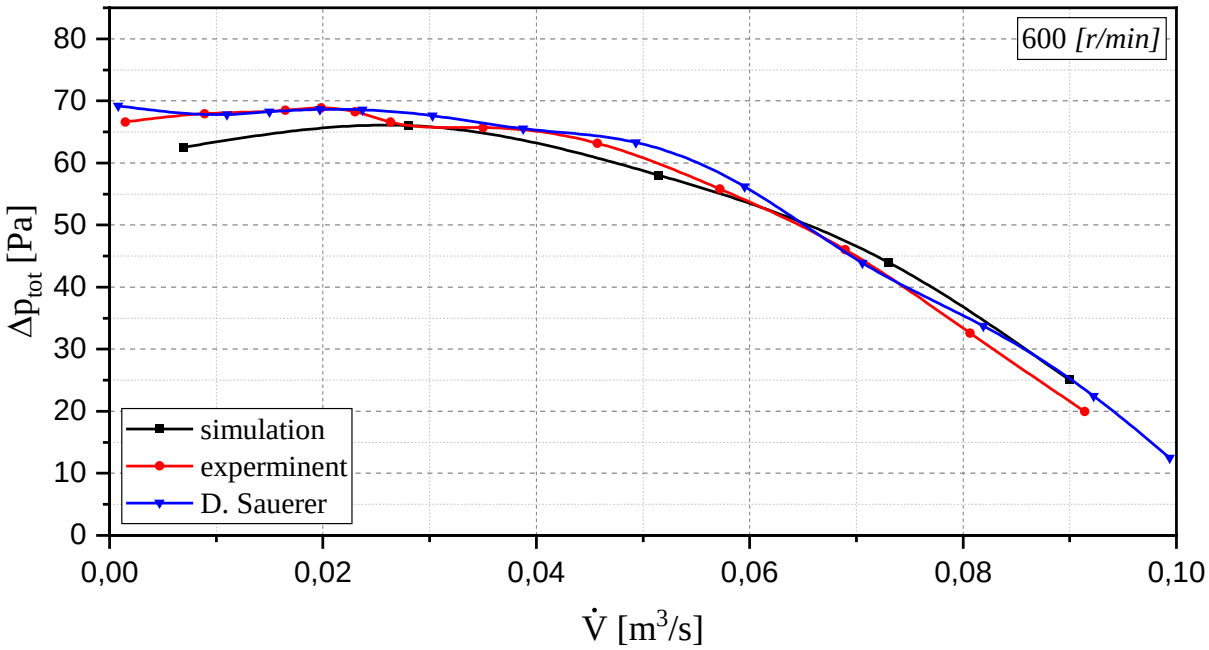

Figure 4-1: Characteristic curves at 600 r/min, 63-mm orifice

Corresponding to the characteristic curve, figure 4-2 displays the efficiency of the turbomachine. Again, in the first quarter of the plot all three results show a very good compliance. Only for very low flow rates ($V \leq 0{,}01\ \frac{m^3}{s}$) the compliance is bad. This could be caused by the low resolution in this region of the simulation. The experiment shows a slightly higher maximum efficiency of 75 % than the simulation predicts with 73 %. After the peak both experimental results decrease with a higher slope, thus falling under the predicted simulation efficiencies at flow rate greater than $0{,}063\ \frac{m^3}{s}$. The slump in the region of $0{,}06\ \frac{m^3}{s} < \dot{V} < 0{,}08\ \frac{m^3}{s}$ in the work of *D. Sauerer* could not be confirmed as it shows an almost constant negative gradient.

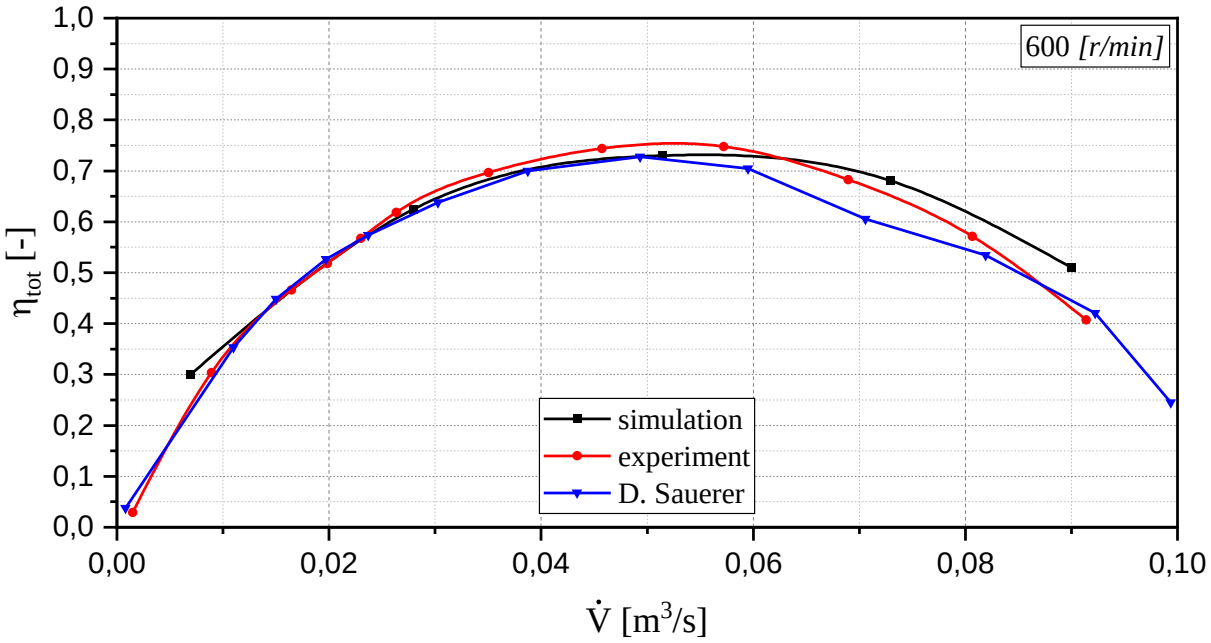

Figure 4-2: Efficiency at 600 r/min, 63-mm orifice

The figure below shows the fan's efficiency measured with a 77-mm orifice. It can be confirmed that also here the curve is decreasing steeper than the simulation suggests at $\dot{V} \geq 0{,}06\ \frac{m^3}{s}$. In the range of $0{,}02\ \frac{m^3}{s} < \dot{V} < 0{,}06\ \frac{m^3}{s}$ both graphs are almost congruent. At very small flow rates the graphs differ again strongly. The simulation has only one measurement point in this region and therefore it is difficult to compare. Maximum efficiency is almost identical to the simulation with 74 % and 73 %, respectively. In both cases the maximum efficiency is reached at a flow rate of $\dot{V} \approx 0{,}068\ \frac{m^3}{s}$, however, due to the resolution it is hard to locate the exact position.

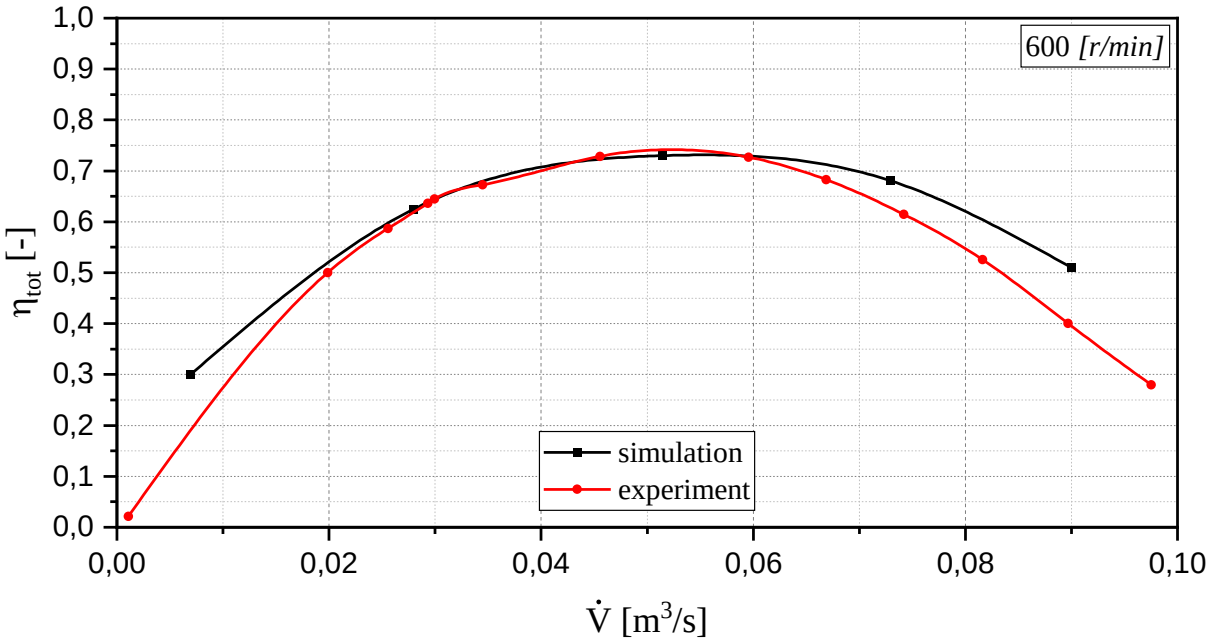

Figure 4-3: Efficiency at 600 r/min, 77-mm orifice

4.2 Measuring results at 1000 r/min

This measurement was done with a 63-mm and 77-mm orifice. The results are compared with *D. Sauerer's* data, which was measured with a 62-mm orifice and a smaller measurement section outer diameter. Simulation data are scaled with the help of the affinity laws described in chapter 25, because data for 1000 r/min are not existent. In figure 4-4 can be observed that the experimental data measured with different orifices are very similar. Solely the measurement of *D. Sauerer* seems to have an outlier at $\dot{V} = 0{,}1\ \frac{m^3}{s}$. By using the 77-$mm$ orifice, a much higher flow rate can be achieved. In comparison to the 63-mm orifice the flow rate is 68,5 % higher and the pressure increase lowered by 57,9 %.

The simulation data predict a lower pressure increase in the range of $0\ \frac{m^3}{s} < V < 0{,}09\ \frac{m^3}{s}$. After $\dot{V} \geq 0{,}1\ \frac{m^3}{s}$ the experimental data subtends the simulation's graph and proceeds under it. Even with the 77-mm orifice the pressure increase can only be decreased to 92 Pa and a maximum flow rate of $0{,}134\ \frac{m^3}{s}$ achieved. A possibility for future experiments to reach higher flow rates, is to boost the power of the auxiliary fan, thus reducing the losses more.

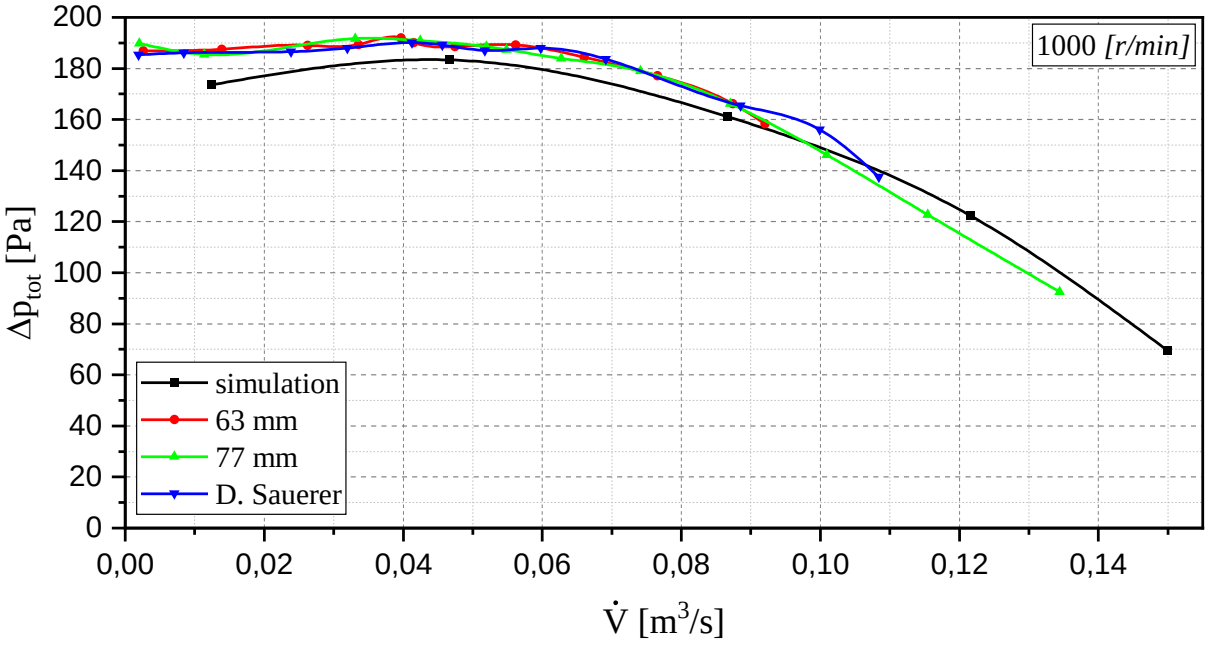

Figure 4-4: Characteristic curves at 1000 r/min

In figure 4-5 the efficiencies at 1000 r/min can be observed analogously. The results are almost congruently aligned with the simulation data until the peak at $0{,}08\ \frac{m^3}{s}$. Afterwards, the measurement from 600 r/min is confirmed, as the graph also declines and the simulation overpredicts the efficiency. A maximum efficiency of 74 % with the 77-mm orifice and 72,8 % with the 63-mm orifice were measured, respectively.

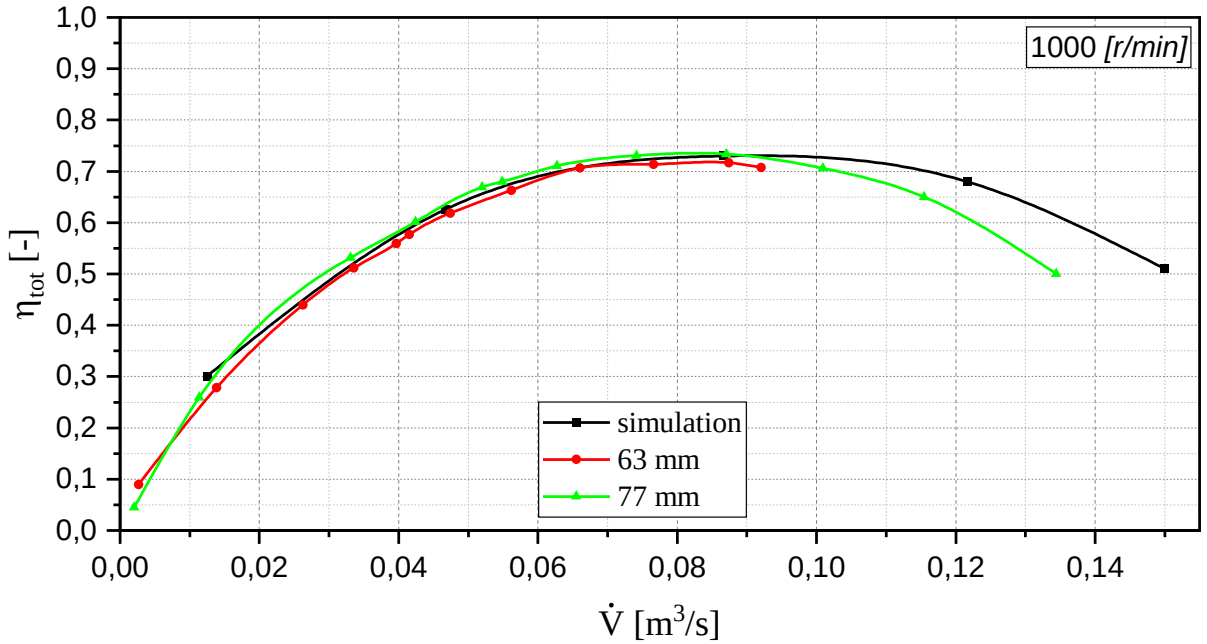

Figure 4-5: Efficiency at 1000 r/min

4.3 Dimensionless review

It is always beneficial to compare the results with other similar turbomachines. In order to do that, in this chapter, the results of both speeds are presented dimensionless. This is done with the help of the similarity laws and dimensionless coefficients [2.1.4]. Figure 4-6 shows the characteristic curves of the results. The flow coefficient represents the x-axis and the pressure coefficient the y-axis. Generally, a very good compliance in the different investigation can be seen, also compared to the ones from *D. Sauerer* (graph: 62 *mm* and 65 *mm*). The existing compliance shows that no significant errors were made in the determination of the characteristic curves.

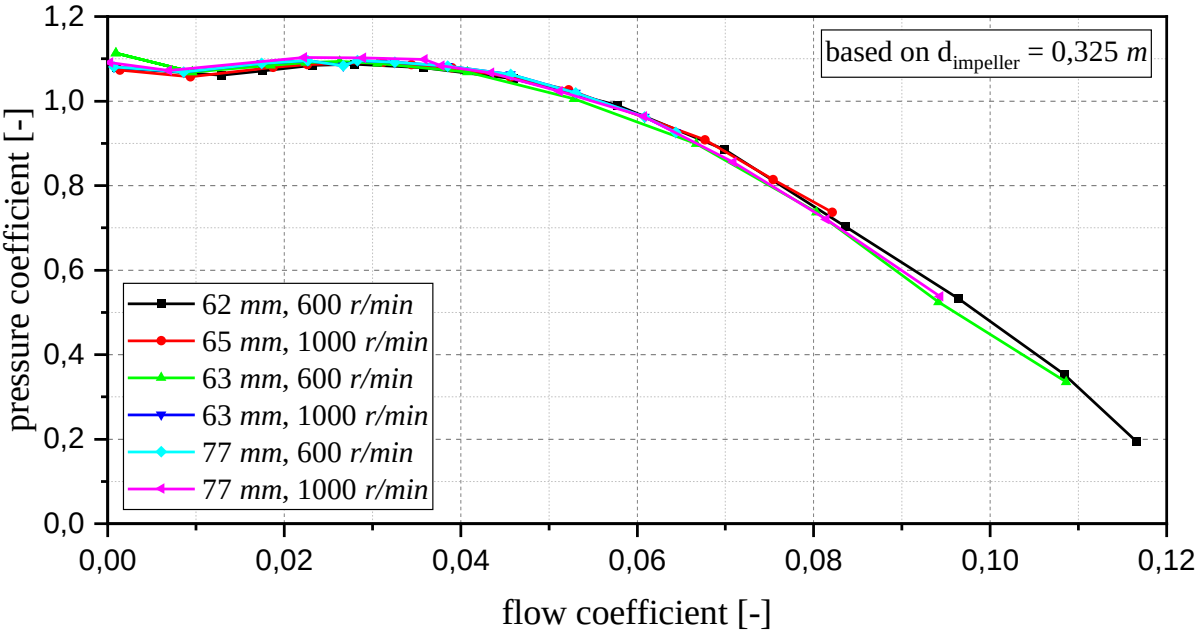

Figure 4-6: Dimensionless characteristic curves

Figure 4-7 displays the measured characteristic curves compared to the simulation. Overall, the graphs show a worse compliance as when compared to the experimental data from *D. Sauerer*, but still a decent alignment can be found. As seen in the previous results, the simulation slightly overpredicts the pressure increase at higher flow rates and underpredicts them at low flow rates.

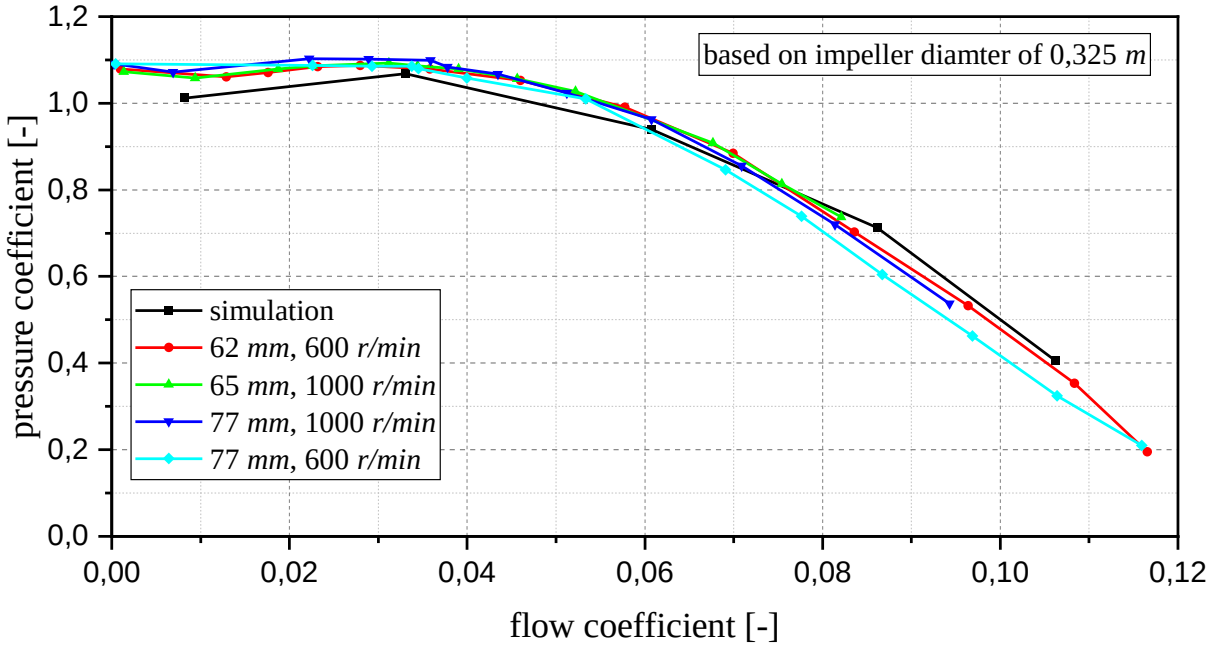

Figure 4-7: Dimensionless characteristic curves

Figure 4-8 shows the efficiencies of all investigations compared to the ones from *D. Sauerer*. It can be observed that they show a good compliance throughout the measured range. The average maximum efficiency is $\eta \approx 73{,}9\ \%$.

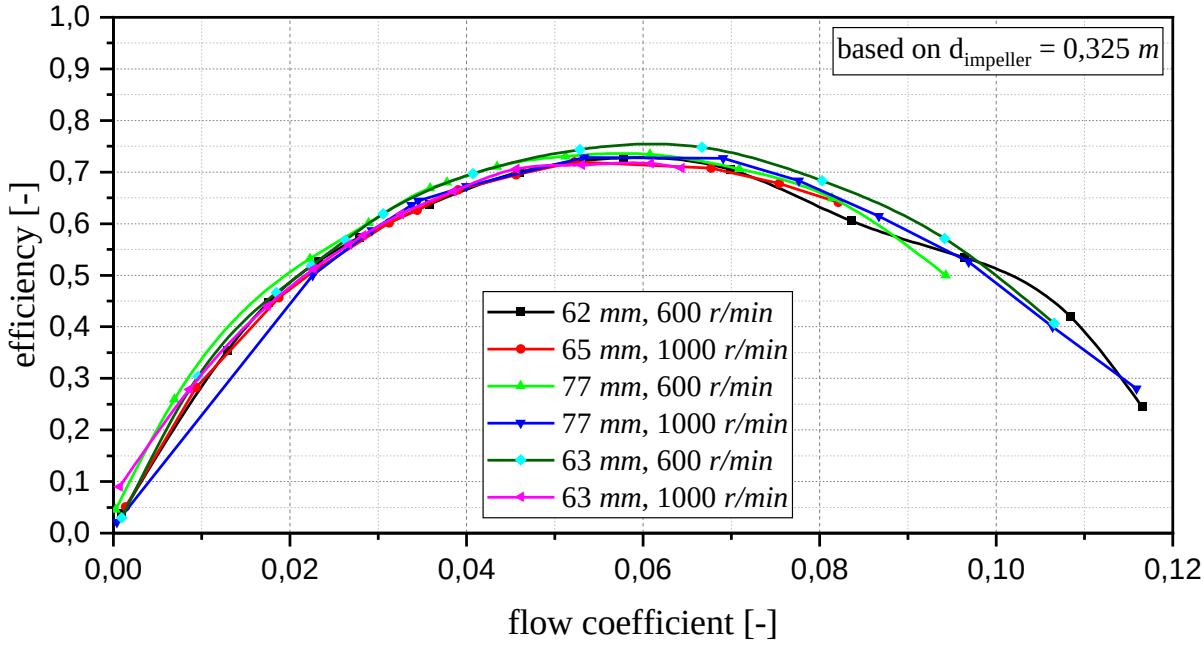

Figure 4-8: Dimensionless efficiencies

Corresponding to the characteristic curve, figure 4-9 shows the efficiencies dimensionless. The deviations between test results are bigger than the deviations within the characteristic curves, as also observed by *D. Sauerer* [11]. It can especially be observed at large flow coefficients. As a possible reason the pressure and volume flow measurement can both be ruled out since the characteristic curve showed a very good compliance. Therefore, an assumption is that the torque measurement causes the divergence.

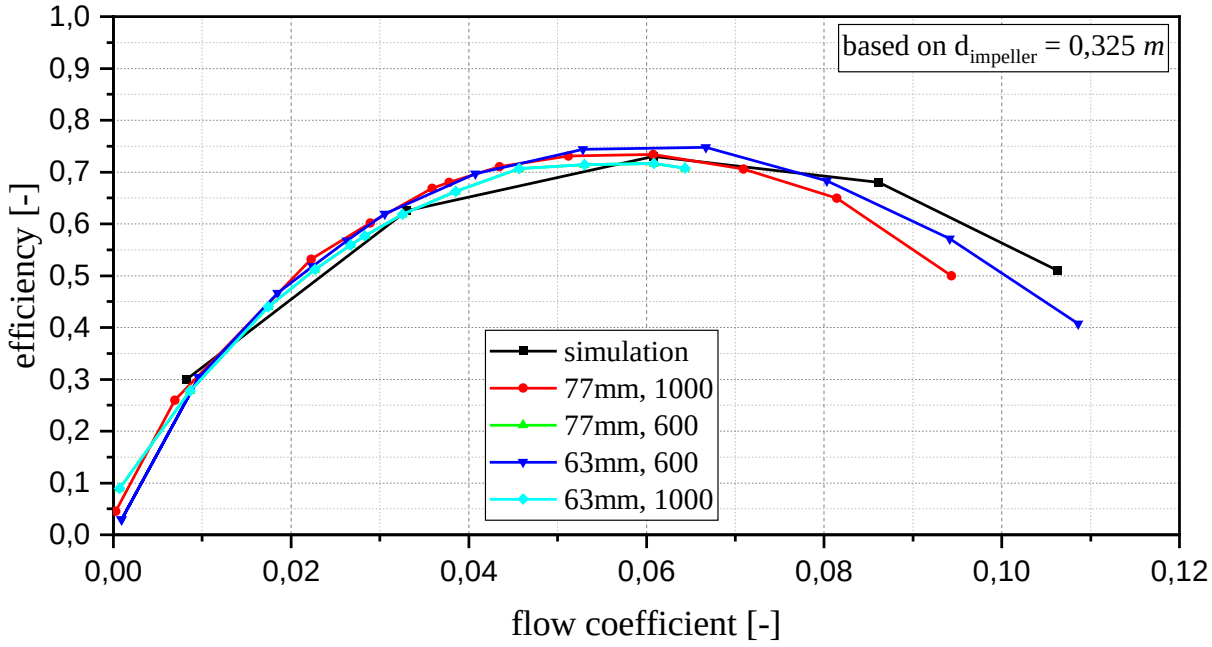

Figure 4-9: Dimensionless efficiencies

.

5 PIV measurement

In this chapter the results of the PIV measurements in the blade channel are presented and compared to the results of *T.Rhode* [23]. The velocity fields are analyzed and information about magnitude and direction gathered. The experiment is done at 600 r/min and 1500 double images are taken and averaged. Also, all images are phase averaged.

5.1 Procedure

Laser and camera need to be aligned to the plane that will be measured. The light section of the laser has to be in the measuring plane. The camera is aligned perpendicular to the plane and focused on a target (A 4) that is divided into 2x2 mm squares. This way the conversation factor M can be found that connects pixels with mm. Afterwards a mask is created to exclude parts of the picture that should not be evaluated by the software. For example, not relevant areas and under- or overexposed parts. Theoretically in both images only the position of the particle changes and the background remains the same. Therefore, a background subtraction is also done to improve the quality of the results. Lastly, the vector field is calculated with the cross-correlation method (chapter 2.3.4).

By the use of a mechanical linear actuator (A 2) the laser and camera can be moved simultaneously along the z-axis while having a constant distance to each other. The advantage is, that once the laser is set up and the camera focused, after changing the position for another measurement, the camera is still focused.

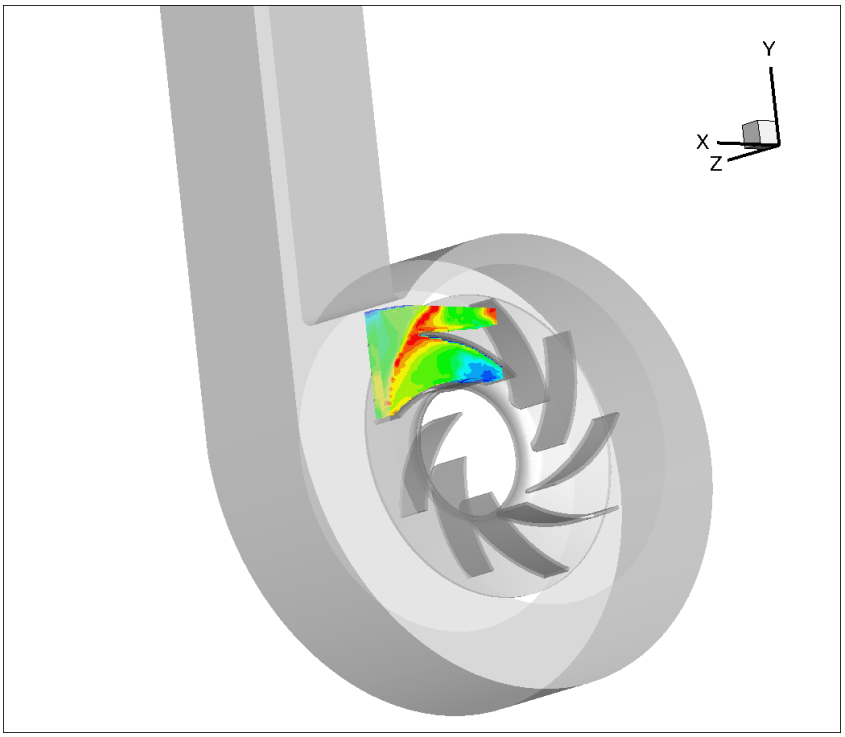

Figure 5-1: Position of the measuring plane 1

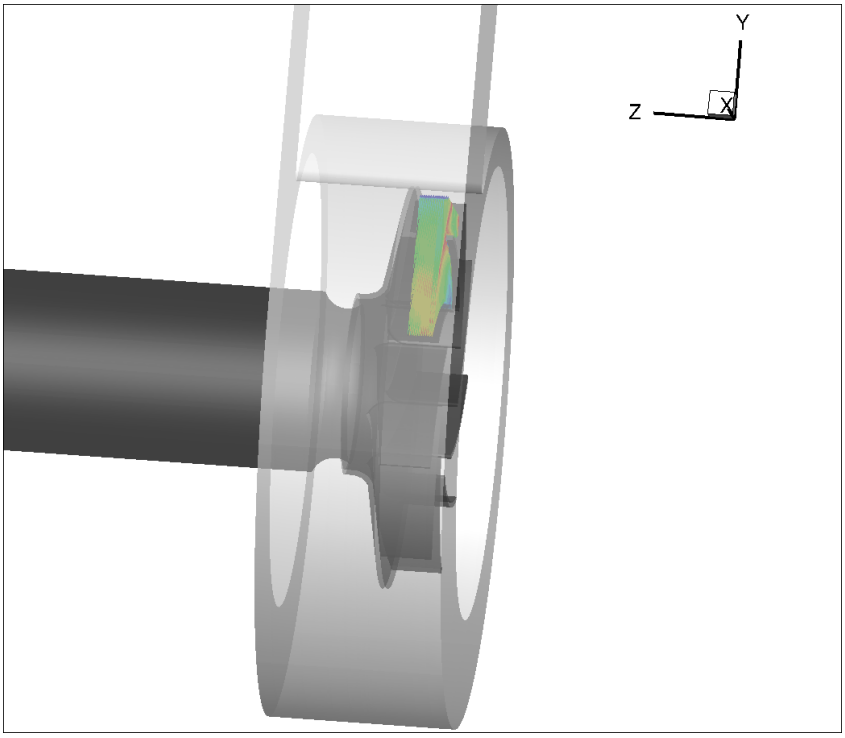

Figure 5-2: Position of the measuring plane 2

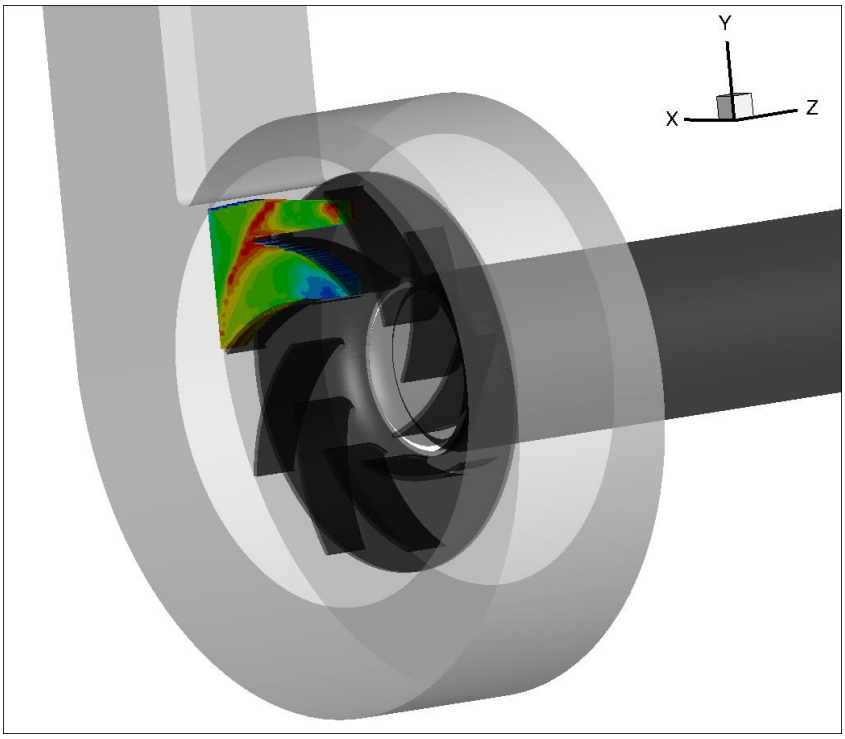

Figure 5-3: Position of the measuring plane 3

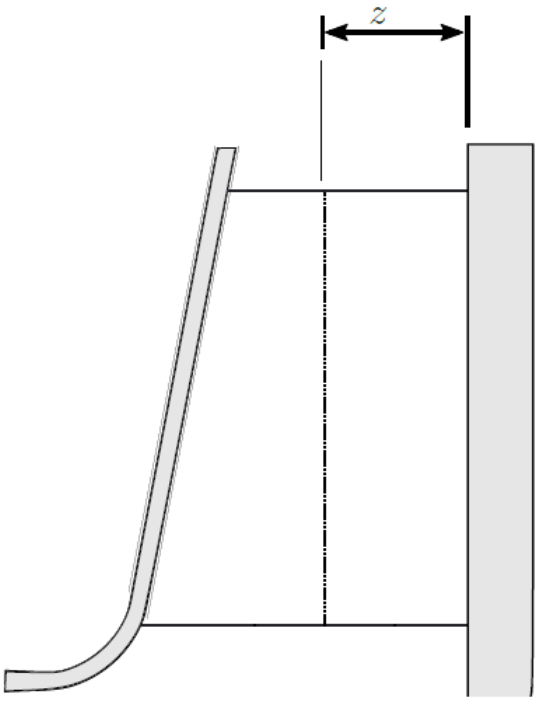

Figure 5-4: View from laser at z-axis

Figure 5-1 till 5-4 show the position of the measuring plane. Along the z-axis 6 planes are measured: 5 *mm*, 12 *mm*, 18 *mm*, 24 *mm*, 30 *mm* and 35 *mm* in relation to the position of the hub. The blade channel's width is 38,2 *mm*, therefore the blade channel is analyzed in almost full depth. Due to reflections of the laser sheet it was not possible to measure closer to hub and shroud. The angle of the impeller's trailing edge relative to the axis is approximately 39° to make a better comparison with the data from *T. Rhode*, which was 40°.

The experiment is done at the point of maximum efficiency (M3), partial load (M2) and full load (M4). Figure 5-5 shows the characteristic curve of the simulation and the operating points chosen for the PIV investigations S1, S2 and S3.

5.2 PIV results

In this chapter the PIV results are presented and discussed. Figure 5-5 shows the operating points M4-M2 on the characteristic curve (blue graph), where the measurement was done and the operating points S2-S4 from the simulation (black graph) as a comparison. The red graph displays the corresponding efficiency to the experimental characteristic curve.

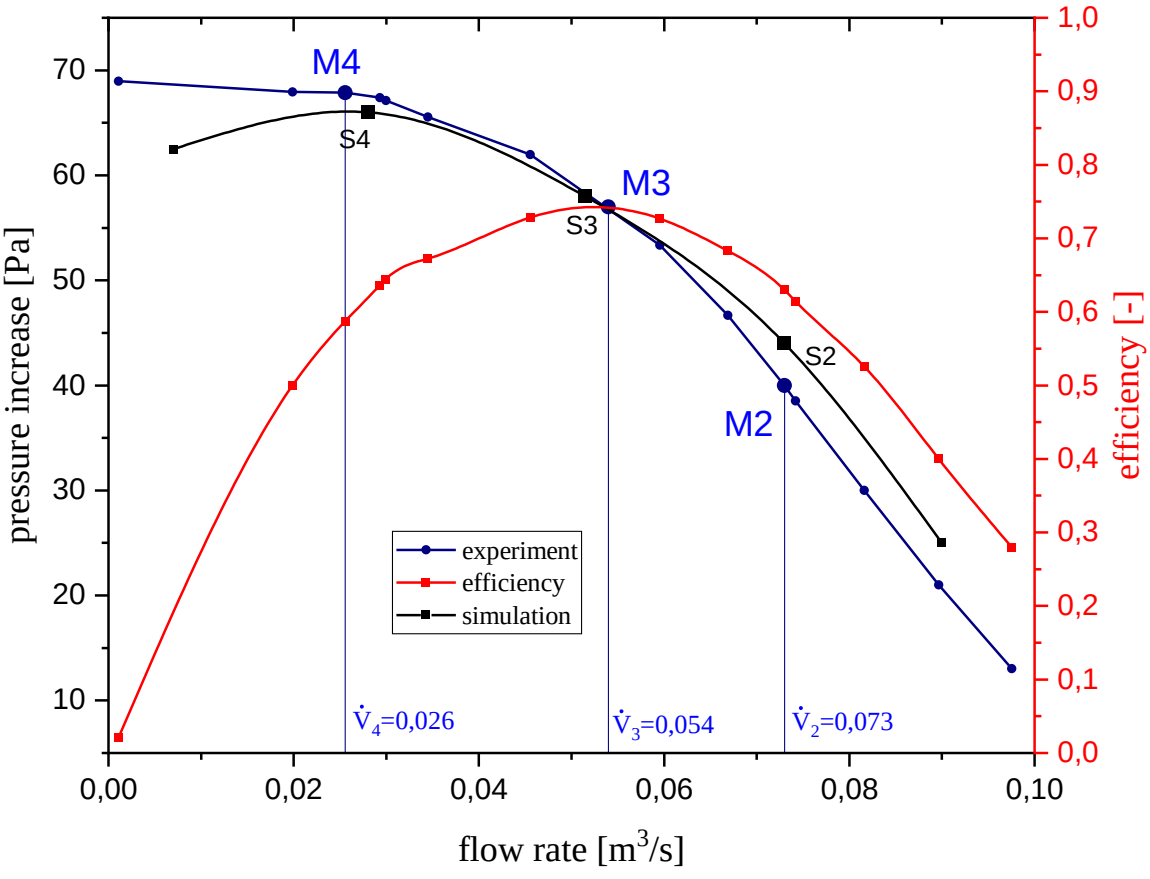

Figure 5-5: comparison of the operating points

The PIV measurement in the blade channel visualizes the flow in a plane of the fan at 600 r/min. The blade's trailing edge angle in the experiment is $\vartheta = 39°$. To ensure better comparability, all speeds are normalized with the reference speed $c_{ref} = \frac{\dot{V}}{A_{ref}}$. The cross-section refers to the impeller's outer diameter. In addition, it is possible to deduce the relative velocity w in the blade channel by calculating the peripheral velocity u. In this chapter the planes 5 mm, 24 mm and 35 mm are presented, because it is assumed that they show the most interesting results. Since measurements close to the hub (5 mm) and shroud (35 mm) do not exist, initially all points are compared at the 24 mm plane. The blade channel's width is 38,2 mm. The results of the other planes can be found attached in the appendix. Additionally, at all three measurements a Relative Standard Deviation (RSD) investigation is done for the absolute velocity c at 6 different positions in the blade channel. The positions P1- P6 can be seen in figure 5-6.

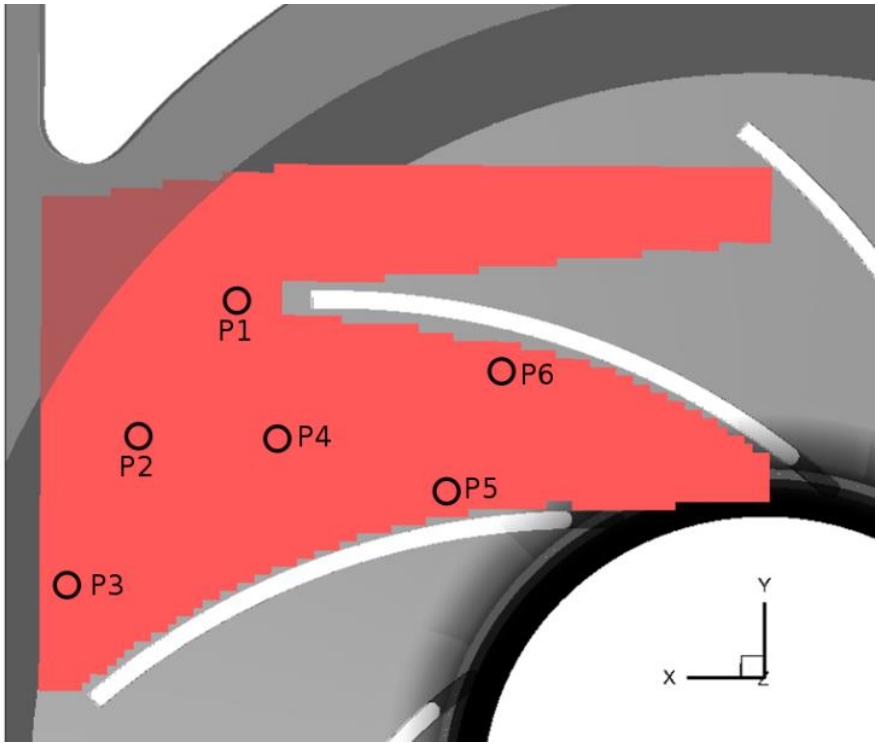

Figure 5-6: Positions of the investigated points

5.2.1 Nominal load M3

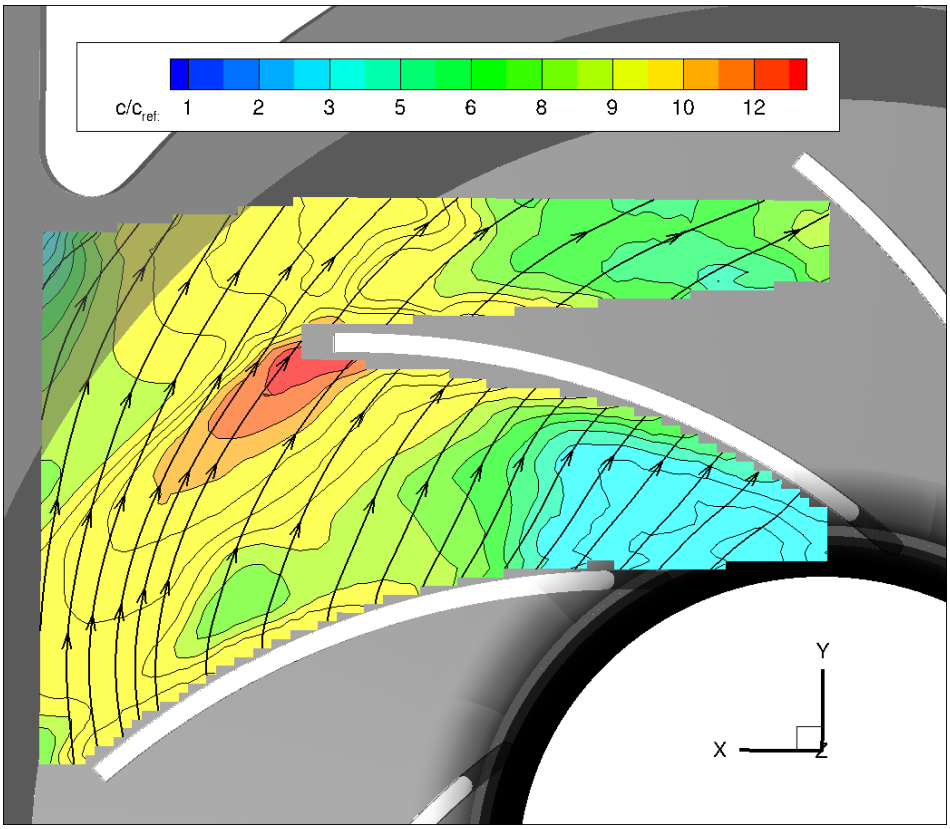

Figure 5-7: PIV measurement M3 in the blade channel at 24 mm; absolute velocity c

In figure 5-7 an extract of the turbomachine with the blade channel is displayed. This plane is chosen because the flow is expected to be unaffected from the edges since it is centrally arranged. The black streamlines emphasize the flow direction. The absolute velocity *c* is normalized with $c_{ref} = 0{,}65\ \frac{m}{s}$.

The greatest velocities can be observed behind the blade's trailing edge. From that point a region with high velocities spreads out in peripheral direction. In general, a steady increase in the velocity can be observed within the blade channel. Near the volute exit the velocity decreases and the influence of the tongue can be noted.

Figure 5-8 shows the corresponding results S3 from the simulation. Both results show a good compliance in the magnitude and direction of velocities.

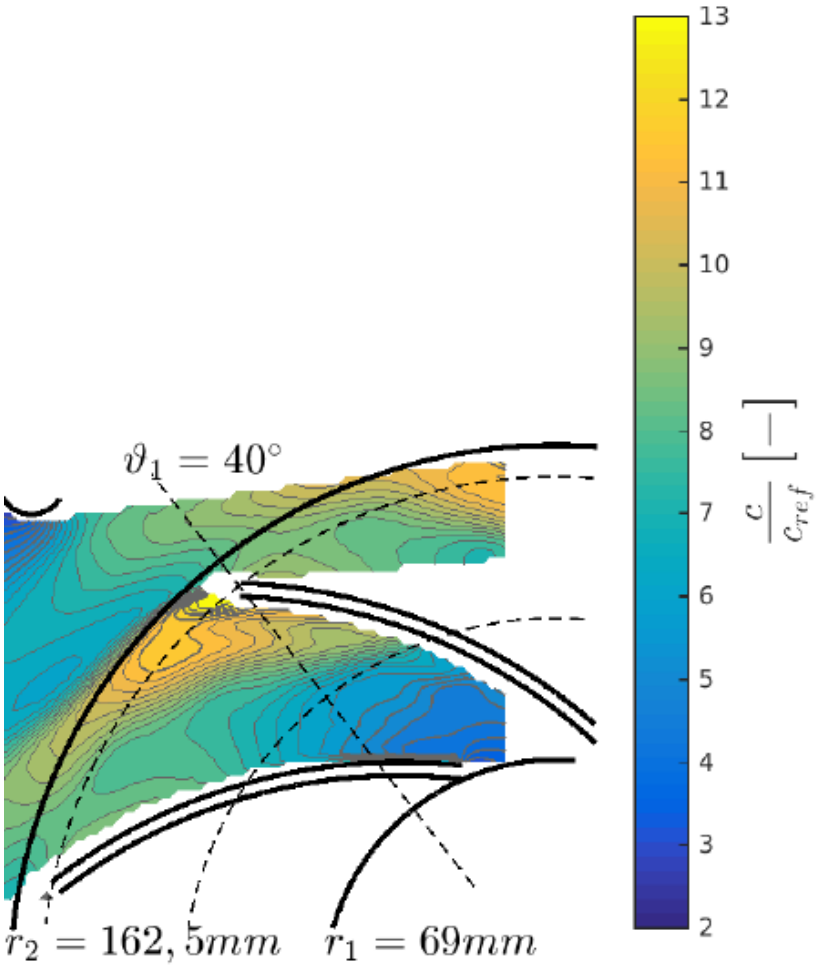

Figure 5-8: PIV measurement S3 in the blade channel at 24 mm; absolute velocity c

Figure 5-9 and Figure 5-10 show the relative velocity *w* in the blade channel. It can be seen that the flow has a homogenous profile and no swirls or detachments can be found, as excepted at this operation point. The black arrows indicate the velocity vectors measured in the experiment. They flow almost parallel to the blades which emphasizes the good design of the impeller.

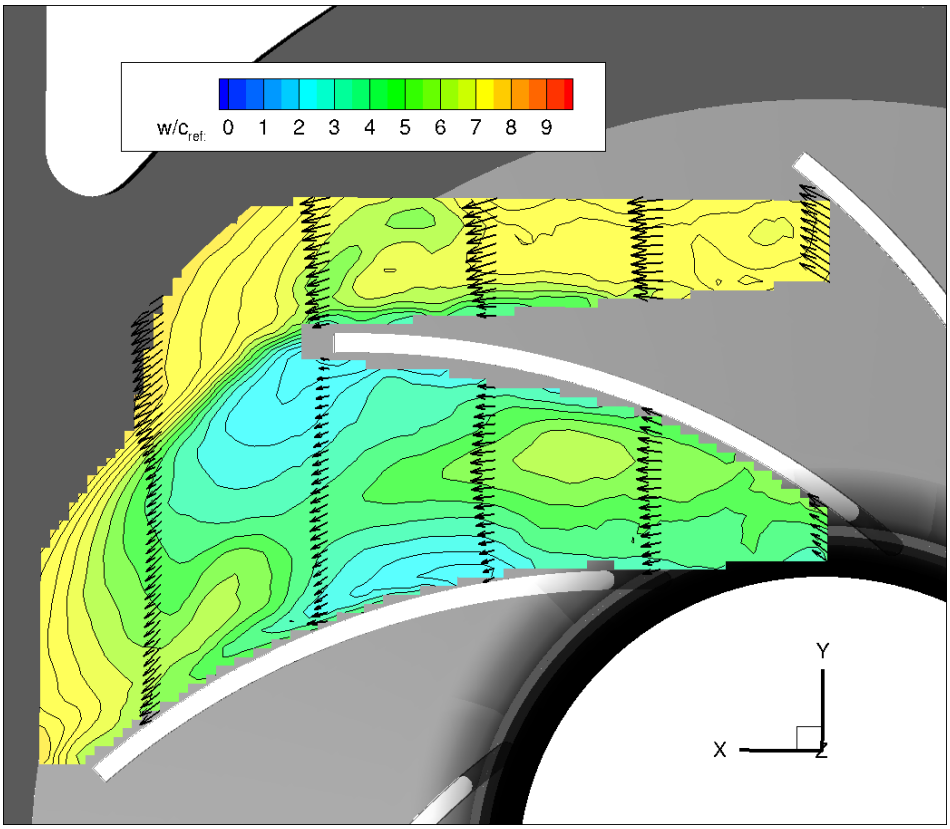

Figure 5-9: PIV measurement M3 in the blade channel at 24 mm; relative velocity w

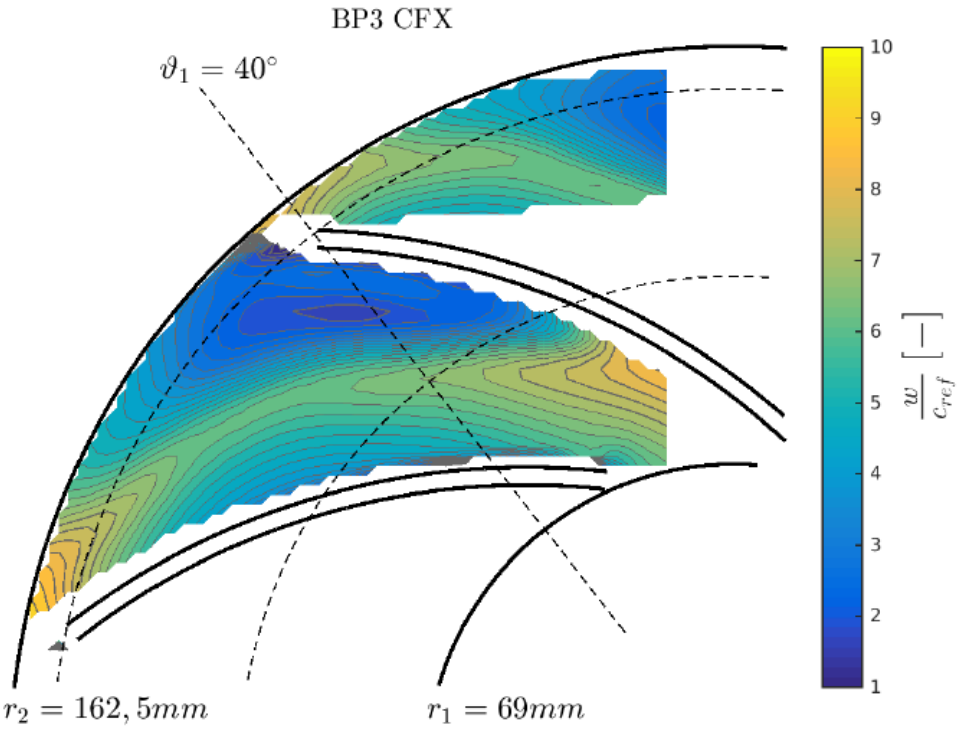

Figure 5-10: PIV measurement S3 in the blade channel at 24 mm; relative velocity w

In addition to previous investigations several planes along the z-axis are measured. There is no data to compare it with. Figure 5-11 shows both absolute and relative velocities at 5

mm, which is the closest measurable plane to the hub without having reflections from the laser sheet. In comparison to the velocity field from the plane in the center of the blade channel, the flow on the left develops small areas with higher velocities near the blades trailing edge. This could be due to the interaction with the boundary layer. Also, the flow profile on the right indicates that the conditions are not as homogenous as in the center. Maximum velocities are also at $c \approx 13 \frac{m}{s}$. Figure 5-12 displays the equivalent flow field near the shroud at 35 mm and it can be observed that the flow conditions are similar in magnitude and direction, but at inlet and suction side there occurs a detachment of the flow.

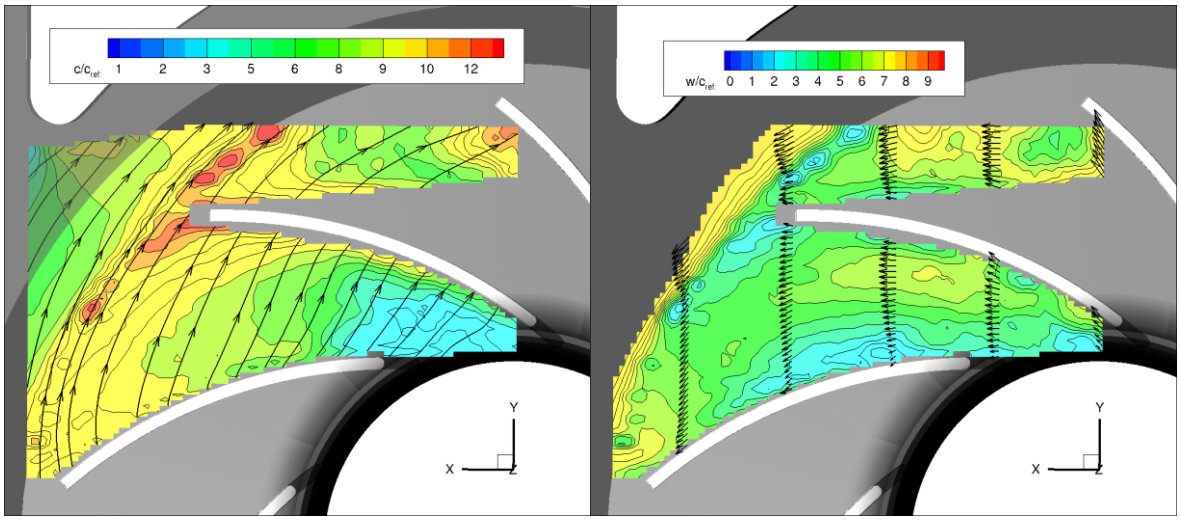

Figure 5-11: PIV measurements M3 at -5 mm; absolute velocity c (top) and relative velocity w (down)

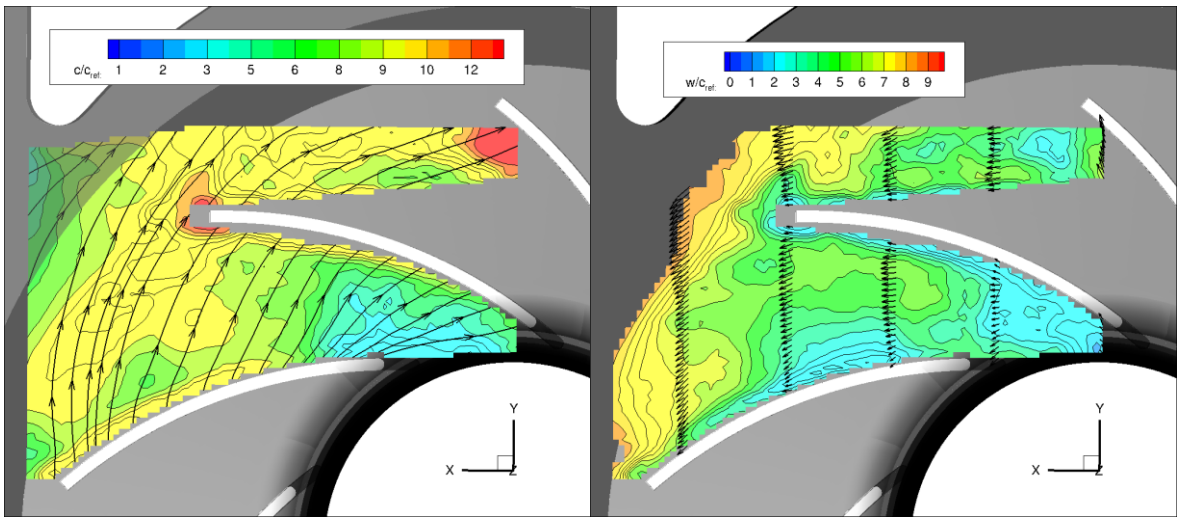

Figure 5-12: PIV measurements at -35 mm; absolute velocity c (top) and relative velocity w (down)

Relative Standard Deviation (RSD) at operating point M3

Figure 5-13 shows the *RSD* of the absolute velocity c along the number of measurements for 6 different positions (P1-P6) in the blade channel. The positions can be seen in figure 5-6. If the graph is converging, the measurements repeatability is proven and the series of test are statistically significant. It can be observed that all graphs show a converging behavior. P2 and P4 show the lowest RSD value and a smooth converging behavior. This could be due to the fat, that they are located in the middle of the blade channel with fairly constant velocities. On the other hand, P5 and P6, which are located closer to the edges and velocity fluctuations are more present, have a higher RSD value. The value of P3 is also in the same magnitude, but additionally shows a strange jump at $n \approx 320$. The cause could be that this area was slightly underexposed in the PIV experiment.

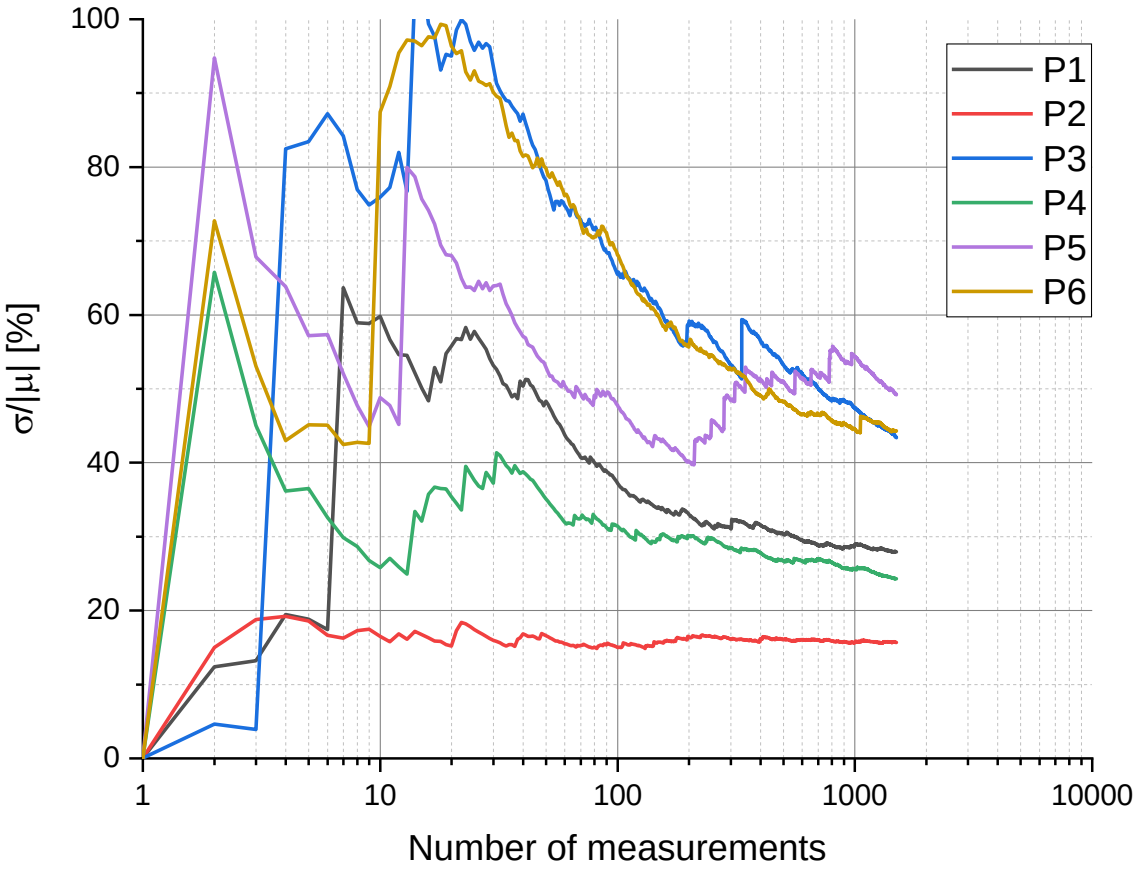

Figure 5-13: RSD at M3

5.2.2 Partial load M4

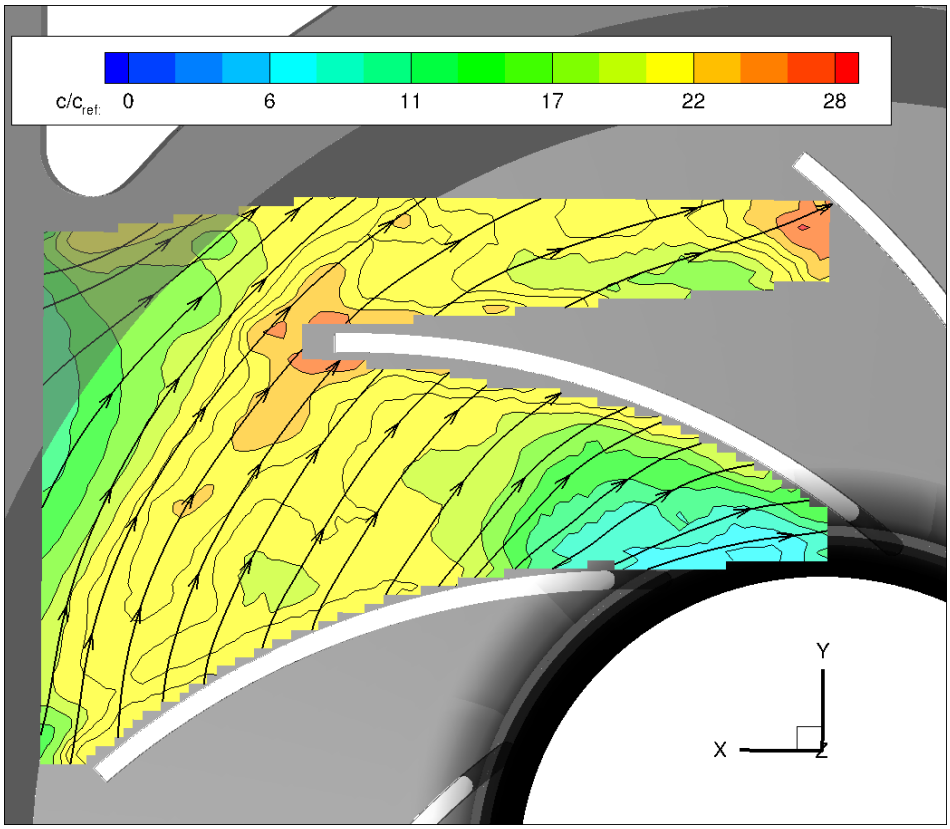

Figure 5-14: PIV measurement M4 at 24 mm; absolute velocity c

Figure 5-14 shows the normalized absolute velocity at M4 (partial load), which is at low flow rates and a higher pressure increase. The absolute velocity c is normalized with $c_{ref} = 0{,}313\ \frac{m}{s}$. The normalized velocity distribution and gradients are much higher than at M3. Again, near both blade's trailing edge the highest velocities occur, which shows the periodicity. The velocity near the volute is in comparison to M3 more influenced and very small. The simulation result at S4 can be seen in figure 5-15. It predicts slightly smaller velocities, especially near the tongue, but generally the distribution shows again a good compliance.

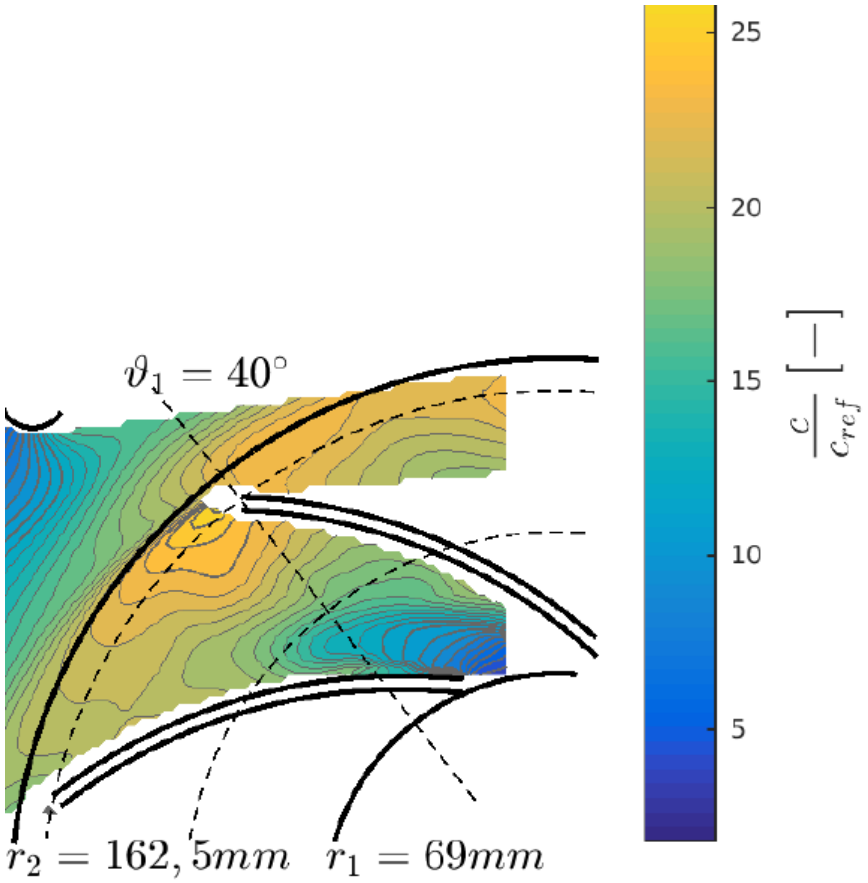

Figure 5-15: PIV measurement S4 at 24 mm; absolute velocity c

The following figure 5-16 and figure 5-17 show the corresponding normalized relative velocities. It can be observed that on the suction side near the blade small flow detachments take place due to bad inflow conditions at this operating point. The main flow is again flowing in the center of the blade channel not until the outer region of the blade channel. On the other hand, in the transition to the volute housing greatly increased relative velocities can be seen, since there is almost no flow outside of the impeller that rotates and accelerates the fluid within it. Overall, the simulation predicts smaller velocity fields and the detachment is not as distinct as in the experiment.

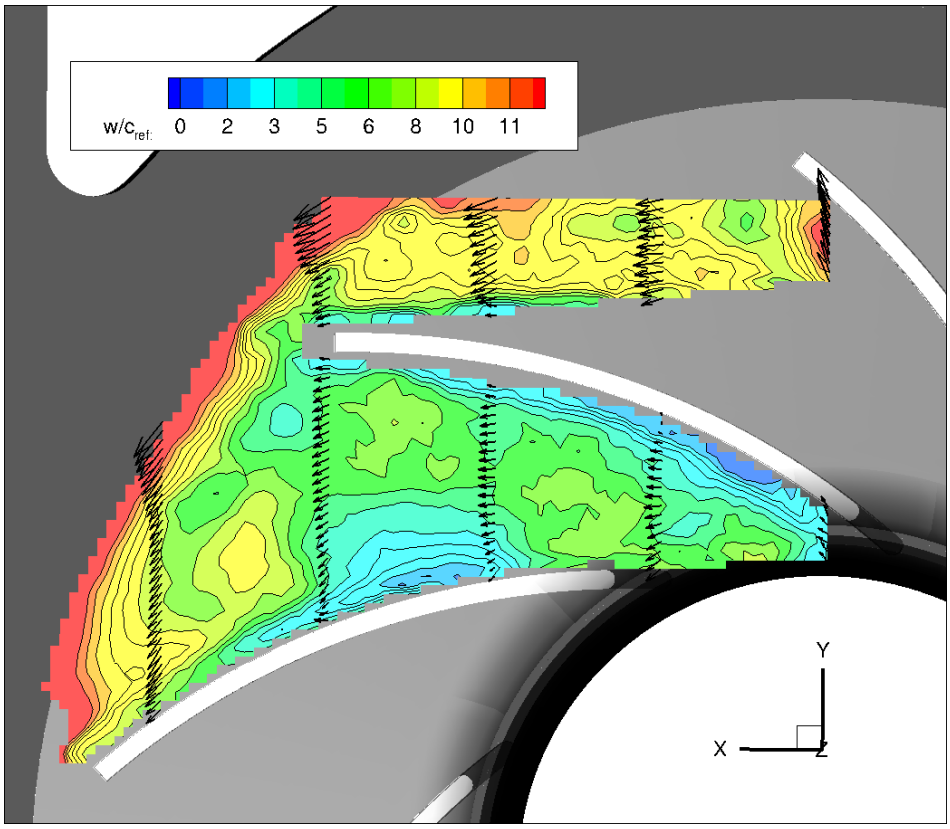

Figure 5-16: PIV measurement M4 at 24 mm; relative velocity w

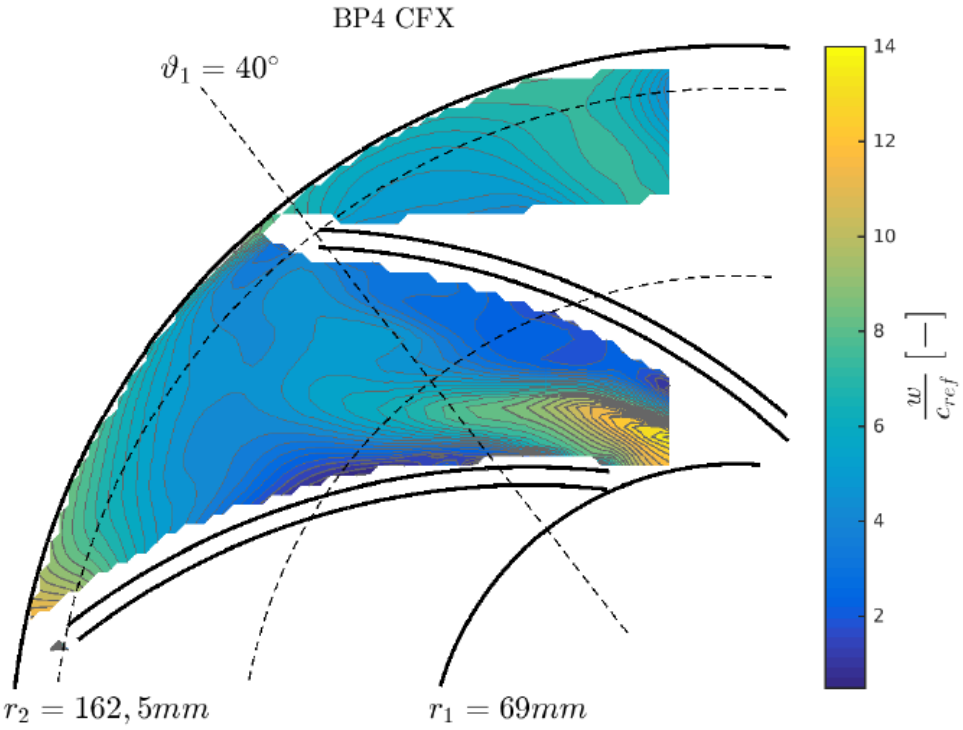

Figure 5-17: PIV measurement S4 at 24 mm; relative velocity w

Figure 5-18 and figure 5-19 display the same effects as in the center of the blade channel and the maximum velocities are even higher up until $c \approx 30 \frac{m}{s}$. Furthermore, the detachment and flow separation near the suction mouth can be observed even better, due to bad inflow conditions at partial load. The influence of the tongue is also more distinct at this measuring plane.

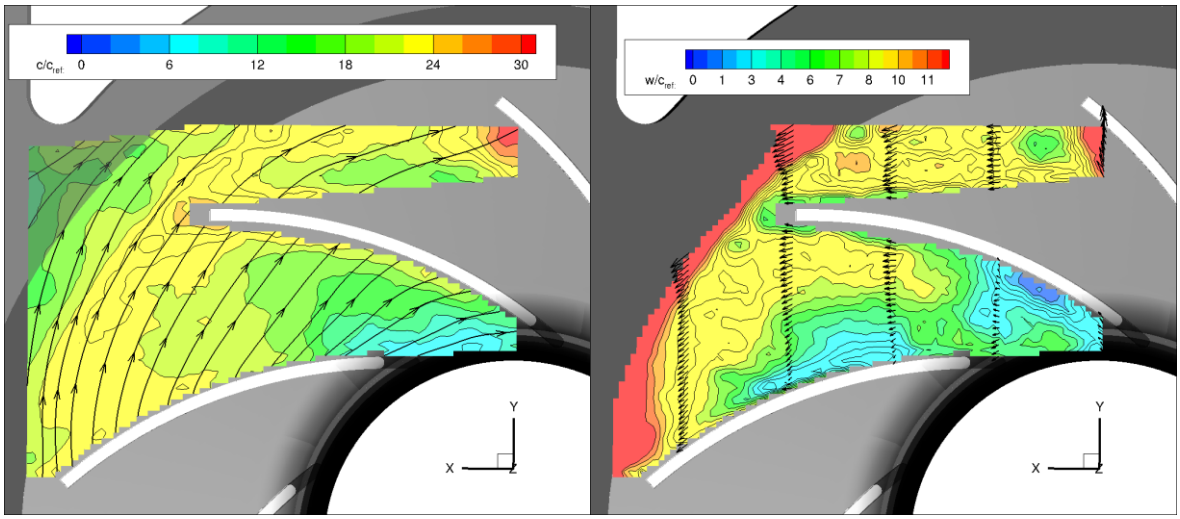

Figure 5-18: PIV measurement at 5 mm, absolute velocity c (top) and relative velocity w (down)

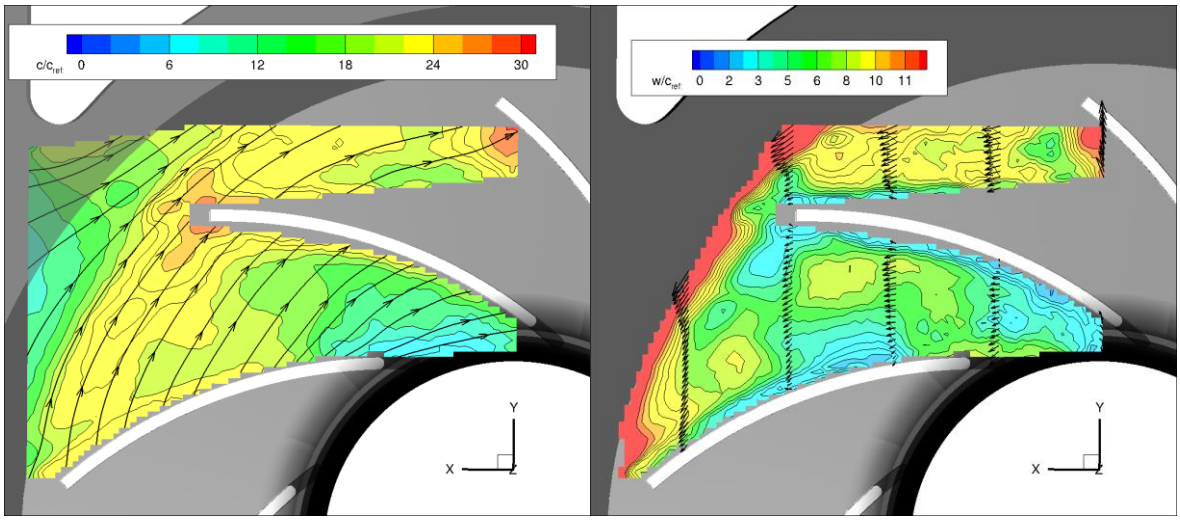

Figure 5-19: PIV measurement at 35 mm, absolute velocity w (top) and relative velocity w (down)

Relative Standard Deviation (RSD) at operating point M4

Figure 5-20 shows the *RSD* of the absolute velocity c at M4. In general, all graphs are converging like previously at M3. P1, P2 and P4 also show the lowest RSD value and the outer points are higher. Due to the underexposed area, P3 shows a jump at $n \approx 210$ but is afterwards converging. To view the location of the positions P1-P6, refer to figure 5-6.

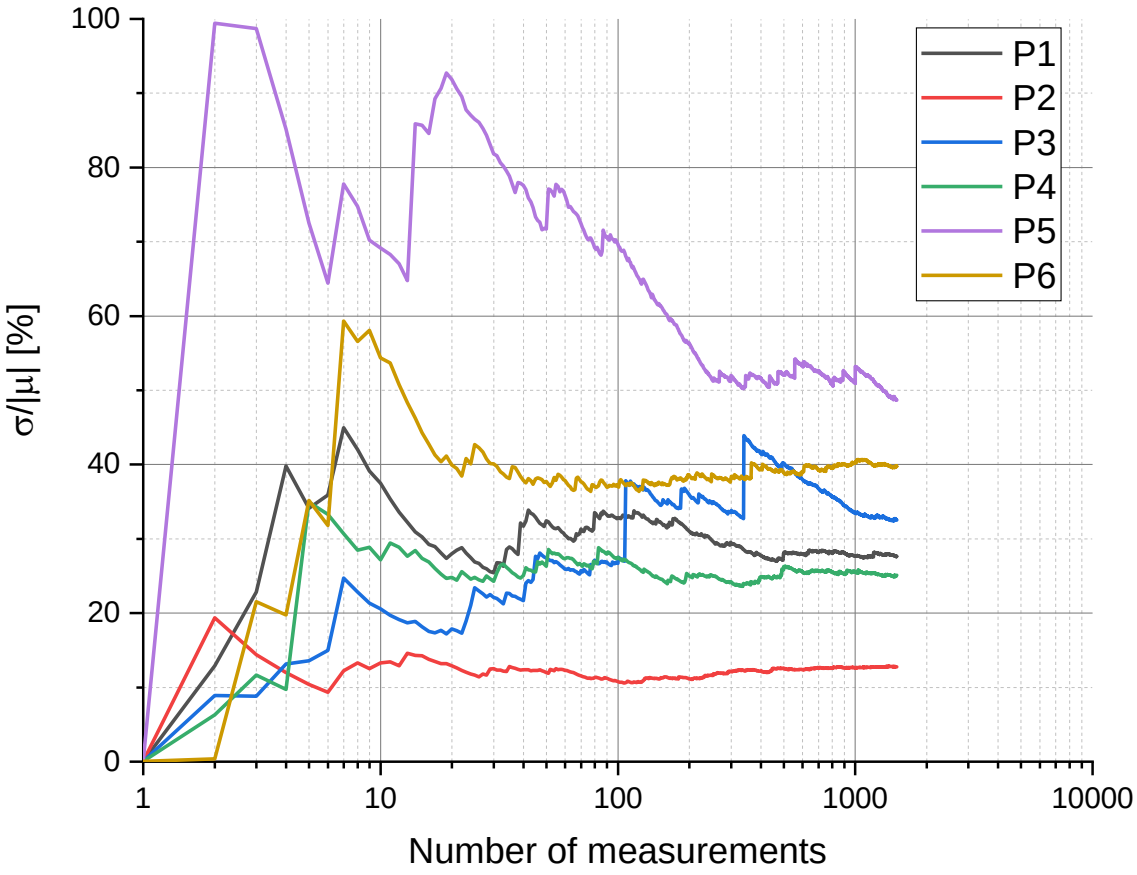

Figure 5-20: RSD at M4

5.2.3 Full load M2

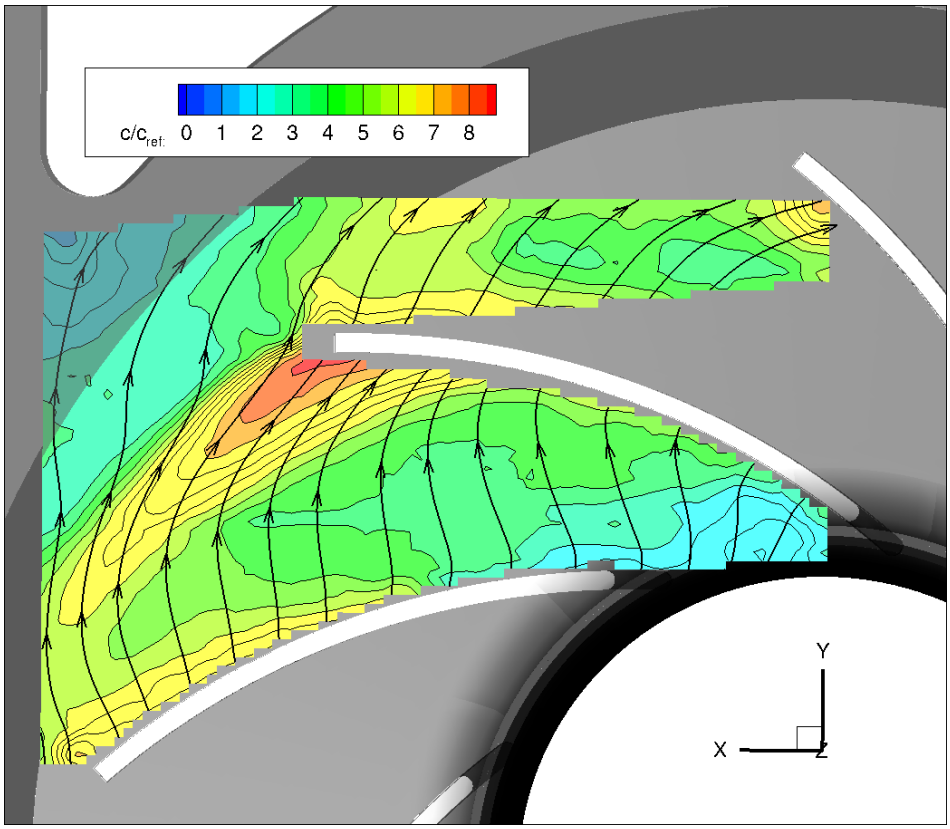

Figure 5-21: PIV measurement M2 at 24 mm; absolute velocity c

Figure 5-21: PIV measurement M2 at 24 mm; absolute velocity c shows the normalized absolute velocity at M3 (full load), which is at high flow rates and a low pressure increase occurs. The absolute velocity c is normalized with $c_{ref} = 0{,}88\ \frac{m}{s}$. The area of higher velocities near the blade's trailing edge is clearly visible and it keeps increasing in peripheral directing. The change of direction of the streamlines is due to the incorrectly and changed inflow conditions of the blades. Close to the volute outlet the flow is very slow which can also be observed in the simulation S4 in figure 5-22. In general, the simulation shows a good compliance at this measuring point.

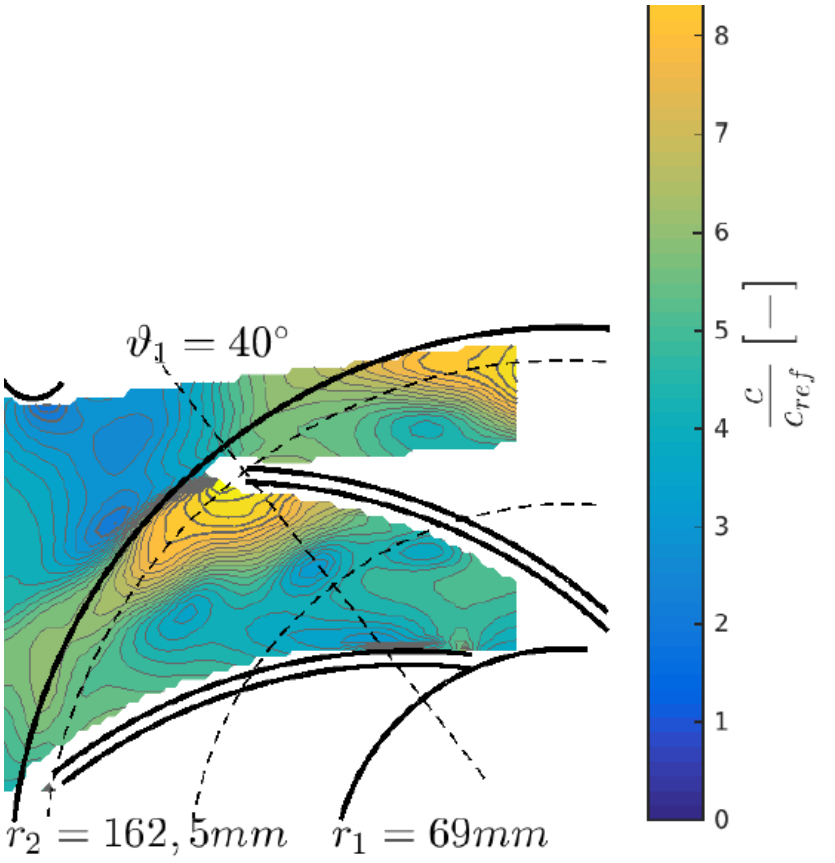

Figure 5-22: PIV measurement M2 at 24 mm; absolute velocity c

The corresponding relative velocity *w* of the experiment and simulation is displayed in figure 5-23 and Figure 5-24. A region of higher velocities can be seen at the suction side of the blade and in contrast, smaller velocities can be observed at the pressure side with small separations of the flow. The simulation predicts similar flow conditions but overall higher velocities.

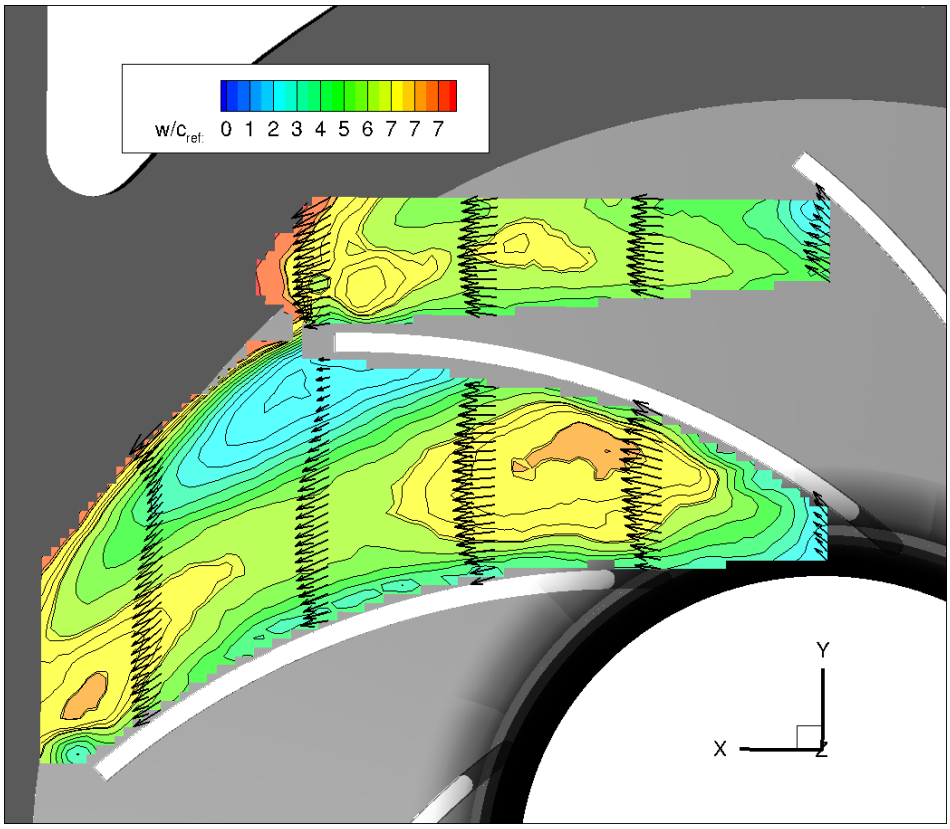

Figure 5-23: PIV measurement M2 at 24 mm; relative velocity w

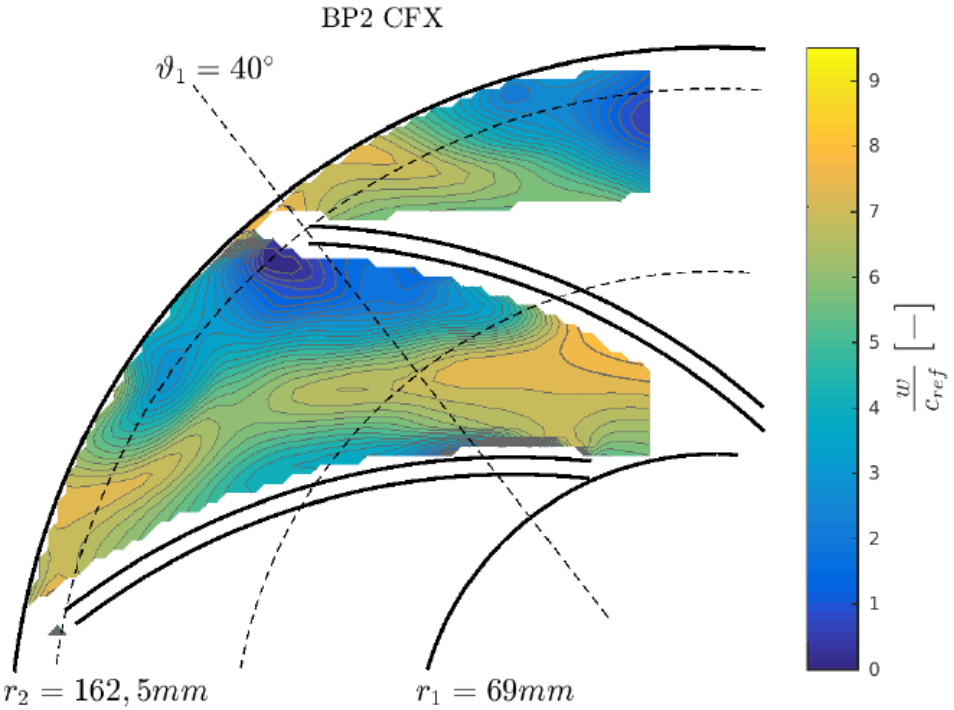

Figure 5-24: PIV measurement M2 at 24 mm; relative velocity w

Lastly, the two extreme positions close to the hub and shroud are displayed in figure 5-25 and Figure 5-26. Both flow profiles show a high inhomogeneity, detachment and flow separations.

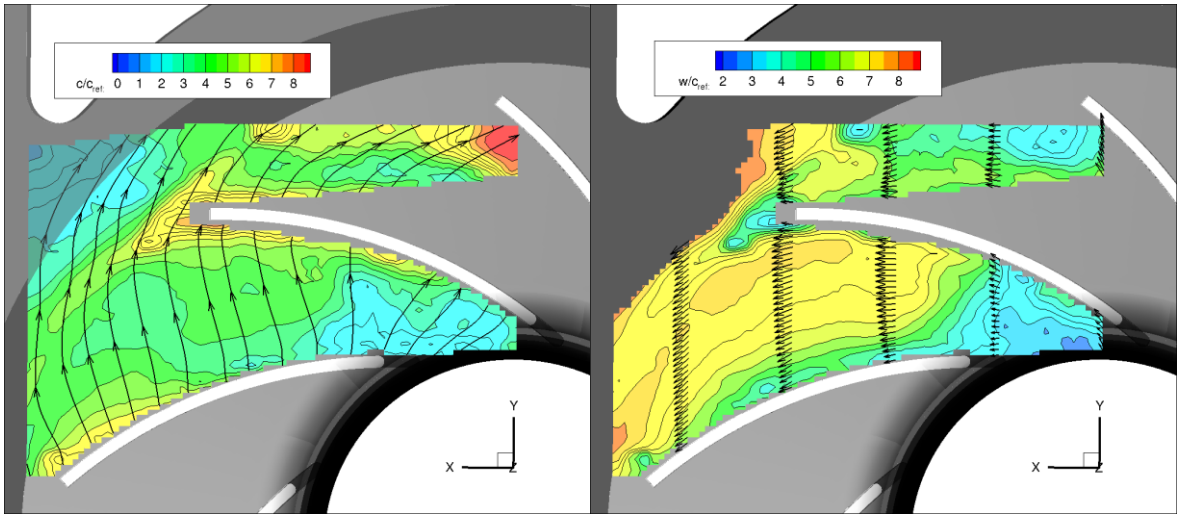

Figure 5-25: PIV measurement M2 at 5 mm; absolute velocity c (top) and relative velocity w (down)

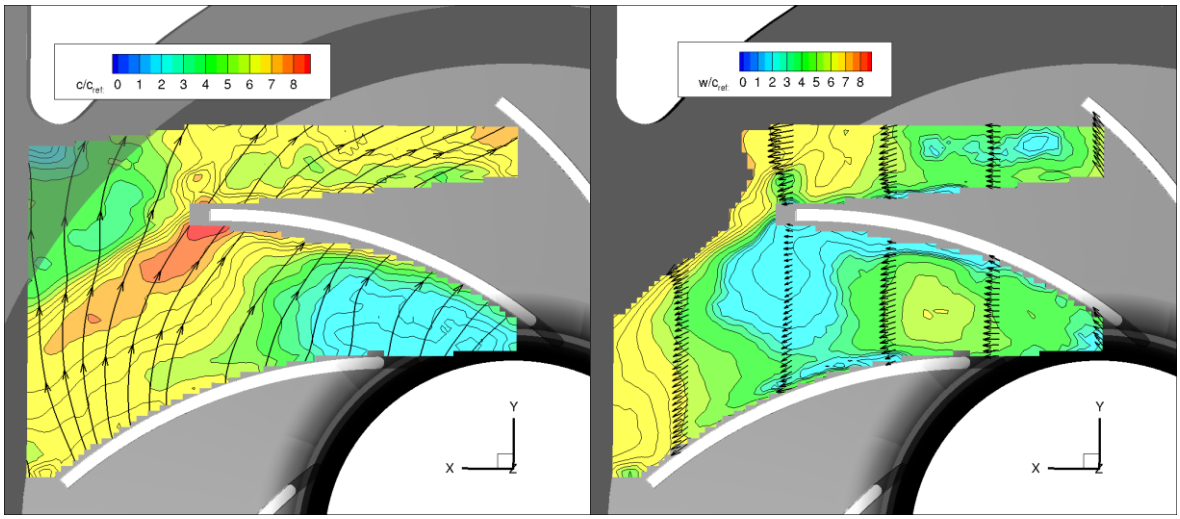

Figure 5-26: PIV measurement M2 at 24 mm; absolute velocity c (top) and relative velocity w (down)

Relative Standard Deviation (RSD) at operating point M4

Lastly, figure 5-27 displays the RSD of the absolute velocity *c* at operation point M4. Apposite to the previous RSD evaluations, the graphs are converging. Center positions P2 and P4 show a lower RSD value as the rest. The jump observed previously at P3 is also shown here.

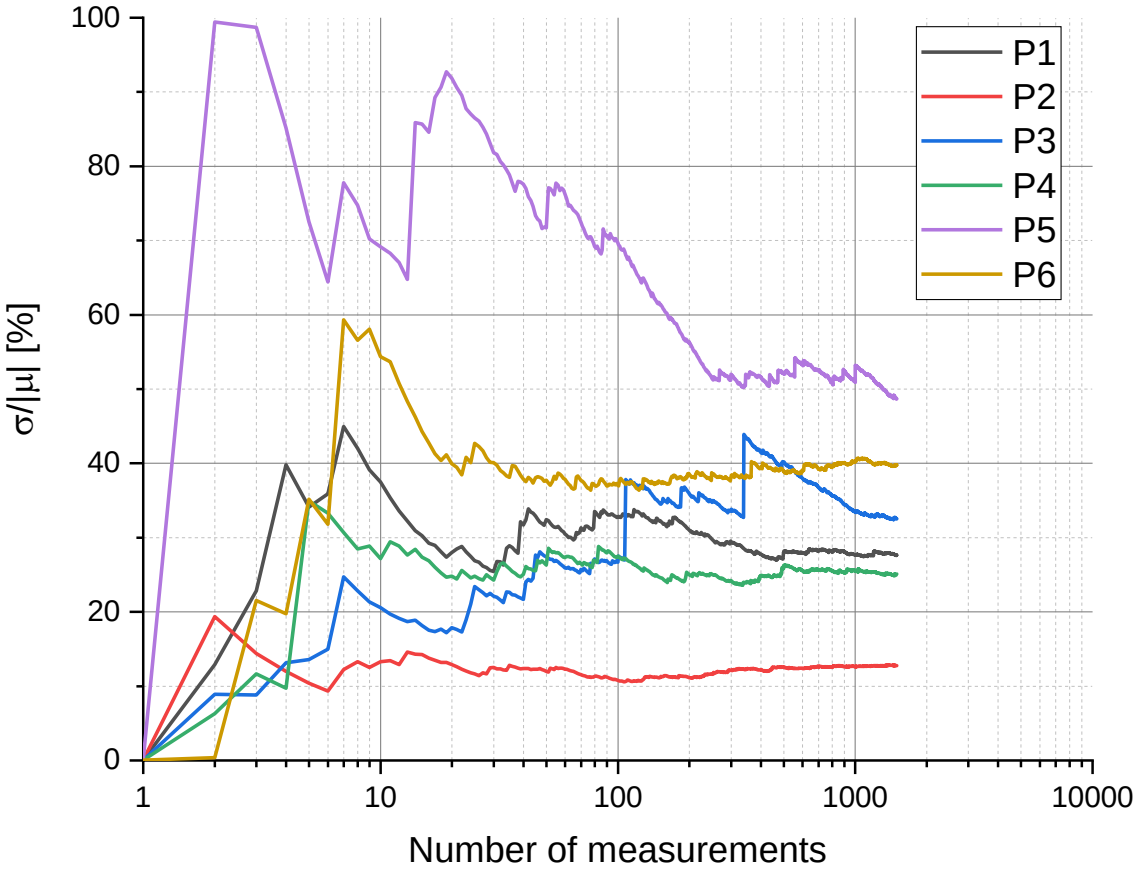

Figure 5-27: RSD at M4

6 Conclusion

Within the framework of this thesis extensive PIV measurements within the impeller of a centrifugal fan were done. Anteriorly, the fan's characteristic curve and efficiency was determined and compared to previous investigations.

In the beginning of this work, the test bench was slightly modified to achieve a higher quality and accuracy in the results of the determination of the efficiency. Previously, problems with the powertrain and fluctuation with the friction torque had occurred, and even though they have been almost entirely eradicated, small changes were made with success. After the modification the fan's characteristic curve at different speeds was determined to proof scalability and the efficiencies were calculated. Results were compared to the previous experimental data and also to existing simulation data. All data show in general a good compliance and the reliability and reproducibility were proven.

After that, the flow conditions in the blade channel of the impeller was investigated using PIV. Therefore, a set-up for laser and camera was constructed to simplify the measurements and also to increase the quality of the images. The blade channel was previously investigated in one single plane at three different operation points: partial load, nominal load and full load. In this work those points, measured previously on the characteristic curve, were also measured, analyzed and compared to the other data. All measurements were done at the same rotational speed. However, multiple planes were measured in the blade channel, which, with the new set-up, was possible.

7 Outlook

This chapter will give some suggestions for improvements for this test bench and further investigations.

Regarding the calculation of the efficiency, despite all the efforts to reduce the torque fluctuations, there is still room for improvement. One possible source is the motor and a flywheel could be a possibility to reduce the fluctuations. In this work the shafts were aligned extensively by means of trial and error, but a professional company may find a better alignment.

During the PIV measurements it came to the attention that the housing cover was slightly bend due to a connector that is to short (see A 7). This causes problems with the alignment of laser and camera as the housing cover is not perpendicular to the laser sheet. It should be taken into consideration to manufacture new ones.

It is now possible to measure multiple planes with a high level of accuracy in comparatively short time. The turbomachine can be rotated in a way that in future investigations other blade channels, that are not affected by the tongue, can be measured extensively. This way an even better knowledge of the flow phenomena and conditions can be gathered.

Bibliography

[1] S.-C. e. a. Lin, "An integrated experimental and numerical study of forward–curved centrifugal fan," *Elsevier, ScienceDirect,* pp. 1-3, 2001.

[2] S.-C. e. a. Lin, "An integrated performance analysis for a backward-inclined centrifugal fan," *Elsevier, ScienceDirect,* pp. 1-5, 2011.

[3] S. H. e. a. Liu, "Computational and experimental investigations of performance curve of an axial flow fan using downstream flow resistance method," *Elsevier, ScienceDirect,* 2010.

[4] C. e. a. Sarraf, "Experimental study of blade thickness effects on the overall and local performances of a Controlled Vortex Designed axial-flow fan," *Elsevier, ScienceDirect,* pp. 1-4, 2011.

[5] J. e. a. Zhang, "Numerical and experimental investigations of the unsteady aerodynamics and aero-acoustics characteristics of a backward curved blade centrifugal fan," *Elsevier, ScienceDirect,* pp. 1-12, 2016.

[6] M. e. a. Gholamian, "Effect of axial gap between inlet nozzle and impeller on efficiency and flow pattern in centrifugal fans, numerical and experimental analysis," *Elsevier, ScienceDirect,* pp. 1-2, 2013.

[7] P. e. a. Hergt, "Visuelle Untersuchung der Strömung im Leitrad einer Radialpumpe," *Schweizerische Bauzeitung,* pp. 1-8, 2016.

[8] L. e. a. Chunxi, "The performance of a centrifugal fan with enlarged impeller," *Elsevier, ScienceDirect,* pp. 1-2, 2011.

[9] B. Driedger, Experimentelle Untersuchung eines generischen Radialventilator-Modells, Masterarbeit, Karlsruher Institut für Technologie: Fachgebiet für Strömungsmaschinen, 2015.

[10] M. Raffel, Particle Image Velocimetry, Springer, 2.Auflage, 2007.

[11] D. Sauerer, Konstruktive Überarbeitung eines Prüfstandes für einen radialen Ventilator, Masterarbeit, Karlsruher Institut für Technologie: Fachgebiet für Strömungsmaschinen, 2017.

[12] D. D. I. f. N. e.V., DIN EN ISO 5167 Durchflussmessung von Fluiden mit Drosselgeräten in voll durchströmten Leitungen mit Kreisquerschnitt, 2004.

[13] K. Menny, Strömungsmaschinen - Hydraulische und thermische Kraft- und Arbeitsmaschinen, Teubner, 5. Auflage, 2006.

[14] J. Kriegseis, "Experimentelle Strömungsmechanik," Vorlesungsunterlagen, 2017.

[15] T. Carolus, Ventilatoren, Springer, 3. Auflage, 2013.

[16] E. Kommission, "Verordnung (EU) Nr. 327/2011," Europäische Union, 2011.

[17] E. Kommission, "Richtlinie 2009/125/EG," Europäische Union, 2009.

[18] J. Zierep and K. Bühler, Grundzüge der Strömungslehre, Springer, 2015.

[19] "Schaeffler," 17 Februar 2018. [Online]. Available: http://medias.schaeffler.de/medias/de!hp.tg.cat/tg_hr*ST4_102160011. [Accessed 17 02 2018].

[20] S. M. Ross, Statistik für Ingenieure und Naturwissenschaftler, Heidelberg: Elsevier GmbH, Spektrum Akademischer Verlag, 3. Auflage, 2006.

[21] "How to Statistics," [Online]. Available: http://www.statisticshowto.com/relative-standard-deviation/. [Accessed 17 Februar 2018].

[22] Contrinex, Data Sheet Photoelectric Proximity Switch.

[23] T. Rhode, Numerische Untersuchung eines generischen Radialventilator-Modells mit kommerzieller und freier Software, Masterarbeit, Karlsruher Institut für Technologie: Fachinstitut für Strömungsmaschinen, 2016.

[25] R. W. Johnson, The Handbook of Fluid Dynamics, Springer, 1998.

[26] J. Gülich, Centrifugal Pumps, Springer, 2014.

[27] B. Zohuri, Dimensional Analysis and Self-Similarity Methods for Engineers and Scientists, Springer, 2015.

[28] N. Pedersen, Flow in a Centrifugal Pump Impeller at Design and Off-Design Conditions—Part I, Tecnical University of Denmark, 2008.

[29] K. e. a. Cheah, Numerical Flow Simulation in a Centrifugal Pump at Design and Off-Design Conditions, National University of Singapore, 2007.

[30] D. S., Numerische und experimentelle Untersuchungen an Querstromventilatoren, Dissertation, KIT, 2002.

[31] Untersuchungen der instationären Strömungsvorgänge in Seitenkanalverdichtern mit Hilfe der Particle-Image-Velocimetry, Dissertation, Technische Universität Berlin, 2003.

[32] W. e. a. G., PIV Measurements in the Impeller and the Vaneless Diffuser of a Radial Flow Pump in Design and Off-Design Operating Conditions, ASME: Journal of Fluids Engineering, 2002.

Appendix

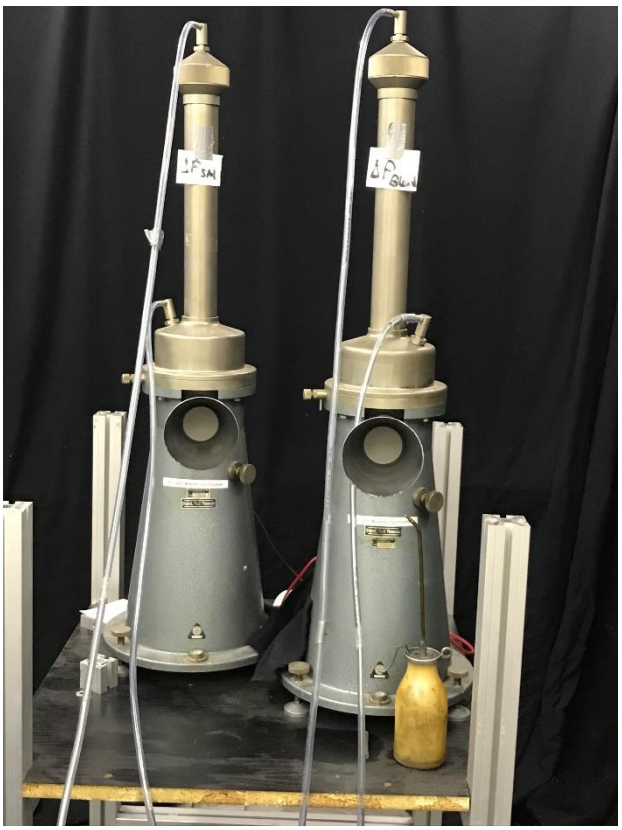

A 1: Betz Manometer

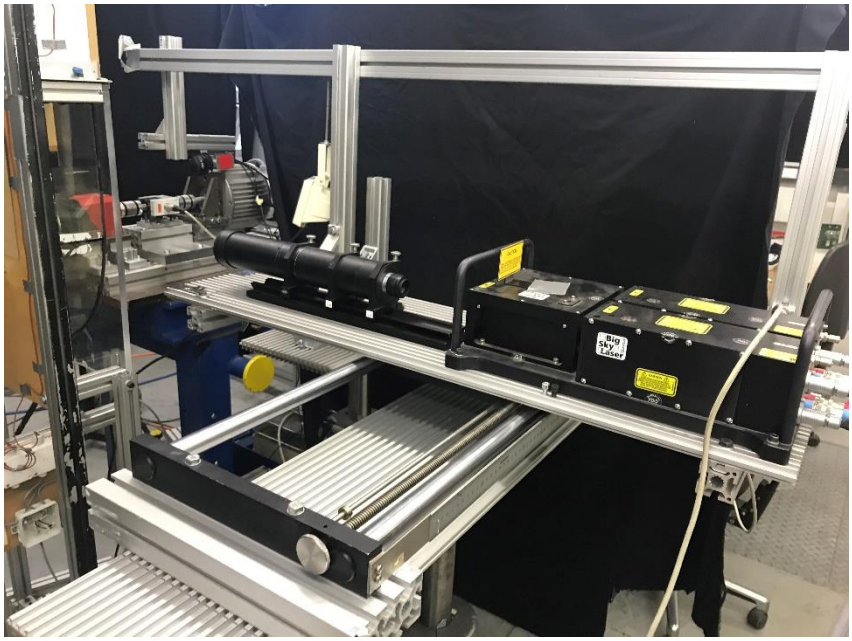

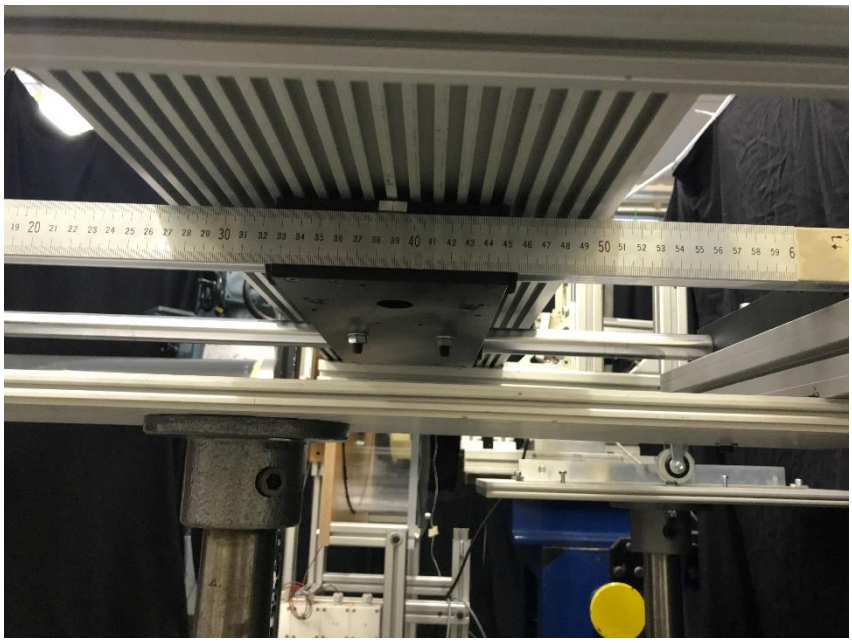

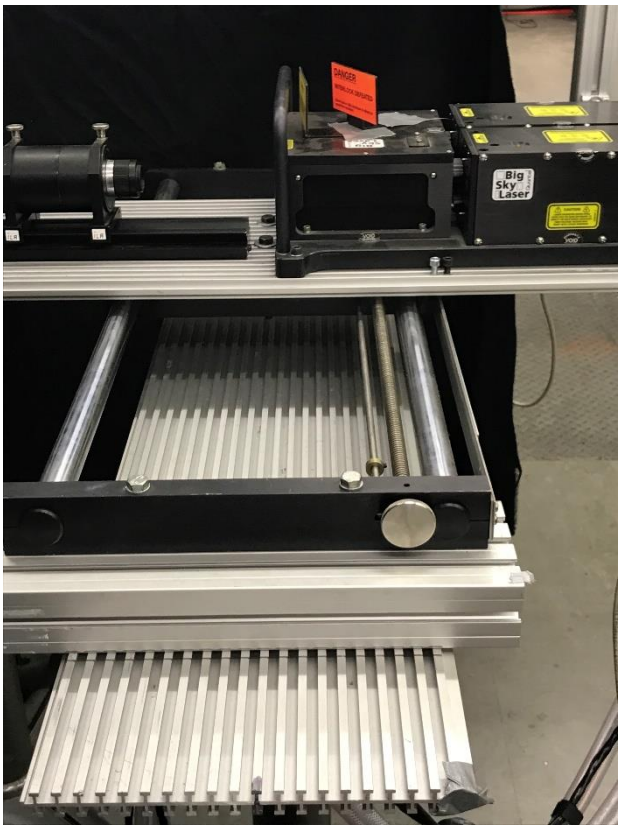

A 2: Mechanical linear actuator for PIV measurements 1 – 3

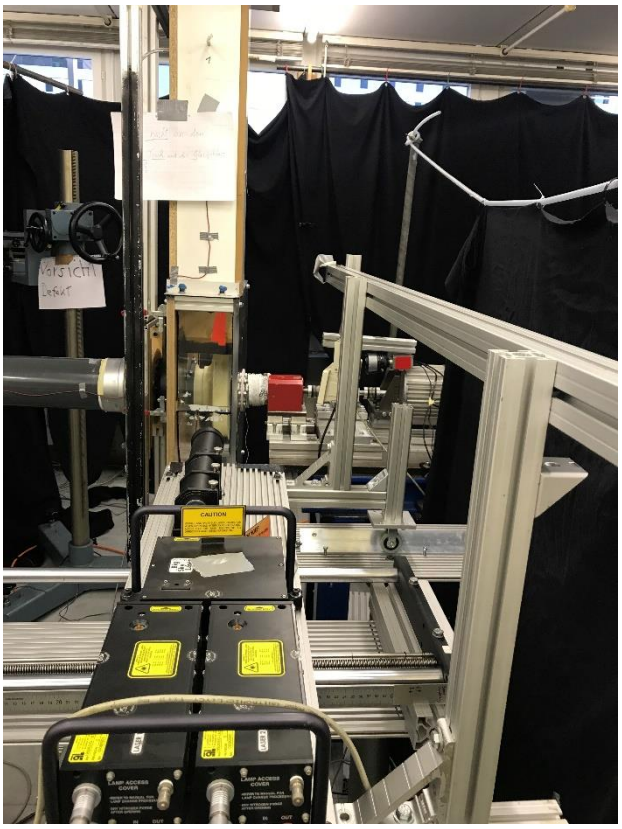

A 3: PIV set-up

A 4: Targets used for calibration

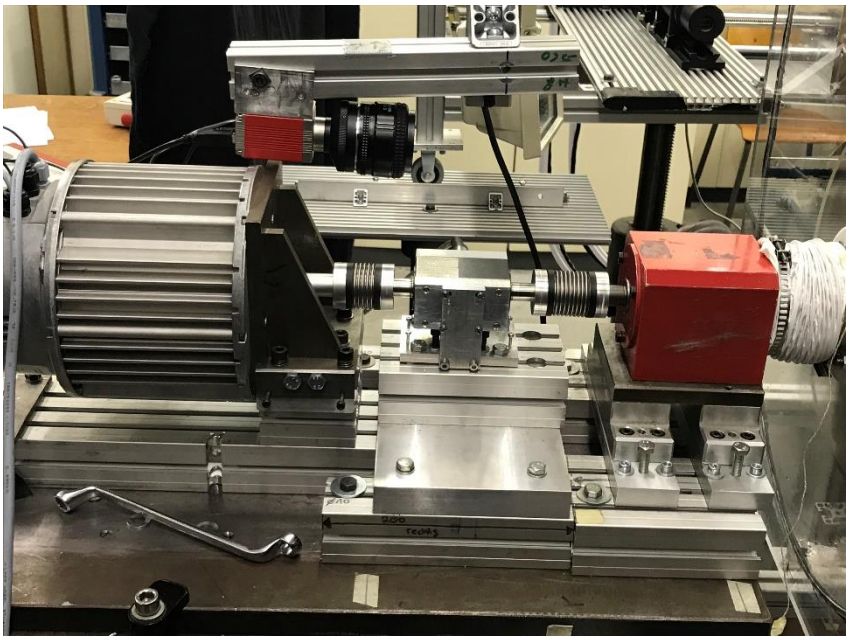

A 5: powertrain

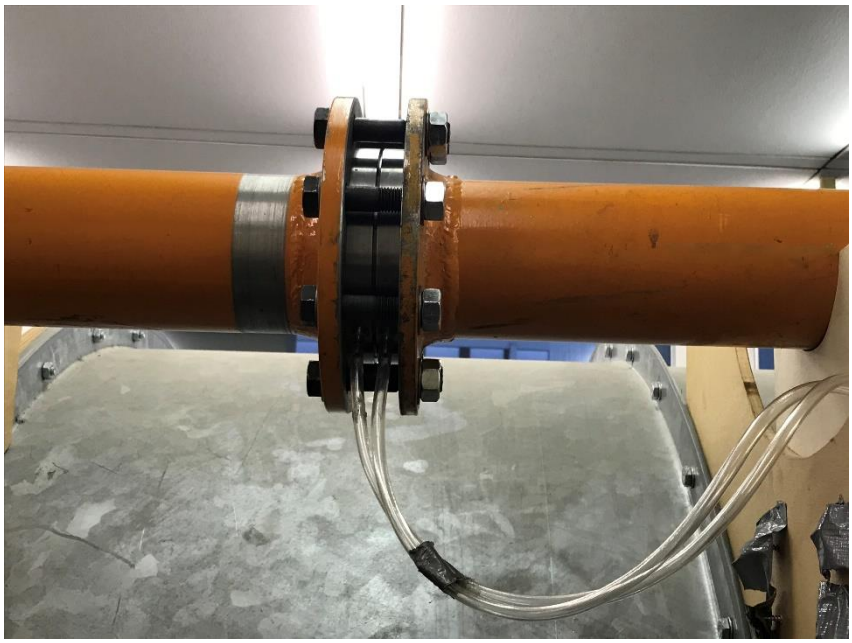

A 6: Flow rate measuring section with measuring orifice inside the duct and

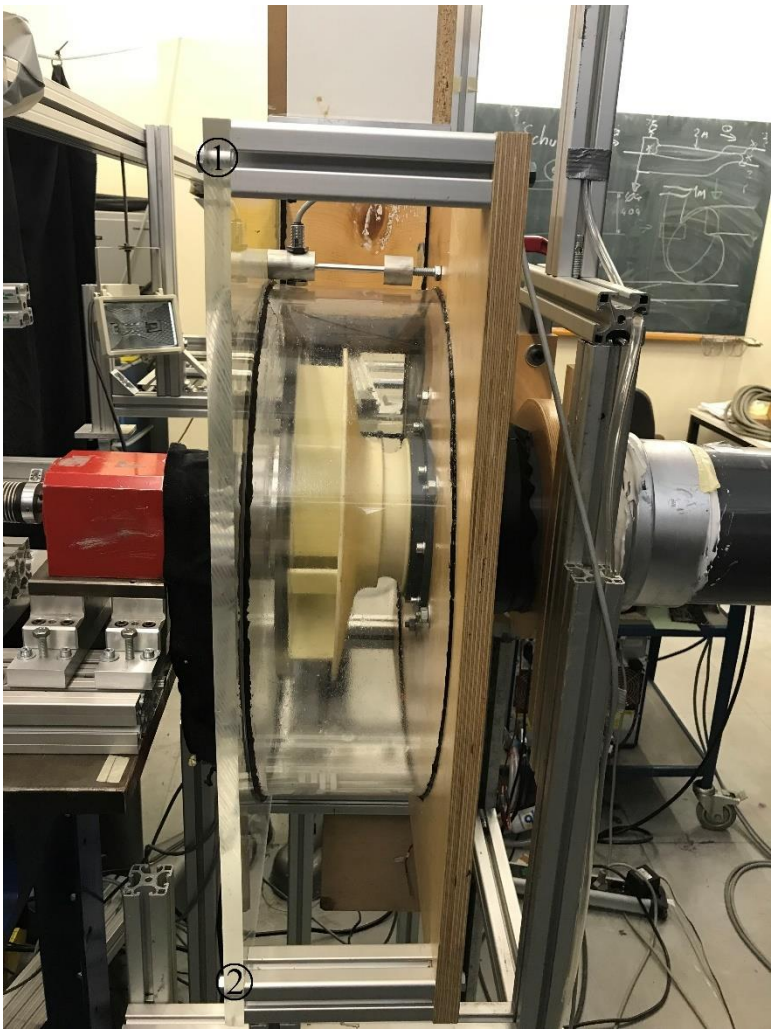

A 7: Connectors (1, 2) for housing

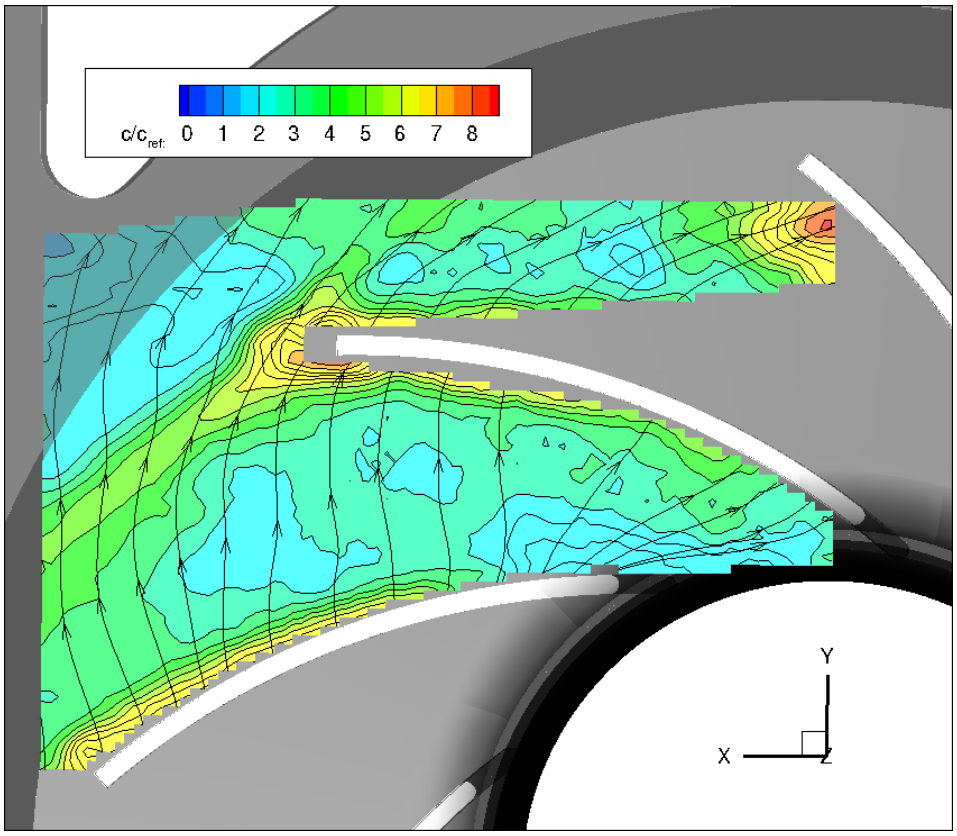

B 1: PIV measurement M2 at -12 mm; absolute velocity c

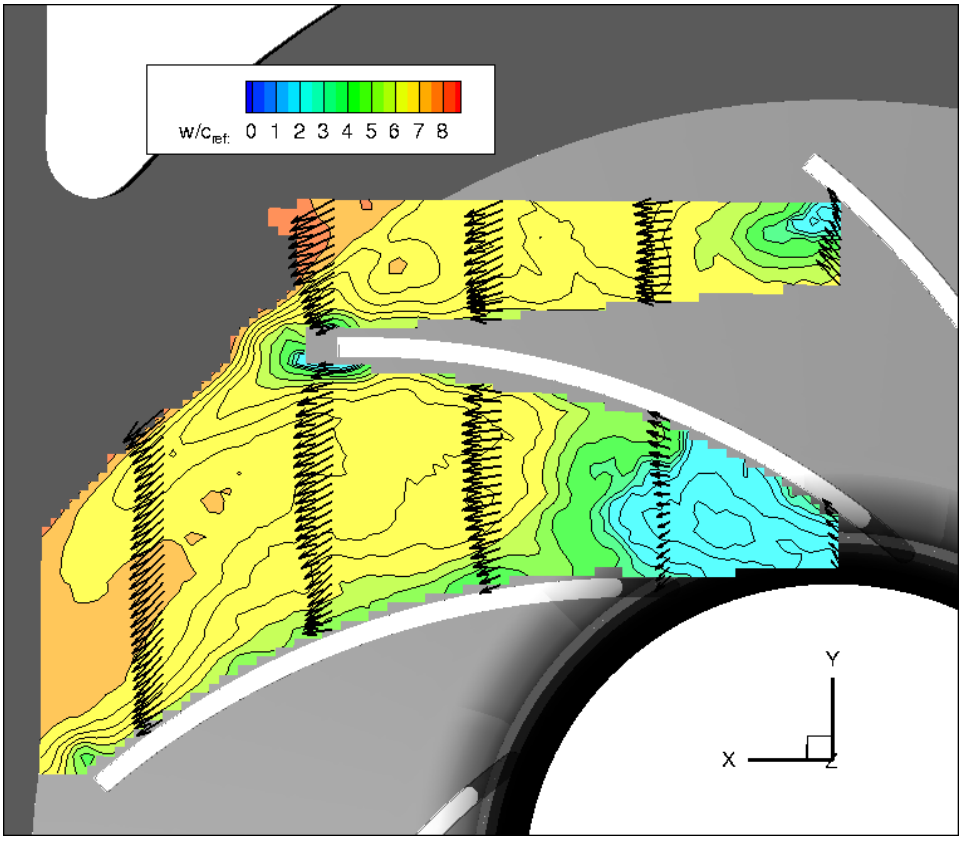

B 2: PIV measurement M2 at -12 mm; relative velocity w

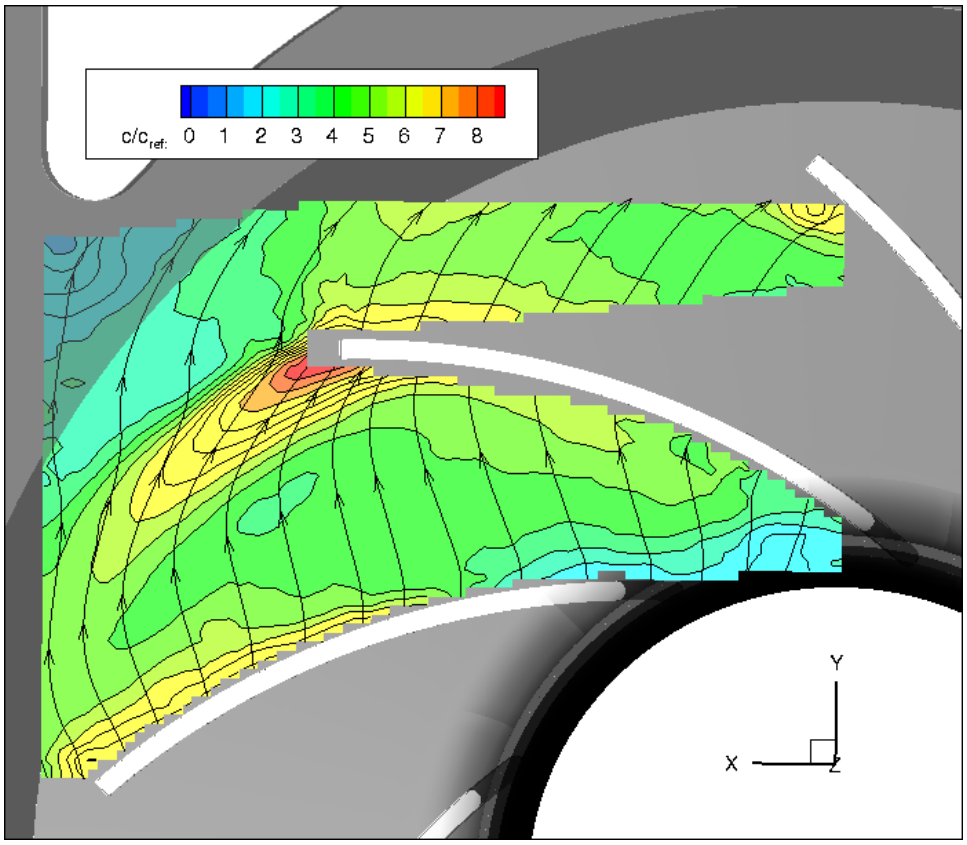

B 3: PIV measurement M2 at -18 mm; absolute velocity c

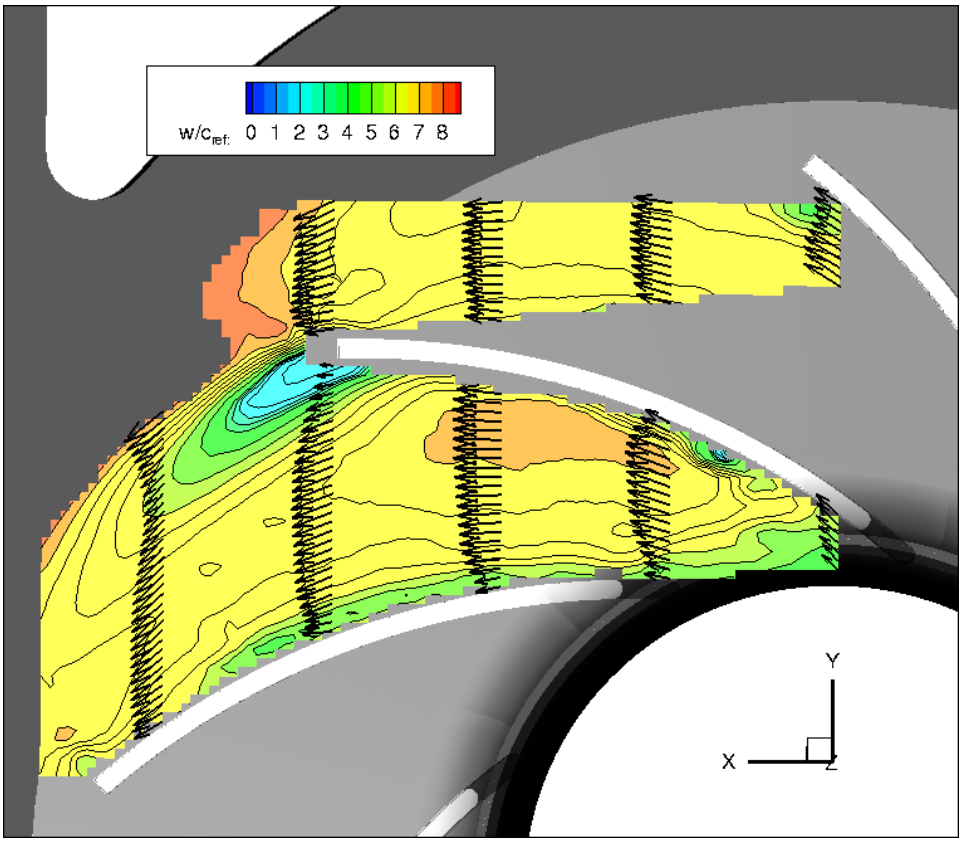

B 4: PIV measurement M2 at -18 mm; relative velocity w

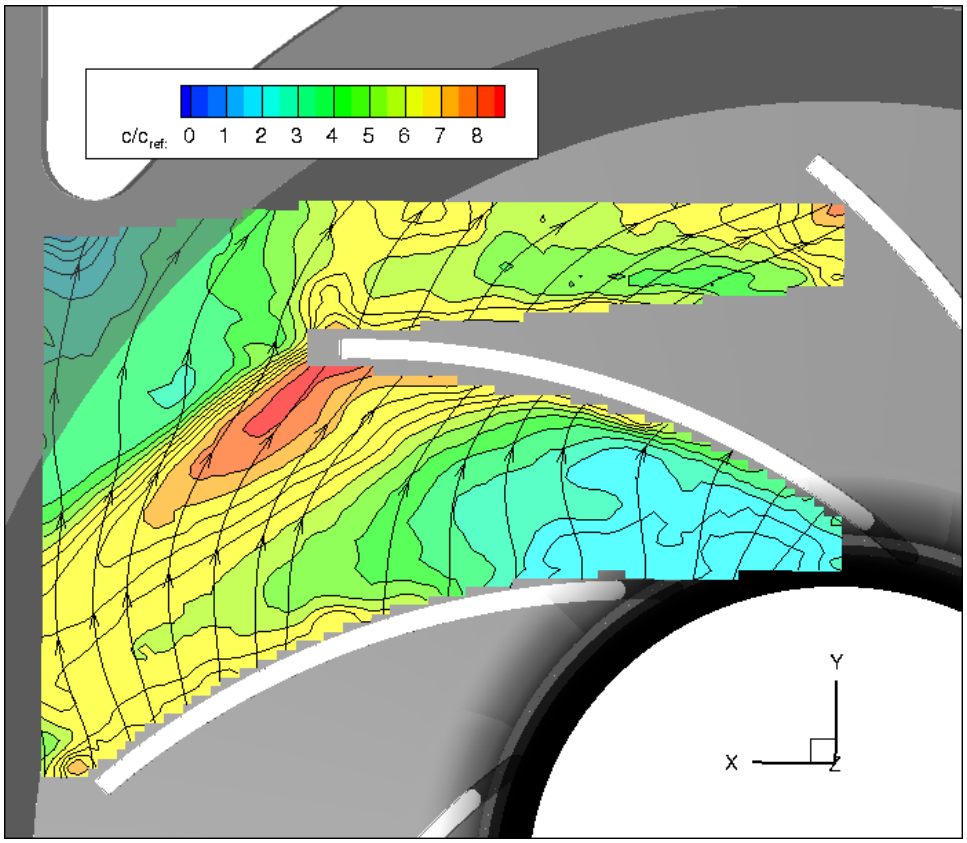

B 5: PIV measurement M2 at -30 mm; absolute velocity c

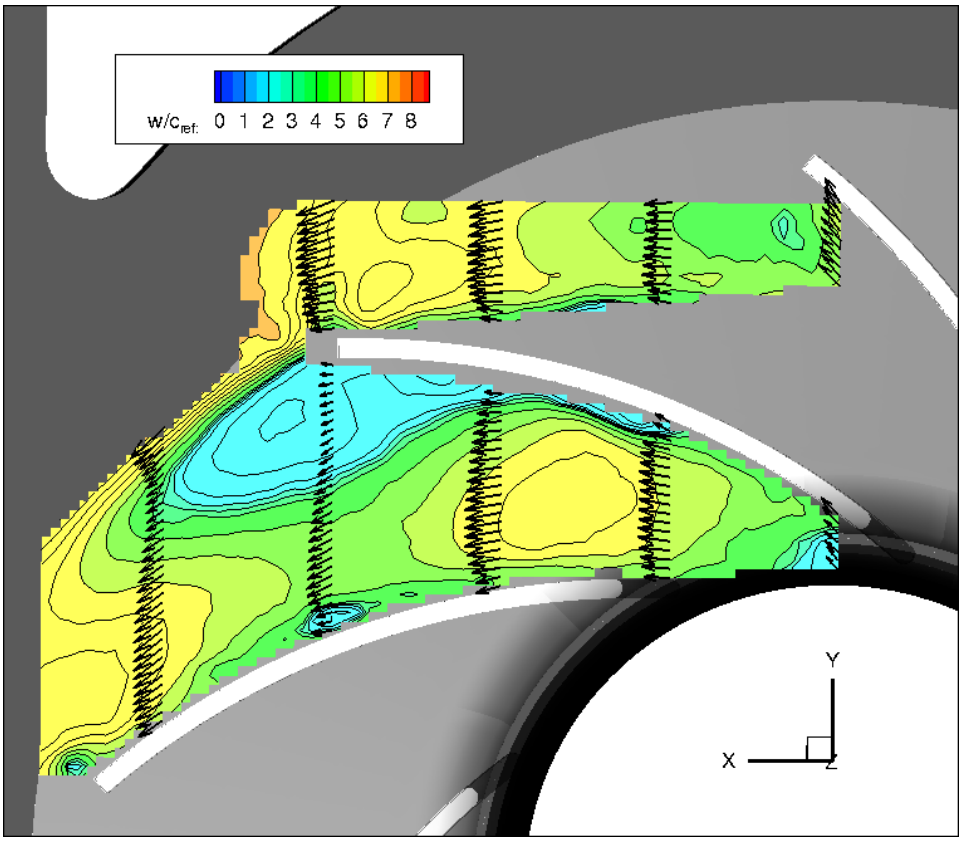

B 6: PIV measurement M2 at -30 mm; relative velocity w

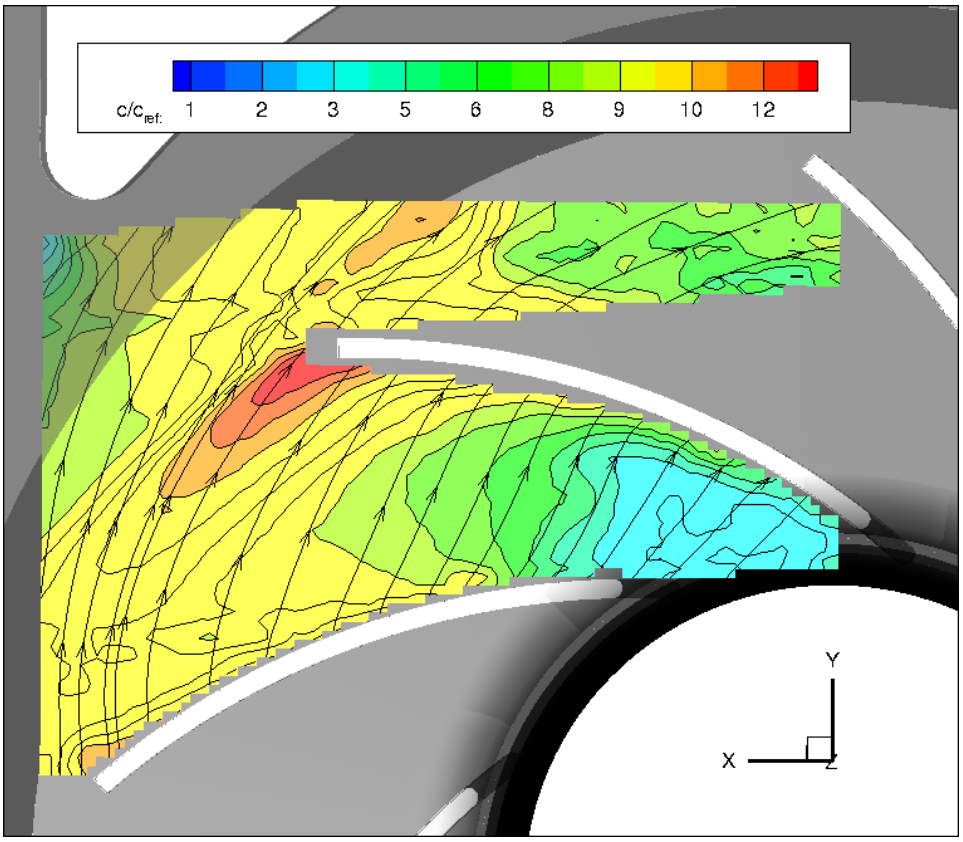

B 7: PIV measurement M3 at -12 mm; absolute velocity c

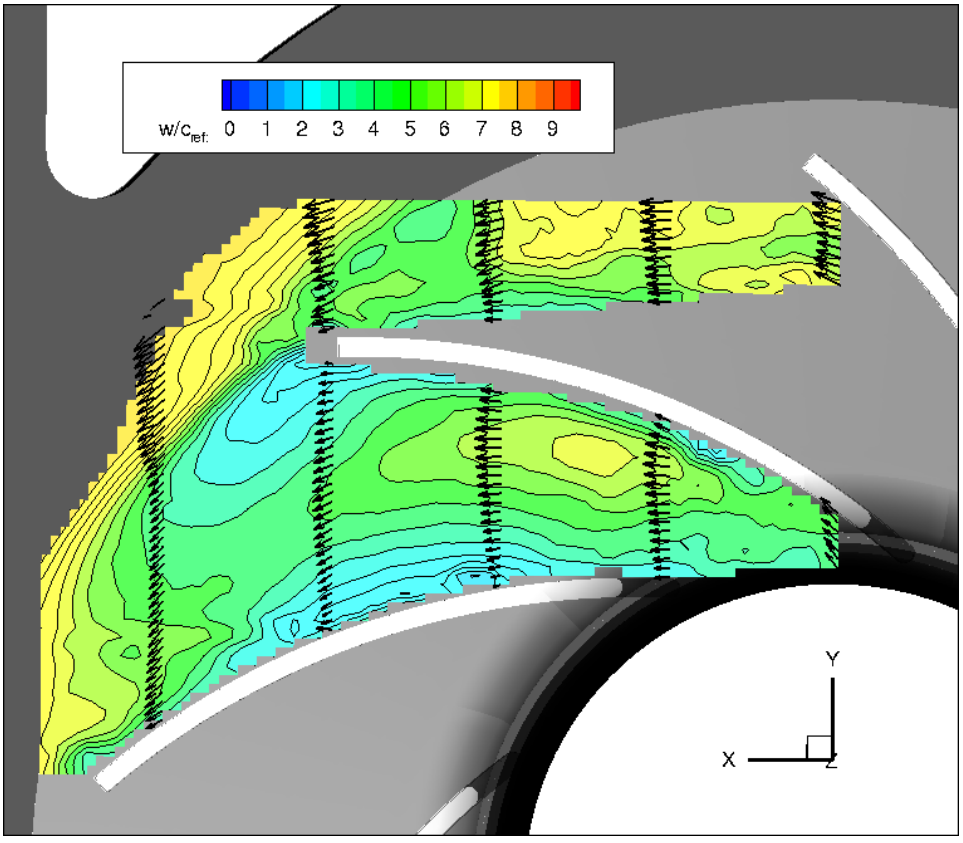

B 8: PIV measurement M3 at -12 mm; relative velocity w

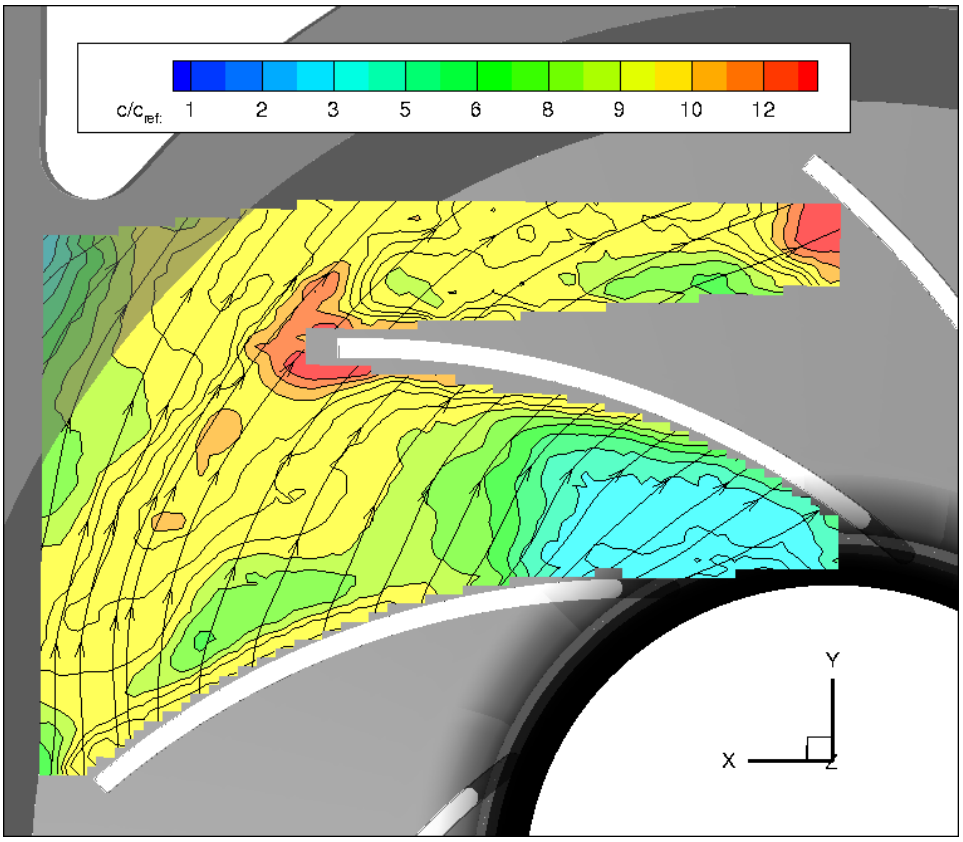

B 9: PIV measurement M3 at -18 mm; absolute velocity c

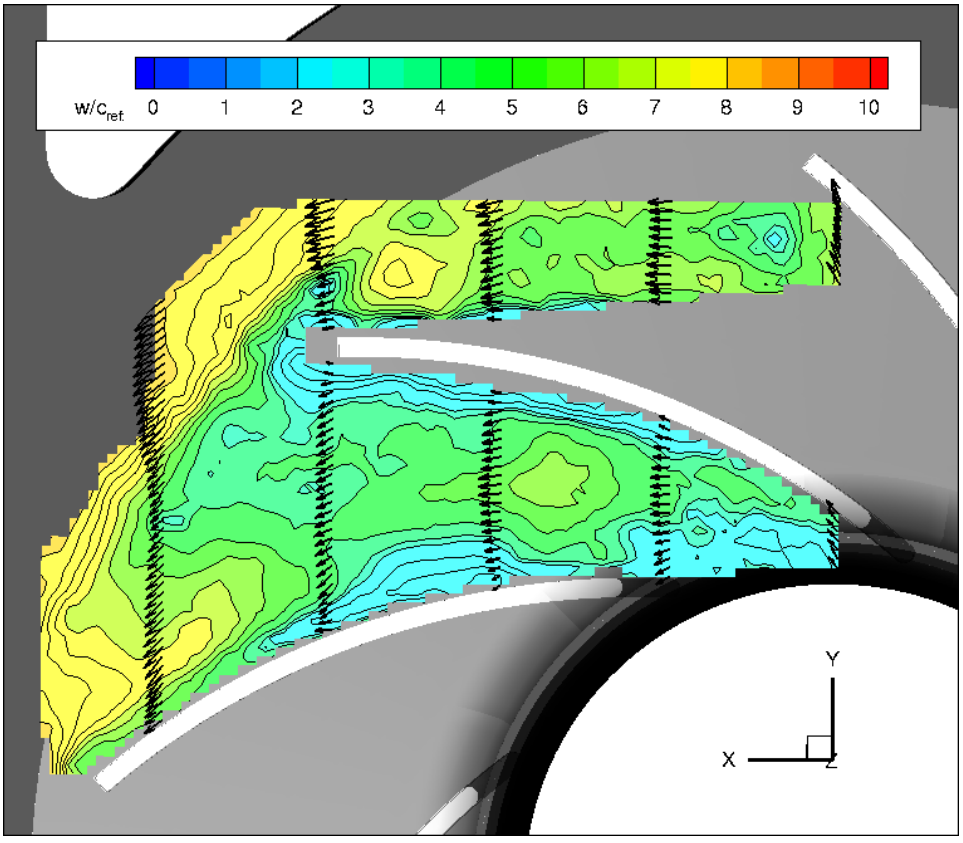

B 10: PIV measurement M3 at -18 mm; relative velocity w

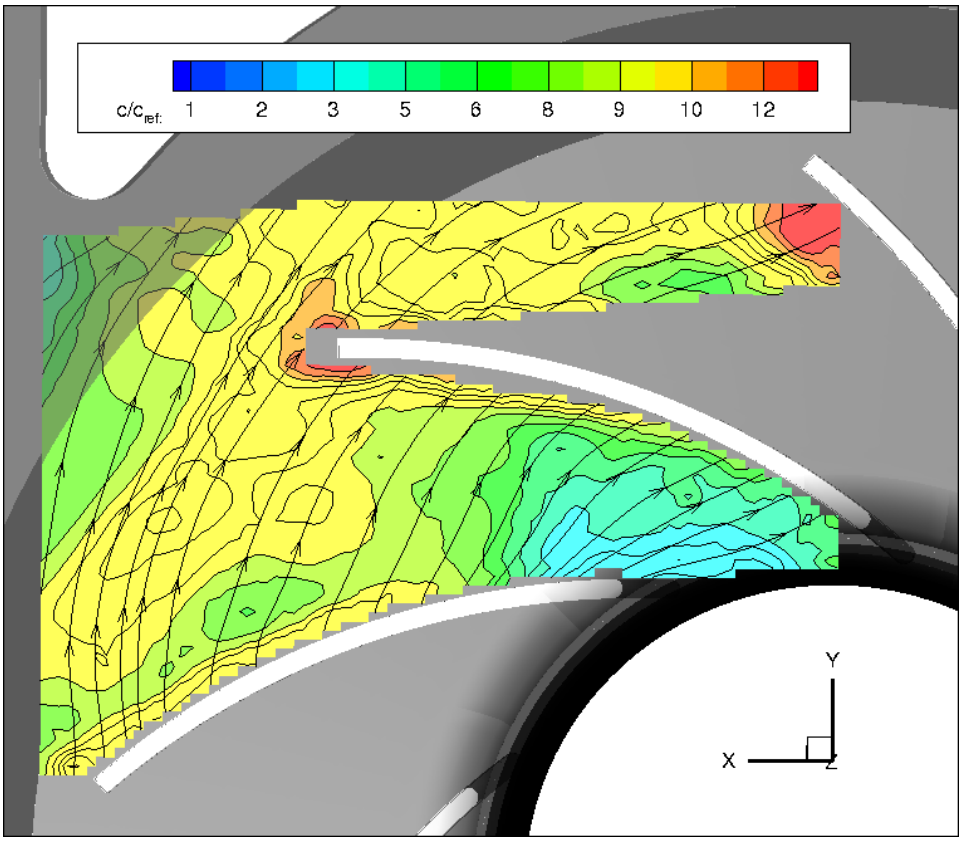

B 11: PIV measurement M3 at -30 mm; absolute velocity c

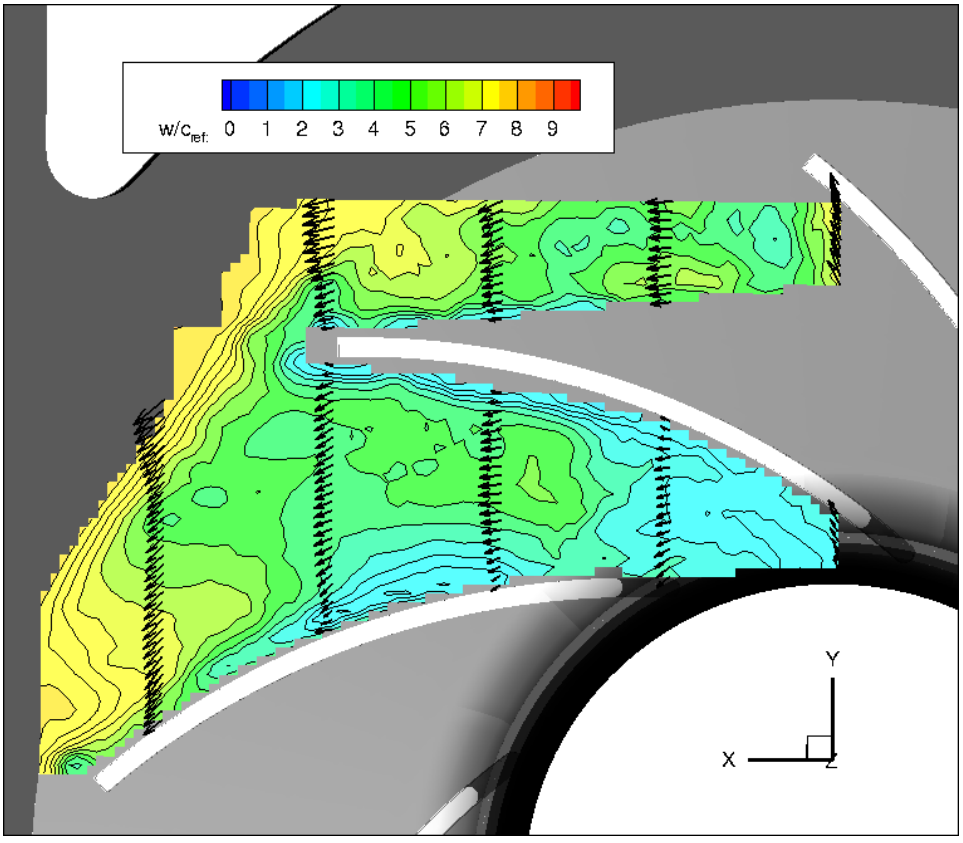

B 12: PIV measurement M3 at -30 mm; relative velocity w

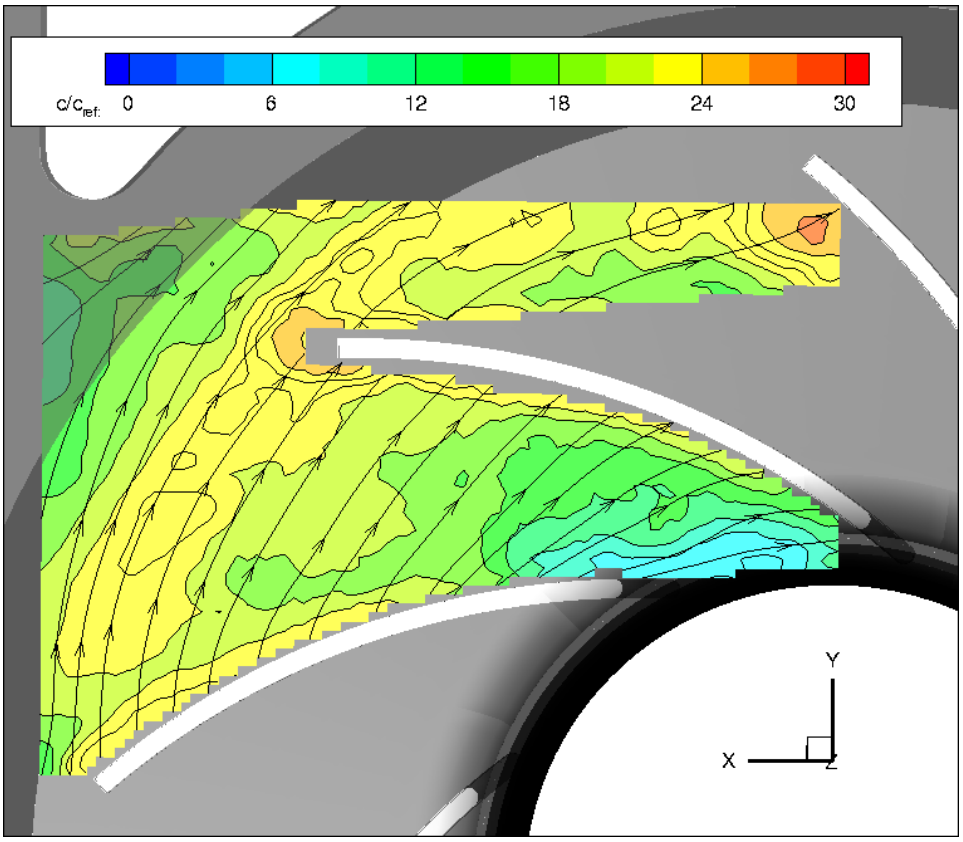

B 13: PIV measurement M4 at -12 mm; absolute velocity c

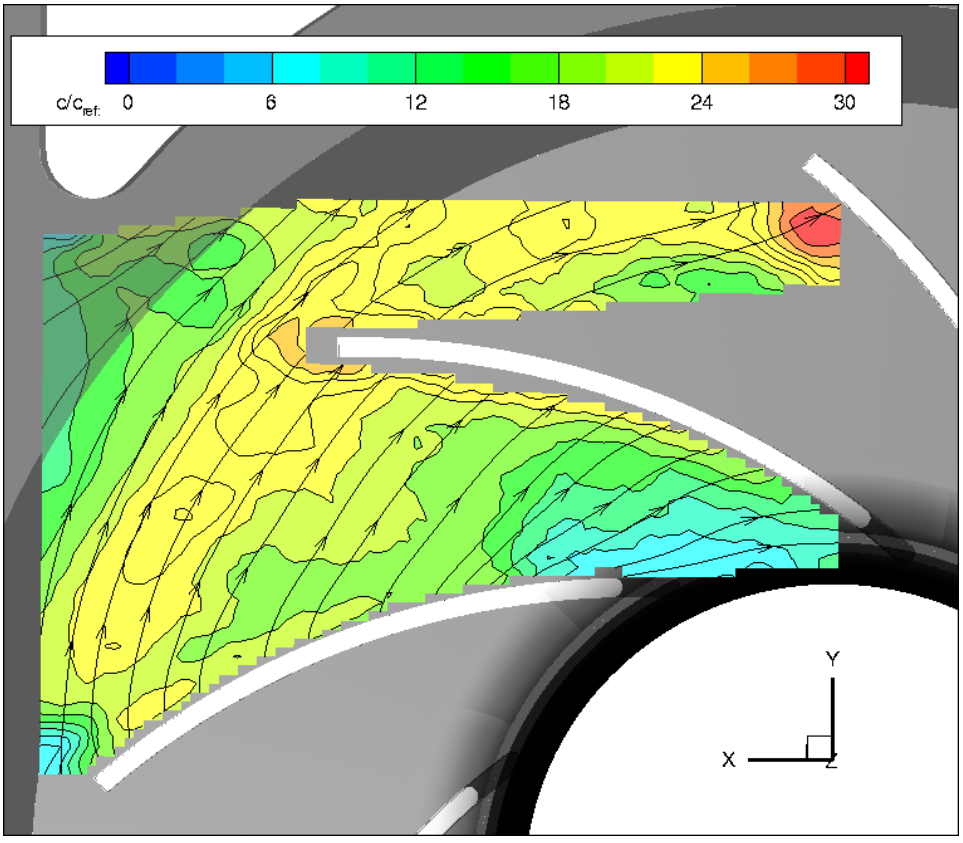

B 14: PIV measurement M4 at -12 mm; relative velocity w

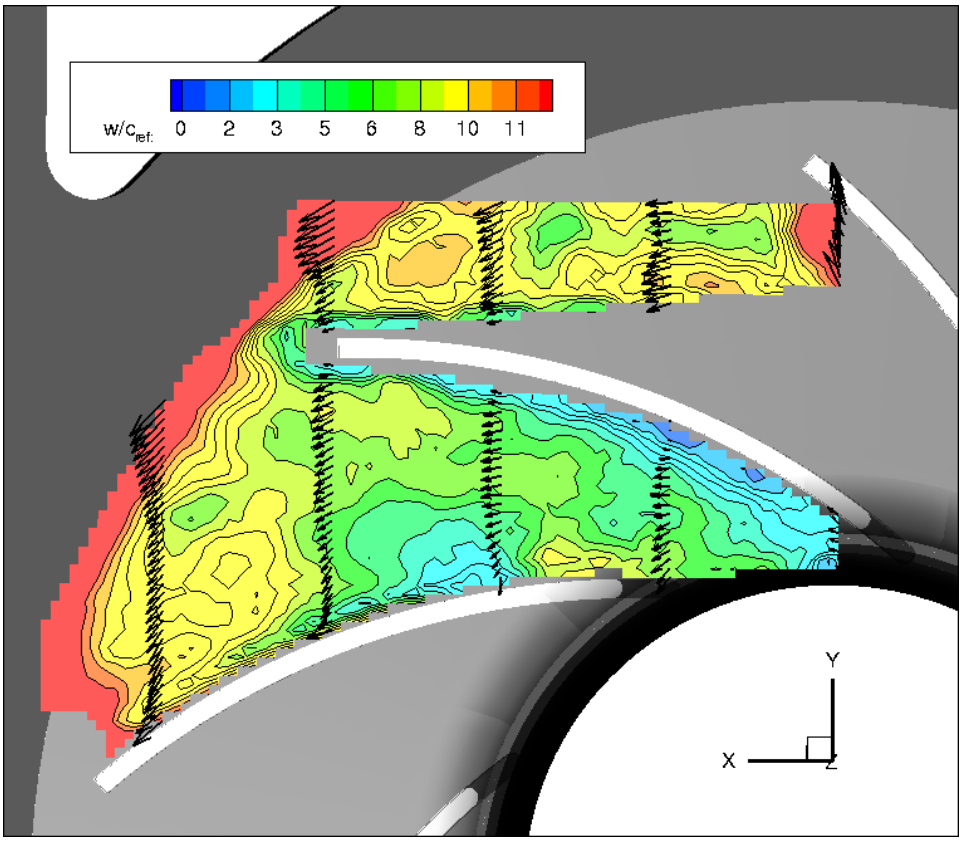

B 15: PIV measurement M4 at -18 mm; absolute velocity c

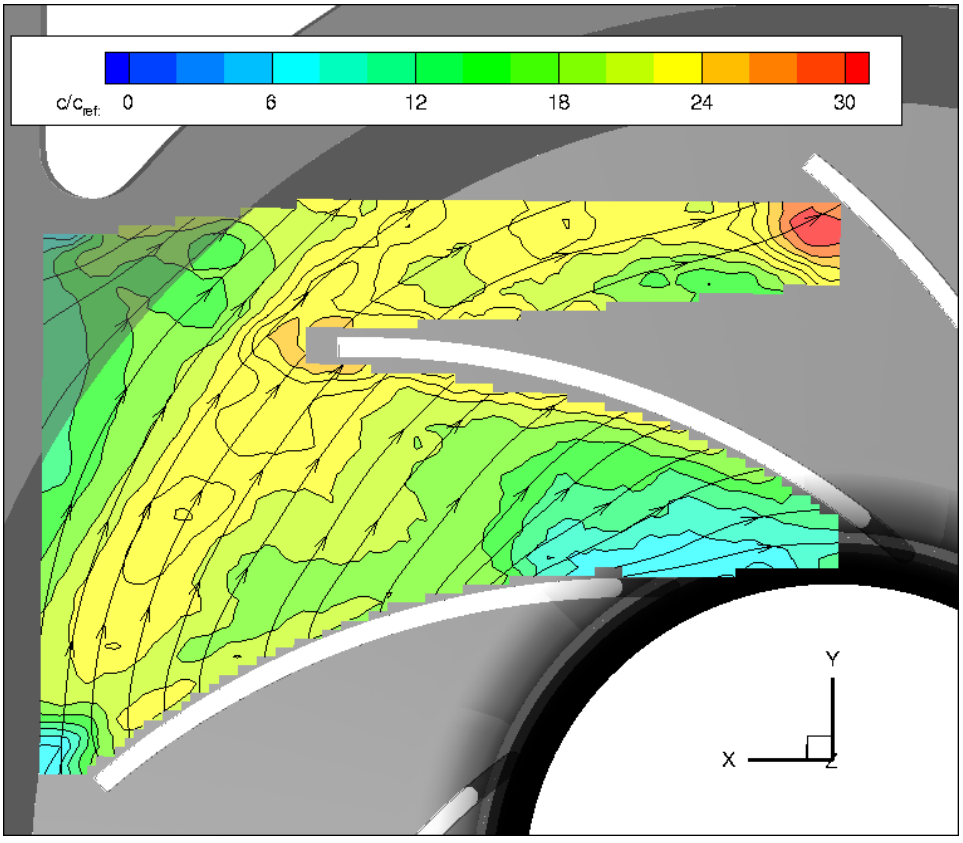

B 16: PIV measurement M4 at -18 mm; absolute velocity c

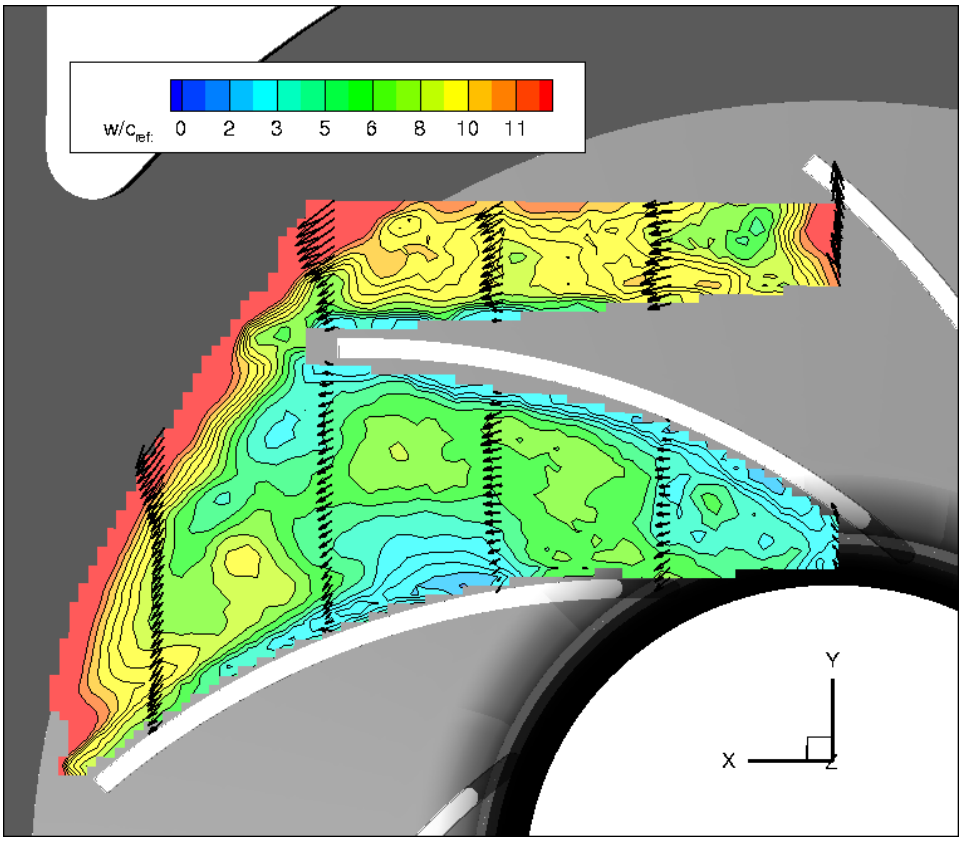

B 17: PIV measurement M4 at -30 mm; absolute velocity c

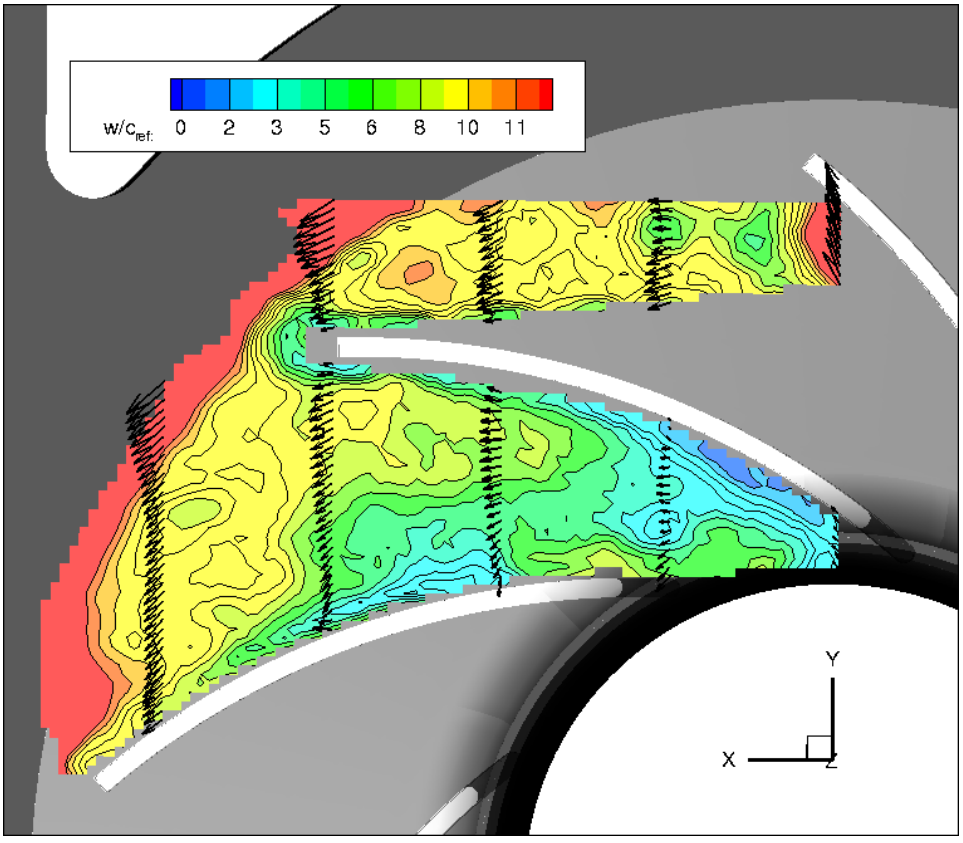

B 18: PIV measurement M4 at -30 mm; relative velocity w